An investigation of tropospheric refractive effects on Ka-band terrestrial links

Vowles, Mark Christopher

Award date:
2007

Awarding institution:
University of Bath

An investigation of tropospheric refractive effects on Ka-Band terrestrial links

Mark Christopher Vowles

A thesis submitted for the degree of Doctor of Philosophy

University of Bath
Department of Electronic & Electrical Engineering

July 2006

Accepted 2006

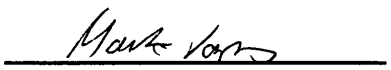

Mark Christopher Vowles

ProQuest LLC
789 East Eisenhower Parkway
P.O. Box 1346
Ann Arbor, MI 48106-1346

Contents

List of Figures

List of Tables

List of Symbols

Some symbols, single Arabic characters in particular, are used as constants or coefficients in addition to their meaning given below. Where this is the case, their alternative meaning is made clear in the text. Where a symbol has more than one meaning excluding use as a constant or coefficient, two entries appear below.

Mathematical meanings take precedence over the meanings given below.

a : Earth's radius, km

$B(\theta)$: Beam pattern, dependant on angle θ

c : Speed of light

c_1 : Slope in mixed layer

C_n^2 : Refractive index structure constant, $\mathrm{m}^{-2/3}$

d : Distance, m

δ : Evaporation Duct Height

e : Partial pressure of water vapour, mbar

e^t : Mathematical expression for $exp(t)$

e_s : Saturation water vapour pressure, hPa

E : Error function

ϵ : Dominant error term in series

ϵ_r : Dielectric Constant

f : Frequency

f_1 : First Fresnel size

F : Interferometer fringe function

$F[\,]$: Fourier transform of bracket contents

$F^{-1}[\,]$: Inverse Fourier transform of bracket contents

$F_\chi(\kappa)$: Fluctuation spectral density function for amplitude

$F_s(\kappa)$: Fluctuation spectral density function for phase

G_r : Gain of receive antenna

G_t : Gain of transmitter antenna

γ_R : Specific rain attenuation (dBm^{-1})

H : Relative humidity, %

h : Height, km

h_0 : Scale height, km

h_s : Surface height, km

k : Wavenumber

κ : Spatial wavenumber

L : Characteristic flow length, m

L : Path length, m

log : Logarithm, base 10

ln : Natural Logarithm

l_0 : Inner scale (dissipation range) of turbulence

L_0 : Outer scale (input range) of turbulence

λ : Wavelength

M : Modified refractivity

$M(z)$: Modified refactivity at height z

M_0 : M profile offset, intersection of mixed layer slope and $z = 0$

M_d : M deficit of the inversion layer

μ : Viscosity, $\mathrm{kgs^{-1}m^{-1}}$

N : Refractivity

N_0 : Average value of N, extrapolated to sea level

N_s : Refractivity at Earths surface

N_{wet} : Wet portion of refractivity, N

N_{dry} : Dry portion of refractivity, N

n : Refractive Index

$n(h)$: Refractive index at height h

P : Pressure, mbar

P_r : RF power at receiver

P_t : RF power at transmitter

$\Phi_n(\kappa)$: Refractive index spectral density - Kolmogorov Spectrum

ϕ : Phase angle, degrees

ψ : Electric field component

q : Board thickness

R : Rain rate ($\mathrm{mmh^{-1}}$)

R_e : Reynolds number

ρ : Fluid density, $\mathrm{kgm^{-1}}$

$S(k)$: Eddie stretch rate

σ_M : Standard deviation of total wind speed magnitude

T : Temperature, K

t : Temperature, °C

t : Time

t_h : Track thickness

τ : Polarisation tilt angle, degrees

τ_g : Geometric delay

θ : Angle, degrees

U : Flow speed, ms^{-1}

U_t : Total wind speed magnitude ms^{-1}

u : Reduced propagation function

w : Track width

ζ_m : Midpoint in finite step PE

Z_0 : Impedance, Ω

z_b : Trapping layer base height

z_{thick} : Thickness of inversion layer

Acronyms

A/D Analogue to Digital

AOA Angle of Arrival

APM Advanced Propagation Model

ASCII American Standard Code for Information Interchange

CS Chip Select

CW Continuous Wave - Sine wave transmission at a single frequency.

DC Direct Current

DPST Double Pole Single Throw

DTMF Dual Tone Multi-Frequency

DU Demodulation Unit - The unit comprising much of the receive hardware, specifically LO signal generation, IF processing, demodulation, amplification and power supply/regulation.

EEPROM Electrically Erasable Programmable Read Only Memory

EPROM Erasable Programmable Read Only Memory

FET Field Effect Transistor

FR Fire Retardant - Polymer/glass fibre cloth laminate used to make PCBs

GaAs Gallium Arsenide

GSM Global System for Mobile communication

I/Q In phase, Quadrature phase - The Sine and Cosine output signals resulting from demodulation.

IC Integrated Circuit

IF Intermediate Frequency - One resultant frequency of a mixer, down converted signal.

LED Light Emitting Diode

LO Local Oscillator - The locally generated frequency for mixing operations or the actual device responsible for the generation of this frequency.

LNA Low Noise Amplifier

MATLAB Matrix Laboratory

MM5 Mesoscale Model version 5

MMIC Monolithic Microwave Integrated Circuit

MOSFET Metal Oxide Semiconductor Field Effect Transistor

MUX Multiplexer

OfCom Office of Communications - Formerly the Radio Communications Agency RA

PC Personal Computer

PCB Printed Circuit Board

PDRO Phase Locked Dielectric Resonator Oscillator

PE Parabolic Equation

PIC

PLL Phase Locked Loop

RAM Random Access Memory

RCD Residual Current Device

RD Receive Data

RF Radio Frequency

RPO Radio Physical Optics

SIM Subscriber Information Module

SMA SubMiniature version A

SNR Signal to Noise Ratio

SPE Standard Parabolic Equation

TD Transmit Data

TPEM Terrain Parabolic Equation Model

USART Universal Synchronous-Asynchronous Receiver/Transmitter

VCO Voltage Controlled Oscillator

Acknowledgements

The author wishes to formally recognise and thank the following people for their assistance and contributions during the course of this period of study.

Mr Richard Lewton, Bristol Water, for his assistance in expediting the deployment of the transmitter on the Bristol Water Mast Reservoir site near Blagdon. In particular for the rapid installation of a mains supply but also for permitting the extension of the transmission period. Without the cooperation of both Mr Lewton and Bristol Water the experimental link would have been very difficult to establish, certainly on the 24/7 basis that we sought for this study.

Dr Duncan Hodges for his kind contribution in performing numerous model runs using the Mesoscale Model version 5 (MM5) and for converting the output into a Matlab friendly form. The time taken to assist in this way is both recognised and much appreciated, as is the contribution this data made to the analysis process. Thanks are also due for assistance rendered in other ways including Latex advice and the supply of 3 dimensional link maps.

Mr Mike Edwards, Mr Dave Hatten, Mr Trevor Ryan and Mr Mike Thomas for their assistance and advice in the course of preparing the equipment and its deployment. Particular thanks are due to Mr Mike Edwards for operating the equipment in remote locations during the testing phase.

Dr Robert Watson for constant advice, guidance and assistance throughout the PhD process.

Mark Vowles

Abstract

This thesis explores the theoretical background of high frequency radio propagation through the troposphere, setting out the range of problems facing communication links in the Ka-band. These include scattering and attenuation due to hydrometeors and the gasses present in the troposphere.

Millimetre frequencies are becoming of greater importance for communications links however, how they are affected by atmospheric scintillation remains largely undocumented.

An experimental Ka-Band terrestrial link covering some 28 km is described in detail, including the extensive work undertaken to refurbish, augment and successfully deploy the transmit and receive equipment.

Further consideration is given to the various techniques employed to model the propagation of radiowaves given various refractivity profiles. This and a refractive index profile model lead to the production of a refractive index profile database.

The thesis then brings together the theory and practical results from the experimental link to investigate the extent to which the refractivity present on the link affects the propagating beam. In particular its apparent angle of arrival at the receiver array.

This investigation covers a period of eight months from the link which operated for eleven months.

The conclusions reached from the investigation are that although there is some evidence of beam steering as a result of refractive bending, the magnitude of these angles is small. This is an interesting result as it contradicts observations reported in the literature. The result does indicate however that such links might operate well on closely spaced parallel link paths, a welcome result for many applications.

Chapter 1

Introduction

As demands on the radio spectrum increases and available bandwidth within established bands becomes scarce, interest naturally turns to higher frequencies. This introduces new challenges as frequencies affected by weather phenomenon become of interest. This work focuses on propagation at a frequency (36.57 GHz) which lies in an attenuation trough with respect to oxygen and water vapour. This fact makes this and similar frequencies prime candidates for high bandwidth links.

It is this type of narrow, point-to-point link which is considered in this work. The primary objective being to consider the mechanisms which lead to fading and wavefront distortion. One significant concern being that the beam might be steered off course which would have serious consequences for other similar links operating in close proximity.

The subjects of scintillation and bulk refractivity are key to this investigation as both potentially lead to fading and bending. Other mechanisms which affect the attenuation along the transmission path, in particular precipitation, are also due consideration.

An interferometer, inherited from an earlier study, was recommissioned and formed the basis of an experimental link. The aim being to continuously operate a microwave link of substantial length for a period. From the experimental data an assessment of the degree of beam bending was established for a range of weather and refractivity conditions experienced by the link during its operation.

To complement the experimental approach, a number of modelling techniques have been investigated with the intention of validating the experimental results and placing them in context.

Structure of Thesis

This thesis consists of seven further chapters.

In Chapter 2 the background theory pertaining to radio propagation is considered. An emphasis is placed on frequencies within the band of study and after a broad introduction, the characteristics which influence tropospheric microwave propagation are considered. The chapter also introduces the reader to interferometric techniques.

Chapter 3 reviews the available tropospheric propagation modelling techniques. These include the Parabolic Equation and Ray Optics. The various forms of PE are described, namely, the basic derivation, split-step and finite-difference.

Chapters 4 and 5 discuss the work carried out in relation to the design, construction, rebuilding, testing and preparation for deployment of the microwave equipment. Chapter 4 considers the transmitter while Chapter 5 considers the receiver array. Both chapters include discussion of the chosen solutions and the reasons behind the choices made, they also include design detail.

Chapter 6 introduces the Advanced Propagation Model (APM), breaking it down into its constituent parts. In doing so Chapter 6 develops a link between the experimental work and the theoretical approach first discussed in Chapter 3. Also introduced here is the database of APM model runs forming a propagation database. From this an assessment of the apparent AOA is derived. In achieving this it becomes possible to prepare a theoretical benchmark against which the experimental result can be compared.

Chapter 7 analyses the data collected by the experimental link. This chapter considers a number of identified periods during the data collection campaign for analysis. The analysis attempts to examine data from a broad base of conditions to build as complete a picture as is possible.

Chapter 8 concludes the work, summarising the results and proposing further work.

Chapter 2

Background Theory

2.1 Propagation at Millimetre Wave Lengths

2.2 Electromagnetic Spectrum

The portion of the electromagnetic spectrum used for practical radio systems extends from 3 kHz to 300 GHz and is divided into broad bands and named as shown in Table 2.1. Further band definitions exist for frequencies in the Gigahertz range including C-band (4-6 GHz), Ku-band (12-14 GHz), Ka-band (20-30 GHz) and V-band (40-50 GHz).

In recent times, interest has shifted toward higher frequencies. These frequencies boast higher bandwidths, ideal for high speed bulk data transfer applications. Significant advantages are to be gained from the smaller size of antenna necessary for equipment operating at higher frequencies, however, there are difficulties associated with the propagation of these signals. These difficulties will be reviewed in this chapter with a particular emphasis on terrestrial millimetre wave propagation in the troposphere.

2.3 Atmospheric Effects

Radio waves propagating through the atmosphere are attenuated and scattered by various mechanisms. The predominant mechanism for a given link depends on a number of factors including frequency and elevation angle. Tra-

Table 2.1: Electromagnetic Spectrum

Band Name	Frequency Range	Wavelength
VLF	3 kHz - 30 kHz	100 km - 10 km
LF	30 kHz - 300 kHz	10 km - 1 km
MF	300 kHz - 3 MHz	1 km - 100 m
HF	3 MHz - 30 MHz	100 m - 10 m
VHF	30 MHz - 300 MHz	10 m - 1 m
UHF	300 MHz - 3 GHz	1 m - 10 cm
SHF	3 GHz - 30 GHz	10 cm - 1 cm
EHF	30 GHz - 300 GHz	1 cm - 1 mm

ditionally satellite links have operated at higher frequencies than terrestrial links. This has been possible because of the relatively short path through the Earth's atmosphere, in particular the troposphere. As the elevation angle of the link decreases, an increasing proportion of the link passes through the troposphere and thus its effects on the link become more significant.

The troposphere contains a number of gases which attenuate, scatter and depolarise radio waves leading to a highly variable, weather dependent, level of attenuation. Oxygen, water vapour and other minor constituents interact with the electric field, the vastly larger proportions of oxygen and water vapour making their effects more significant. Oxygen has a permanent magnetic dipole moment and water vapour has an electric dipole. Work in the theory of attenuation by atmospheric gasses has been given in the literature [1]. The interaction between a radio wave propagating through the troposphere and these molecules gives rise to attenuation peaks at 60 and 119 GHz for Oxygen and 22, 183 and 325 GHz for water vapour. At and near these frequencies, the attenuation of radio waves is orders of magnitude greater than other frequencies within the same band. Between these attenuation peaks there are a number of windows of relatively low attenuation. One such window is centred on 35 GHz, chosen for study in this thesis. Clearly the water vapour content of the troposphere varies both temporally and spatially while the contribution of oxygen varies only with height due to pressure.

Figure 2.1 shows the specific attenuation in dBkm^{-1} for oxygen (dry

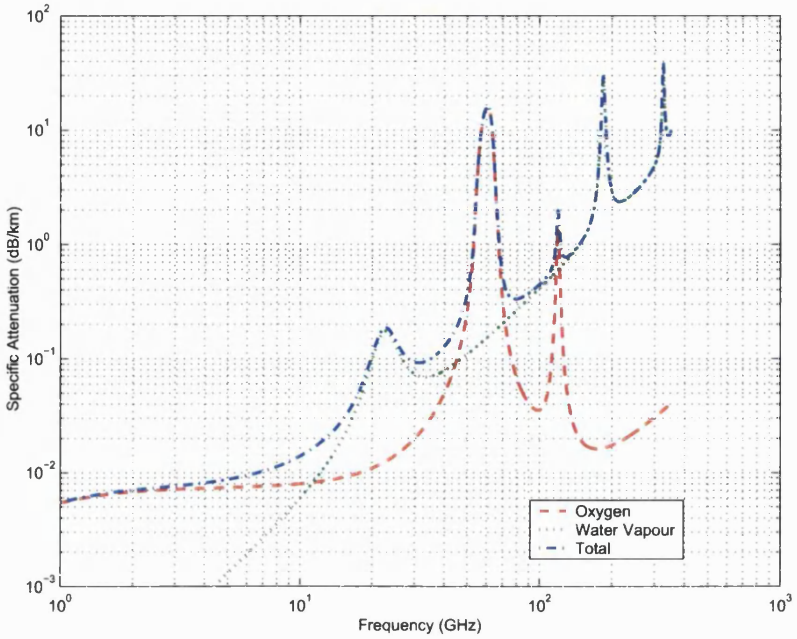

Figure 2.1: Specific attenuation due to gaseous absorption in the atmosphere

$$\begin{aligned} \text{Pressure} &= 1013\,\text{hPa} \\ \text{Temperature} &= 15\,^{\circ}\text{C} \\ \text{Water Vapour} &= 7.5\,\text{gm}^{-3} \end{aligned}$$

air), water vapour and the combined attenuation. The plot is based on the simplified ITU-R model [2]. The peak in attenuation for oxygen between 50 and 70 GHz is the result of individual resonances which can be calculated using the more accurate line-by-line model calculation [2]. For illustrative purposes though, the simplified algorithms are adequate.

The surface water vapour density exceeded for various percentages of the year are given in an ITU-R model [3] which shows that for the link in this study, the average water vapour density is $7.87\,\text{gm}^{-3}$ reaching a maximum of $13.76\,\text{gm}^{-3}$ for 1 % of the year.

2.4 Precipitation

Radio waves above 3 GHz are also affected significantly by precipitation. The term commonly used to describe precipitation in this context is 'hydrometeor'. This describes a diverse range of precipitation including mist, rain, freezing rain, ice pellets, snow, hail/graupel, ocean spray, clouds and fog. The size of the particles in all of these cases generally exceeds 1 μm. The effect of these hydrometeors varies not only on the frequency of the radio waves but also the size, shape, descent angle and density of the particles themselves.

Each type of hydrometeor will now be examined and discussed in relation to the operating frequency of the link in this study.

2.4.1 Rain

Rain is the most significant form of hydrometeor for millimetre wave propagation. At millimetre wave frequencies the size of the droplets is comparable to the wavelength of the signal, this causes scattering rather than absorption to be the predominant method of signal attenuation.

The effect of rain on the propagating signal also depends on the shape of the droplets. Small drops can be assumed to be spherical however as drop size increases the shape approximates vertically symmetric oblate spheroids. A number of studies have examined drop shape & size through techniques including photography, examples are [4], [5], [6] and [7]. In the case of [7] very good agreement between theory and practical experiments were obtained. The oblate spheroid drop shape leads to a difference in the attenuation experienced by vertically and horizontally polarised waves. This possibility was examined by the research group at Bell Laboratories [8], [9] & [10] and others [11], since this has significance on microwave links using dual polarisation on channels as a means to increase link capacity. Circularly polarised waves (such as those used in this link) are affected according to how the wave is incident on each drop; in modelling it is assumed that the wave is equally likely to be horizontally or vertically polarised at the point of interaction. As the drop size exceeds 4 mm (radius) the droplets become oblate spheroids

with a concave base. Beyond 9 mm the droplets are unstable and break up forming smaller drops and are modelled accordingly.

The effect of rain is also dependent on the rain rate, the more droplets there are between the transmitter and receiver, the more scattering will occur. This rate cannot be assumed to be constant spatially; one portion of the link may be affected by one rain rate while another is affected by a different rate for example. The concept of an effective path length is therefore often used to model the non-uniform nature of rain fall.

Additional complicating factors are drop-size distribution and canting angle. Drop-size distribution investigations began using the 'absorbent paper' method, involving filter paper dusted with dye which is then exposed to the rain. This method was subsequently used widely by investigators though more recent studies, [12] have made use of electronic instruments such as disdrometers which convert the momentum of drops falling on a diaphragm into electronic signals [13]. One more recent development is the 2D-Video-Disdrometer, [14], which employs two video cameras positioned at 90 degrees to each other. The rain drops passing through the virtual analysis window created by the intersection of the two camera views are considered for measurement while splashes and drops passing through the view of just one camera are rejected.

Two important drop size distributions commonly used are the Marshall-Palmer [15] and Laws-Parsons [16] distributions. The earlier Laws-Parsons distribution is tabulated empirically rather than mathematically expressed and shows fewer small drops but is otherwise similar. More recent work has shown significant variations both between rain events and even within a single event which has resulted in a more general distribution, the gamma-type distribution of [17]. Even so no definitive distribution has yet been reached. Fortunately for the purposes of modelling it is not necessary to have a distribution which exactly describes the physical drop size. On average, the Marshall-Palmer distribution is considered satisfactory for frequencies in the 10-30 GHz range and slightly higher.

The effect of the canting angle was first considered in [9] and significant work in this area may be found in review papers, [18] & [19].

In order to determine the attenuation due to rain, the specific attenuation, γ_R (dBkm^{-1}), and rainfall rates, R in mmh^{-1} are used in Equation 2.1 [20]. The formula uses frequency dependent coefficients k and α which are available for horizontal and vertical polarisations at specific frequencies from tables or can be calculated for intermediate frequencies. Equations 2.2 and 2.3 use tabulated constants for horizontal and vertical polarisations to generate the coefficients k and α. Equations 2.4 and 2.5 allow k and α to be calculated for circular polarisation or fixed polarisation tilted relative to horizontal and any elevation angle.

$$\gamma_R = kR^{\alpha} \tag{2.1}$$

$$\log k = \sum_{j=1}^{3} \left(a_j \exp\left[-\left(\frac{\log f - b_j}{c_j} \right)^2 \right] \right) + m_k \log f + c_k \tag{2.2}$$

$$\alpha = \sum_{i=1}^{4} \left(a_i \exp\left[-\left(\frac{\log f - b_i}{c_i} \right)^2 \right] \right) + m_\alpha \log f + c_\alpha \tag{2.3}$$

Where:

- γ_R: Rain induced attenuation (dB km^{-1})
- R: Rain rate (mm h^{-1})
- f: frequency (GHz)
- k: either k_H or k_V
- α: either α_H (horizontal) or α_V (vertical) depending on constants selected.
- $a_{i,j}, b_{i,j}, c_{i,j}, m_{k,\alpha}, c_{k,\alpha}$ are dependent coefficients.

$$k = [k_H + k_V + (k_H - k_V)\cos^2\theta \cos 2\tau]/2 \tag{2.4}$$

$$\alpha = [k_H\alpha_H + k_V\alpha_V + (k_H\alpha_H - k_V\alpha_V)\cos^2\theta \cos 2\tau]/2k \tag{2.5}$$

Where:

- θ: is the path elevation angle
- τ is the polarisation tilt angle relative to the horizontal, for circular polarisation, τ=45°

In order to calculate the anticipated attenuation on a given link caused by rain, the rainfall rate is required. This is obtained from data collected over a long period of time; in the case of the rain rates from ITU-R [21], 15 years. The data are supplied across the whole globe at 1.5° intervals in both longitude and latitude. Bi-linear interpolation is necessary to obtain a rain rate for a specific location. In link planning and for other calculations it is necessary to determine the rain attenuation experienced for a given percentage of an average year.

Using the ITU-R data, the rain rate exceeded for 0.01% of the average year for the receiver location is 27.9955 mmh^{-1}. The specific rain attenuation can then be obtained from a graph of attenuation against frequency generated using Equations 2.1 - 2.5. Figure 2.2 gives 5.98 dBkm^{-1} at the link frequency for 0° elevation and circular polarisation. For a link of 20 km, the total attenuation would be 64 dB [22], much more than is commercially included in link budgets where a figure of 25 dB is typical. This clearly demonstrates how significant an effect rain has on signals at these frequencies.

2.4.2 Clouds and Fog

The droplets found in non-precipitating clouds and fog are too small to produce appreciable scattering for frequencies below 100 GHz [23]. The droplets themselves are well modelled as spheres meaning that cross polarisation effects, in theory at least, are not experienced though in practice some degree of cross polarisation is detectable. The only difference between cloud and fog is the height at which they occur. For terrestrial links, fog will be a more common occurrence than cloud.

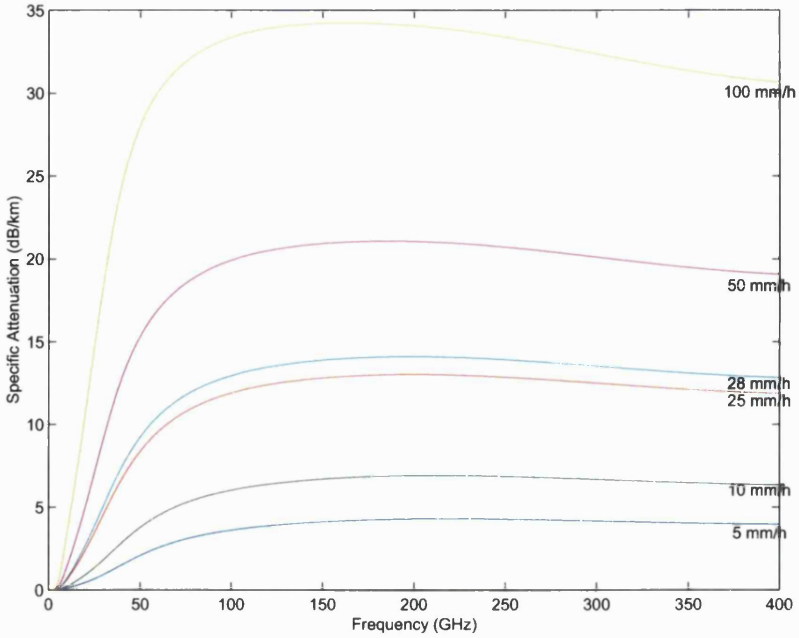

Figure 2.2: Rain attenuation for frequencies between 1 and 400 GHz at discrete rain rates

2.4.3 Ice

Ice hydrometeors come in a number of forms which can, for the purposes of radio wave propagation, be classified into a number of simple types.

2.4.3.1 Ice Crystals

Ice crystals forming at higher altitudes appear to be the most significant form of ice hydrometeors in respect to radio propagation. Broadly speaking there are two crystal classes. The first class includes hexagonal discs of ice with diameters around 0.5 mm and a thickness of approximately one tenth the diameter and crystals of the classical dendritic form, reaching 5 mm in length and thickness 0.05 mm. The second class includes needle shapes and hexagonal prisms, typical lengths 0.5 mm and a length to width ratio of 1-5 [23].

In terms of modelling the effect of ice crystals on radio scatter, when the

size of the ice crystal is smaller than the wavelength, can be modelled as oblate or prolate spheroids [24], [25] & [26]. Although scattering due to ice can be significant, losses due to absorption are small.

The formation of these types of crystal is highly dependent on temperature and thus the height at which they form. Plates tend to form between $-8°C$ and $-27°C$ with dendrites dominating between $-14°C$ and $-17°C$. Prisms form below $-27°C$ while the range $0°C$ to $-8°C$ sees the formation of either class.

2.4.3.2 Snow

Snow is simply a group of ice crystals which form the flakes at lower altitudes at temperatures just below freezing. At this temperature the snow surface is particularly sticky leading to the aggregation of the ice crystals. Dry snow flakes have little effect on radio propagation below 30 GHz due to their low water density (typically $0.1\,\mathrm{gm}^{-3}$) and the polarisation effects are mitigated by the fact that the flakes tumble in a random manner as they fall. A number of studies have examined how snow flakes fall, [27] & [28], the latter concluding that they oscillate with angles between 5° and 10° as they fall.

2.4.3.3 Sleet

Sleet forms when snow flakes melt. The effects of sleet on propagation can be considerable because the water content is higher as the flakes merge but fail to fragment as rain drops of a similar size would. In addition to issues of drop size and fall rate, the melting process depends on temperature which in turn is a function of height and thus link geometry plays a role in determining the effects of sleet [29].

2.4.3.4 Hail & Graupel

Hail and graupel form from supercooled cloud droplets. Hail forms roughly spherical shapes and has a similar density to rain. Graupel has a density between hail and snow and forms conical shapes. The effect of dry hail and graupel is not significant below 30 GHz however as they melt they attenuate

as very large rain drops with significant polarisation and attenuation effects. Studies of melting hailstones [30] & [31] at centimetre wavelengths indicated that for small ice particles, the scattering increased as they melted with a converse observation for larger particles. Further study at 34.8 GHz [32] showed similar results for millimetre wavelengths, this is explained by the different backscattering cross-sections of ice and water and the proportions of water and ice present during the melting process.

2.5 Refractive Index

The refractive index of the atmosphere varies slightly from unity and can be considered on three scales [23].

- Large-scale (global)
- Medium-scale (100 m - 100 km)
- Small-scale (<100 m)

The large-scale gives rise to beam defocusing and bending, altering the apparent angle on earth-space paths. The medium scale affects the strength of millimetre waves by ducting and multi-path effects. Finally small scale changes, caused by turbulent mixing, give rise to scintillation. In this context, scintillation means rapid signal strength fluctuations. The small scale changes are caused by the wind moving larger masses of similar radio refractive index, as these move turbulence causes mixing leading to changes in the refractive index over small distances and time spans.

The refractive index is the consequence of the molecular constituents of the atmosphere, namely oxygen, nitrogen, carbon dioxide and water vapour. Its value varies from unity due to the polarisability of the molecules in the presence of an electromagnetic field. Quantum resonances also play a part at specific frequencies as discussed in Section 2.3.

The former gives rise to frequency independent variations (at the considered frequencies) in the refractive index. The absolute value of the refractive

index is close to unity, typically 1.0003 at sea level. Due to the fact that the refractive index, n, is close to unity, N, refractivity is commonly used. The refractivity is given by

$$N = (n - 1) \times 10^6 \tag{2.6}$$

N is dimensionless but is commonly referred to as 'N units'. N is dependent on pressure P (mbar), temperature T (K) and the partial pressure of water vapour e (mbar). N is formed from two terms, a wet and a dry term. The dry term is primarily the result of the non-polar nitrogen and oxygen molecules while the wet term is the result of the water vapour which is polar. These are related in the following, derived from the Debye formula [33]

$$N = N_{wet} + N_{dry} \tag{2.7}$$

where

$$N_{wet} = 3.73 \times 10^5 \frac{e}{T^2} \tag{2.8}$$

and

$$N_{dry} = 77.6 \frac{P}{T} \tag{2.9}$$

Therefore

$$N = 77.6 \frac{P}{T} + 3.73 \times 10^5 \frac{e}{T^2} \tag{2.10}$$

The constants originate from experimental results [34].
The value of e can be calculated from the relative humidity [35] thus:

$$e = H \frac{e_s}{100} \text{ hPa} \tag{2.11}$$

$$e_s = a \exp\left(\frac{bt}{t + c}\right) \text{ hPa} \tag{2.12}$$

where:

- H (%) is the relative humidity
- t (°C) is the temperature

  and, for water:
- $a = 6.11$
- $b = 17.5$
- $c = 241$

2.5.1 Large Scale Refractive Index Structure

The large-scale structure of the radio refractive index is much more constant horizontally than it is vertically. The main reason for this is the decreasing pressure with increasing altitude. The pressure drops exponentially to a fraction $1/e$ at the scale height of 8 km. Similarly, the temperature decreases with height, for dry (unsaturated) air the temperature drops 1°C/100 m. This is termed the *dry adiabatic lapse rate.*

The solution is much more complicated when the water vapour is included. In the absence of condensation the temperature would decrease exponentially with pressure. However, air can only hold a specific quantity of water at a given temperature, the limit is termed *saturated water-vapour pressure.* Beyond this point the water-vapour condenses to form clouds. Since temperature decreases with height thus the saturated water-vapour pressure decreases, condensation will occur at some height. By the process of condensation, the water-vapour content is reduced, thus water-vapour decreases more rapidly than pressure and is negligible above 2-3 km [23]. Above this height, the temperature follows the saturated adiabatic lapse rate. The saturated adiabatic lapse rate is lower than the dry adiabatic lapse rate because of the heat released by the condensation process.

The refractive index as a function of height is modelled [35] by an exponential law:

$$n(h) = 1 + N_0 \times 10^{-6} \times \exp\left(-\frac{h}{h_0}\right) \tag{2.13}$$

where

- N_0: Average value of atmospheric refractivity extrapolated to sea level
- h_0: Scale height (km)

While N_0 and h_0 can be statistically determined, global averages of $N_0 = 315$ and $h_0 = 7.35\,\text{km}$ are valid, though only for terrestrial paths.

The refractivity at the Earth's surface can thus be calculated using:

$$N_s = N_0 \exp\left(\frac{-h_s}{h_0}\right) \tag{2.14}$$

This, using the global averages, yields a gradient over the first kilometre of -40 N units, that is the gradient is -40 $N\text{km}^{-1}$.

Since the refractive index decreases with height, radio waves will be bent downwards, toward the Earth, according to Snell's Law. In addition the signal energy is spread or defocused due to differential refraction across the beam. This effect is negligible for elevation angles above 3° and is frequency independent in the band 1-100 GHz.

2.5.2 Medium-Scale Refractive Index Structure

Medium-scale refractive index variations are the result of temperature and/or water vapour pressure gradient inversions. The structure on this scale is in the form of layers. Pressure inversions can also cause layering however air moves quickly to correct this situation resulting in the refractive index varying little from its nominal value.

The modified refractive gradient, M [35], is used to determine the properties of these layers for radio propagation.

$$\frac{dM}{dh} = \frac{dN}{dh} + \frac{1}{a} \tag{2.15}$$

where

- a=6370 km, the Earth's radius.

Table 2.2: Classification of Medium Scale Layers by Modified Refractivity Gradient.

Layer Type	Modified Gradient (M/km)
Sub-refractive	$117 \leq dM/dh \leq 157$
Standard	$dM/dh = 117$
Super-refractive	$0 \leq dM/dh \leq 117$
Ducting	$dM/dh \leq 0$

For a standard atmosphere dM/dh is $117 N\text{km}^{-1}$. From this basis, the classifications in Table 2.2 are derived.

In a standard atmosphere, radio waves are, due to ray bending, bent downwards toward the Earth's surface. The curvature of the ray path however is less than the curvature of the Earth leading to a radio horizon. Different refractive gradients cause different degrees of ray bending and so the radio horizon moves. In the super-refractive case, the bending increases, extending the radio horizon and increasing the ground clearance while in the sub-refractive case the ray begins to bend upwards reducing ground clearance and the horizon for terrestrial links.

Ducting occurs when the modified gradient is below zero, which corresponds to ray bending in excess of the curvature of the Earth's surface. For ducting to occur, a layer with an anomalous refractivity must form. These layers may form at the surface or at an elevated level. These are termed surface and elevated ducts respectively.

2.5.3 Atmospheric Turbulence

Atmospheric Turbulence is the term used to describe small-scale changes in the refractive index. These changes are caused by fluctuations in pressure, humidity and temperature. These variations are centred on the mean state of the atmosphere described previously. The theory of propagation in a turbulent medium is explored in [36].

The troposphere is the lowest part of the Earth's atmosphere and it can be further split into two layers, the boundary layer and the free atmosphere.

The boundary layer extends to 100 m at the poles and 3000 m at the equator. The difference is explained by greater solar heating at the Earth's equator. Due to gravity, pressure decreases with height, thus much of the mass of the atmosphere is concentrated at low altitudes and hence approximately 75% of the mass of the atmosphere can be found in the boundry layer. In addition, almost all of the water vapour is found in the boundary layer.

The definition of the boundary layer can be more precisely stated as that part of the troposphere which is directly influenced by the presence of the Earth's surface and responds to surface forces on a time scale of an hour or less [37]. These surface forces include drag due to the surface terrain, evaporation and heat transfer. The surface effects move horizontally by means of a wind and vertically by convection.

Further subdivision can be made of the boundary layer both spatially and temporally. The lowest 10% of the boundary layer, called the surface bounday layer, contains the most significant turbulence.

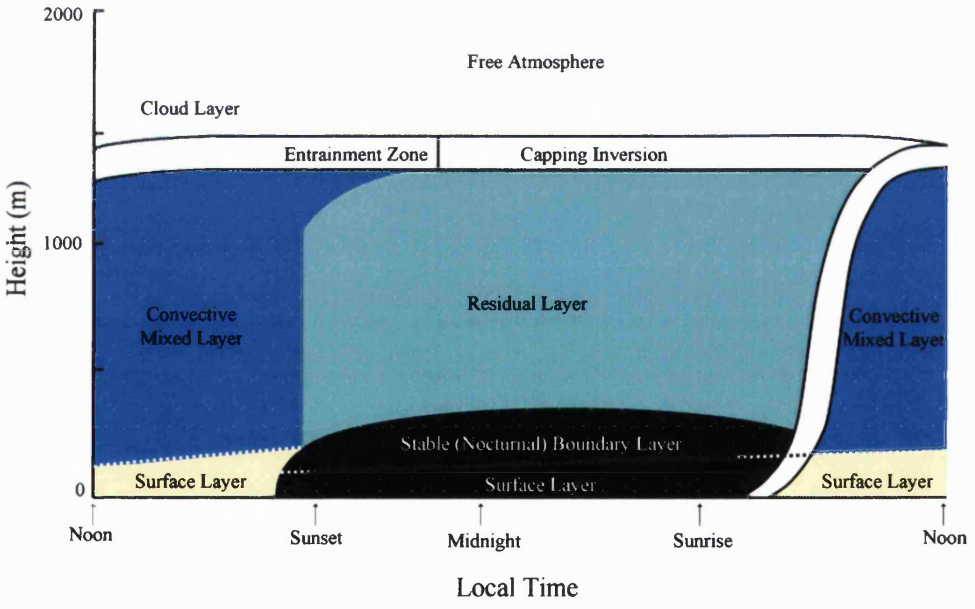

Figure 2.3: Graphical representation of the tropospheric boundary layer structure

Figure 2.3 [38] shows the surface boundary layer and its subdivisions both spatially and temporally. From this diagram, it can be seen that the convective mixed layer forms reaching a maximum depth in the late afternoon. This layer begins to form approximately half an hour after sunrise and dominates the boundary layer. Within this layer are warm thermals of air rising and cool thermals descending. This constant flow is called entrainment and it homogenizes temperature, pressure and humidity within the layer. This process is convective by nature however, at the top of the layer wind shear creates turbulence.

The growth of the mixed layer is controlled or limited by the cool thermals counteracting the rising warm thermals.

Once the sun sets, the thermal process ceases and the layer becomes the residual layer. This initially has the same characteristics of the mixed layer however as convection stops, the layer becomes neutrally stratified. Warm air thermals form a cap at the top of the layer, causing a temperature inversion.

The nocturnal boundary layer consists of statically stable air. The turbulence within this layer is sporadic in nature. While wind at ground level is usually calm with speeds of 2-10 ms^{-1}, low jets forming above 200 m can reach speeds of 10-30 ms^{-1}. While the calm air at lower altitudes suppresses turbulence, the jets cause wind shear, creating turbulence capable of causing short term effects throughout the stable boundary layer.

This large scale description of the boundary layer is sufficient for meteorological studies however for microwave propagation studies it is insufficient. It is therefore necessary to look at the small scale description of turbulent flows and energy transfer.

2.5.4 Turbulent Flows and Energy Transfer

In order to characterise turbulence and energy transfer, Kolmogorov spectrum, Taylor's 'frozen-in' hypothesis and Reynolds Numbers will be presented.

2.5.5 Kolmogorov spectrum

The spectrum describes eddies which comprise the turbulent flow. These eddies range from ~1 mm to several hundreds of metres. The spectrum as described in [39] is broken into three sections, the inner scale, sometimes called the dissipation range, the inertial sub-range and the outer scale, also known as the input range.

The input range is formed of eddies of hundreds of metres. The Kolmogorov spectrum is only valid for eddies smaller than the input range as the eddies in this range are specific to the mechanism which generated them. They cannot therefore be mathematically generalised. The Kolmogorov spectrum is thus described as a model of fully developed turbulence.

Figure 2.4 [36], in which $\Phi_n(\kappa)$ is the Kolmogorov Spectrum, shows these three ranges, where κ is the spatial wave number given by eddy size. This can be expressed mathematically as shown in Equation 2.16 [36].

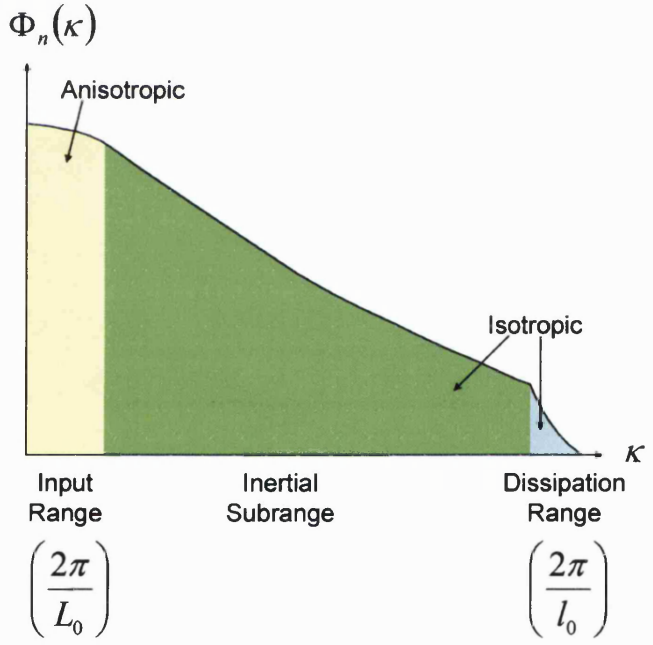

Figure 2.4: The Kolmogorov spectrum of turbulence

$$\Phi_n(\kappa) = 0.033 C_n^2 \kappa^{-11/3} \exp\left(\frac{-\kappa}{\kappa_m}\right)^2 \mathrm{m}^3 \text{ for } \kappa > 2\pi/L_0 \tag{2.16}$$

Where $C_n^2\left(\mathrm{m}^{-2/3}\right)$ is the refractive index structure function constant and $\kappa_m = 5.91/l_0$. Typical values for the refractive index structure constant are between $10^{-14}\,\mathrm{m}^{-2/3}$ for strong turbulence and $10^{-18}\,\mathrm{m}^{-2/3}$ for weak turbulence.

If two eddies are considered and are exposed to a pure shear wind flow (wind speed varies only with height), then the eddies will experience rotation. In addition to rotation, the eddies will experience a stretching force which deforms the eddies from an isotropic shape to an anisotropic shape. The eddies can thus be considered to be rotating deformable blobs. If the stretch rate is expressed as $S(k)$ then the time taken for the blob to return to isotropy [40] is $1/S(k)$ where $S(k) \propto k^{2/3}$. It is clear that large eddies will require longer to return to isotropy, they can be said to have slow strain rates. For example, an eddie of 100 m would take 6.3 s to return to isotropy while a 1 m eddie would require just 0.29 s.

Since the eddies in the input range have strain rates comparable to the mean flow, they remain anisotropic. Conversely, the smaller eddies in the inertial sub-range and dissipation range have higher strain rates and so do not form a permanent anisotropy so the mean state is isotropic.

Energy is transferred from the input range, through the inertial sub-range to the dissipation range by vortex stretching. This process occurs when smaller eddies are exposed to the strain field of a larger eddies. The rotational frequency of the smaller eddie is increased (and thus the kinetic energy) at the expense of the larger eddie. There is thus a flux of energy from large eddies to small eddies. It is suggested that this energy is more efficiently transferred when strain rates are closely correlated and thus a cascade of energy transfer is achieved from input to dissipation ranges.

2.5.6 Reynolds Number

The Reynolds number is used to quantify laminar and turbulent forces. The Reynolds number (R_e) is given in Equation 2.17 [41].

$$R_e = \frac{\rho U L}{\mu} \tag{2.17}$$

where $\rho\,(\mathrm{kg\,m^{-3}})$ is the fluid density, $U\,(\mathrm{ms^{-1}})$ is the flow speed, $L\,(\mathrm{m})$ is the characteristic flow length and $\mu\,(\mathrm{kg\,s^{-1}\,m^{-1}})$ is the viscosity.

In the boundary layer, typical values are:

- $\rho = 1.21\,\mathrm{kg\,m^{-3}}$
- $U = 5\,\mathrm{ms^{-1}}$
- $L = 100\,\mathrm{m}$
- $\mu = 1.81 \times 10^{-5}\,\mathrm{kg\,m^{-1}\,s^{-1}}$

The precise numerical value of the Reynolds number isn't significant as it is large and accurate measurement of the flow length can be difficult in practice. Large variations from unity or changes of magnitude are considered to be more significant indicators of turbulent activity.

2.5.7 Taylor's 'Frozen-in' Hypothesis

Taylor's hypothesis [42] simply states that under certain conditions, turbulence can be considered to be frozen-in. It could therefore be assumed that the structure of the eddies remained unchanged over a defined spatial range. If this is the case, time separated samples of a moving eddy taken by a single sensor, could be equated with simultaneous measurements from spatially separated sensors. Clearly for this to be the case, the eddy characteristics must evolve over a time period in excess of the time taken for the eddy to pass the single time sampling sensor.

Generally, the frozen-in hypothesis is applicable [43] when:

$$\sigma_M < 0.5U_t \tag{2.18}$$

Where σ_M is the standard deviation of the total wind speed magnitude U_t which is given by:

$$U_t = \sqrt{U_1^2 + U_2^2 + U_3^2} \ \text{ms}^{-1} \tag{2.19}$$

2.6 Effects of Turbulence on Millimetre Wave Propagation

2.6.1 Scintillation

Scintillation is the name given to rapid fluctuations in a received signal due to multi-path caused by turbulent eddies traversing the propagation path. Refractivity differences in the eddies create paths through the propagation medium of varying lengths, which in turn, lead to portions of the transmitted signal arriving at different times and therefore out of phase. These signal components constructively or destructively sum at the receiver. These rapid variations manifest themselves in both phase and amplitude. In turn these fluctuations affect calculations based on the received signal such as angle of arrival.

The signals are steered off course by the boundaries between different regions of refractive index. The signal received by an antenna is the sum of many different paths through the eddy laden atmosphere. Each component will have been perturbed by a different degree due to the differing path length it has experienced. The movement of many eddies along a propagation path leads to the rapid variations observed as the signal components constructively and destructively sum. Scintillation therefore gives rise to both spatial and temporal fluctuations in phase and amplitude.

The amplitude variations caused by scintillation can lead to significant difficulties on a radio link with increased bit-error rates, and in severe fading conditions the loss of the link altogether. In addition, a link using high power as an outage mitigation technique could interfere with other systems due to scintillation enhancement.

2.6.2 First Fresnel Zone

As with any line-of-sight radio link, the first Fresnel zone is of major significance. In terms of scintillation it is also of significance as there is a relationship between eddy size and the first Fresnel zone size.

The first Fresnel zone is given [23] by

$$f_1 = 2\sqrt{\frac{\lambda d_1 d_2}{d_1 + d_2}}\ \text{m} \tag{2.20}$$

where d_1 and d_2 are the distances from a point on the Fresnel zone ellipsoid to the receiver and transmitter respectively. The Fresnel zone being an ellipsoid with foci at the receiver and transmitter, therefore reaches a maximum exactly half way between the two, e.g. when $d_1 = d_2$.

The equation can therefore be simplified at this point to:

$$f_1 = \sqrt{\lambda d} \tag{2.21}$$

where $d = d_1 = d_2$.

Tatarski [36] used the Kolmogorov spectrum, a constant term and spectral filters to describe the relationship between eddy size and observed signal fluctuations. The equations for amplitude and phase are:

$$F_\chi(\kappa) = \pi k^2 L \left(1 - \frac{k}{\kappa^2 L}\sin\frac{\kappa^2 L}{k}\right)\Phi_n(\kappa) \tag{2.22}$$

$$F_s(\kappa) = \pi k^2 L \left(1 + \frac{k}{\kappa^2 L}\sin\frac{\kappa^2 L}{k}\right)\Phi_n(\kappa) \tag{2.23}$$

where L (m) is the path length.

These two equations are constructed from a constant term, $\pi k^2 L$, the Kolmogorov Spectrum, $\Phi_n(\kappa)$, and a spectral filter, contained within the brackets in Equations 2.22 and 2.23. The filters show that different sizes of eddy have different effects on the spectral density of the signal fluctuations.

The filter responses given in Figure 2.5 show that at the point κ_0 there is a response of unity. The value of κ at this point is 0.41m^{-1} which corresponds to an eddy of 15 m as $\kappa = (2\pi/\text{eddy size})$. From this point it is clear that

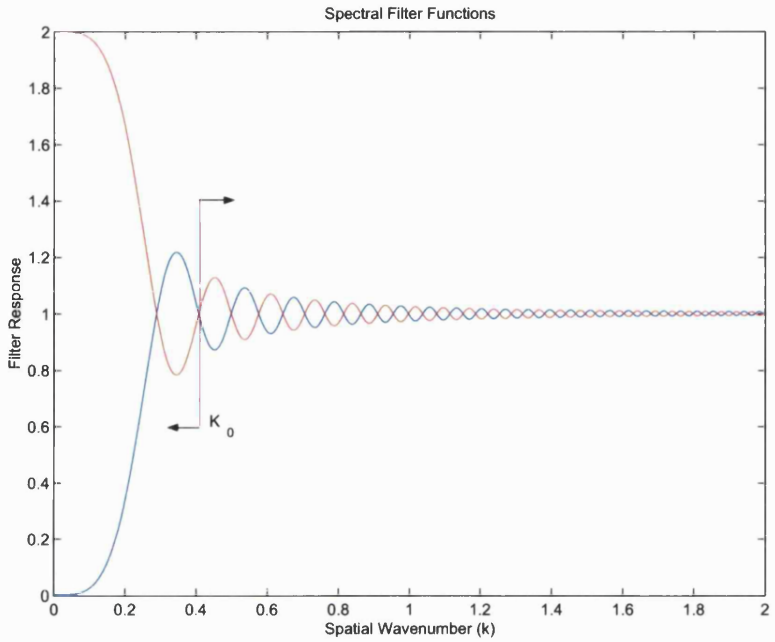

Figure 2.5: Amplitude and phase spectral filter responses

small eddies correspond to higher spatial wave numbers and larger eddies correspond to lower. The filter responses for amplitude and phase are the opposite to each other. For example, smaller eddies result in greater phase fluctuation but less amplitude fluctuation.

The maximum size of the first Fresnel zone of a 28.6 km link[1] is ~15 m corresponding to the value of κ_0 used. This value forms a boundary condition between eddies which have an effect on fluctuation density.

The product of the spectral filters and the Kolmogorov Spectrum depends on the size of the first Fresnel zone in relation to the inner and outer scales of turbulence. There are three conditions;

- $\sqrt{\lambda L} << l_0$
- $l_0 << \sqrt{\lambda L} << L_0$
- $L_0 << \sqrt{\lambda L}$

[1]This is the length of the experimental link established for this study.

The first condition is not practical for sub-optical frequencies. The path length would have to be less than 1mm for a Ka-Band link. Similarly the effects of eddies larger than the outer scale of turbulence cannot be assessed as no models exist which account for the outer scale of turbulence.

The condition of interest is therefore the second where the size of the first Fresnel zone is between the inner and outer scales of turbulence. At the point where the eddy size equals the first Fresnel zone size, the amplitude spectral density reaches a maximum. Tatarski's correlation model states that this can be mitigated by spatially separating antennas by a greater distance than the first Fresnel zone.

2.6.3 Interferometry

Interferometry is a technique, with origins in astronomy stemming from the Michaelson Interferometer [44] which uses two or more antennas in an array configuration to synthesize a larger aperture, allowing more detailed study of fine detail of a wavefront incident upon the receivers. Similarities between radio and optical radiations fields have meant that experience gained from optical interferometry has fed into radio interferometry.

Early interferometers added the signals from two or more antennas and fed the resulting signal into a square-law detector (Figure 2.6). The result of which is proportional to $(V_1 + V_2)^2$. This suffered from problems of noise as the output was comprised of both noise and signal components, often where the background noise power exceeded the signal power. To mitigate this, a technique called phase-switching interferometry (Figure 2.7) was developed. In this scheme, the phase of one antenna signal is periodically reversed by inserting a $\lambda/2$ delay. This delay typically being switched in and out at a rate of a few tens of Hertz [44]. This results in the input to the square-law detector alternating between $(V_1 + V_2)^2$ and $(V_1 - V_2)^2$, a synchronous detector is used to take the difference of these terms. Thus the output of a phase-switched interferometer is the time average of the product of the signals which is proportional to $V_1 V_2$. This is the cross-correlation of the signals and in modern interferometers the device responsible for performing

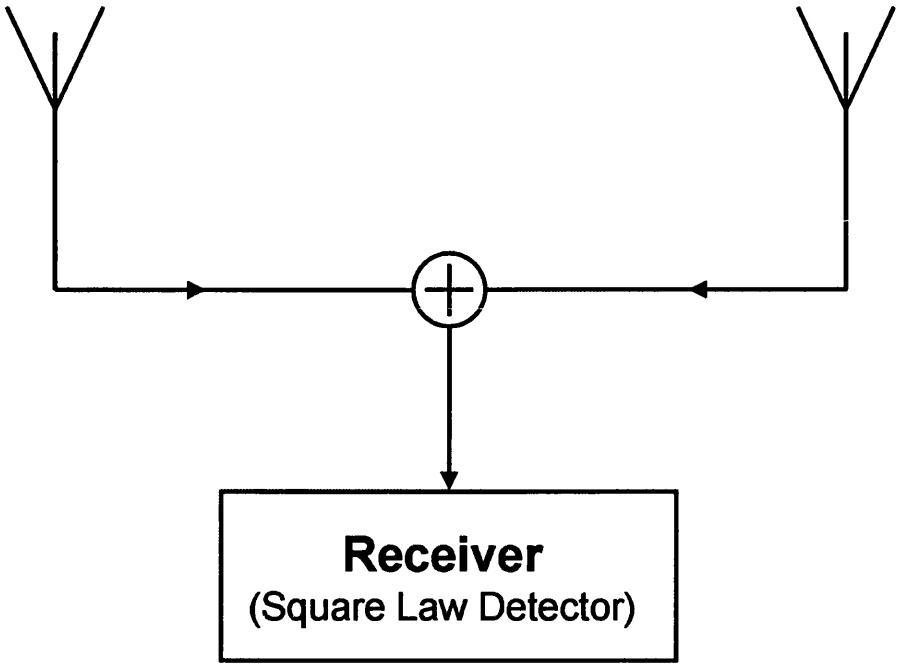

Figure 2.6: Functional diagram of a simple adding interferometer

the multiplication and averaging is a correlator.

This development made the introduction of amplification into the system possible in turn allowing larger, more widely spaced arrays to be built. The phase switching is no longer necessary to achieve the voltage multiplication however it is sometimes included to assist with the elimination of imperfections within the equipment. Figure 2.8 shows this arrangement.

One of the most important measurements interferometers can make is Angle of Arrival (AOA) which comes under the broader heading of radio direction finding.

For simplicity and for visualization purposes the 2-dimensional planar case will be examined and is shown in Figure 2.9. This assumes a single distant point source in the far-field of the interferometer, radiating toward it at an angle to the normal, θ. The wave front can therefore be considered to be a plane wave which will reach one antenna before another. This difference in path length will give rise to a phase difference between the signal received

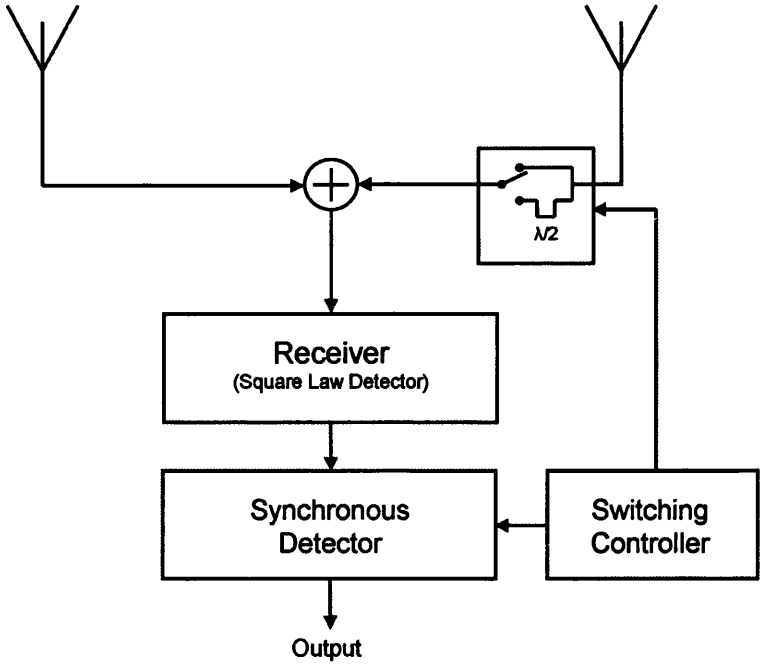

Figure 2.7: Functional diagram of a switching interferometer

at the two antennas.

This is the idealised case, in reality, small scale turbulence (scintillation) causes wave-front distortion which introduces variations in the measured phase. Similarly, under certain refractive index conditions the wave-front, although normal to the array axis under homogeneous conditions, arrives at an angle to the normal due to ray bending.

Looking at the operation of an interferometer in more detail again using the 2D geometric approach in Figure 2.9. The phase angle seen between the received signals from two antennas is directly related to the angle of arrival. Using simple trigonometry, the baseline D forms the hypotenuse of the right-angled triangle ABC. This gives the length AC as $D\sin\theta$. This length can then be converted to a phase by multiplying by $\frac{2\pi}{\lambda}$ thus:

$$\phi = \frac{2\pi D\sin\theta}{\lambda} = \frac{2\pi f D\sin\theta}{c} \tag{2.24}$$

It should be obvious that if the antenna separation D is varied for a

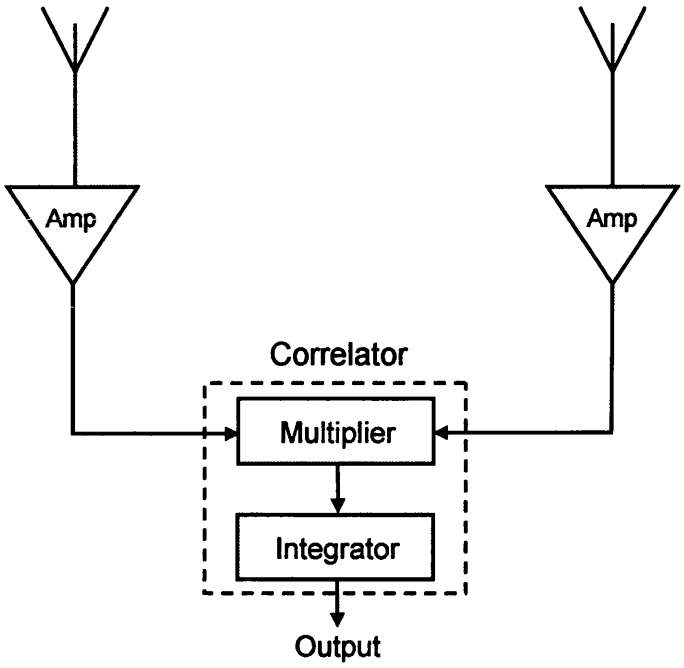

Figure 2.8: Functional diagram of an interferometer with a correlator

constant wave front, the phase ϕ will vary in a sinusoidal fashion. Thus the same apparent phase would be measured with a set of separation distances. This phase wrapping leads to an ambiguity so for a fixed separation D, the measured AOA aliases. To mitigate this ambiguity it is necessary to reduce the separation D to λ or less. With millimetre wavelengths this becomes difficult because the size of the receive antennas are often many wavelengths in diameter, physically preventing such close spacing.

For the link in this study, the wavelength is 8.2 mm. Rearranging and using Equation 2.24 with a phase shift of 2π shows that aliasing will occur at an AOA of 0.24°.

So far it has been established that to resolve ambiguity, close spacing of the receiving antennas is necessary however there is another method for resolving ambiguity. This second method examines the output of the antennas for components of the same received signal which differ in frequency.

The former technique called 'phase-difference-interferometry' will be the

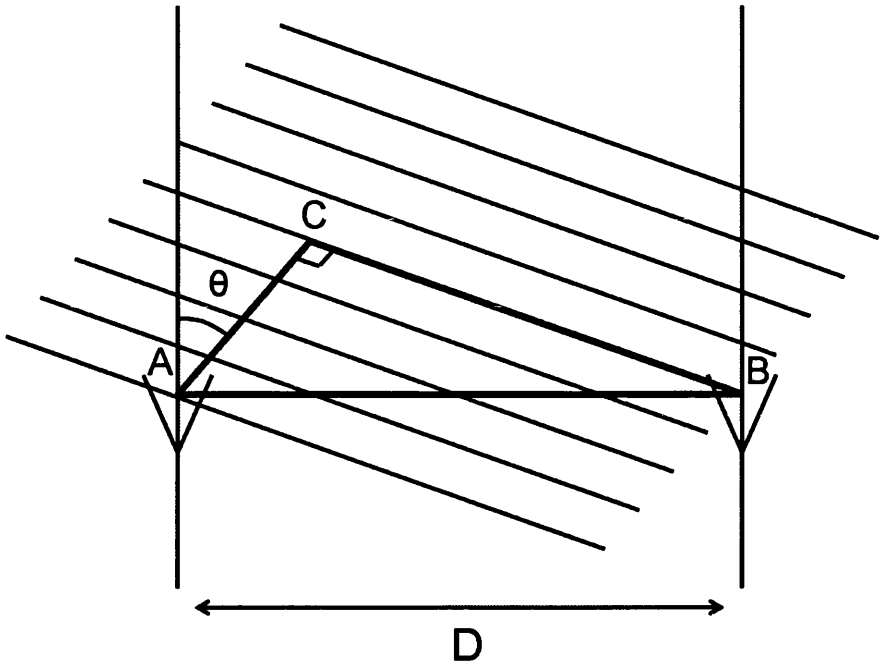

Figure 2.9: Elementary interferometer geometry

technique of discussion here though.

Widely spaced antennas can provide a more accurate measurement of the phase difference. The measurements will include an integer number of 2π multiples which cannot be resolved directly however they can be by combining both measurement types. This method is termed 'hybrid interferometry' [45].

The AOA is determined 'coarsely' by a closely spaced pair of receivers giving an unambiguous measurement and then a 'fine', ambiguous measurement is taken using widely spaced receivers. Together the measurements lead to the measured AOA.

In the case of high frequencies the completely unambiguous measurement isn't possible due to antenna size. However a range of antenna spacings allows some ambiguity to be removed.

It is important to introduce the concept of fringe angles, lobes of interferometer response. Following the mathematical approach of [44] and recalling

that in a correlating (or phase switching) interferometer the output is proportional to $V_1 V_2$ we derive the fringe function.

Defining the time delay between the wavefront reaching the two antennas as $\tau_g = \left(\frac{D}{c}\right) \sin\theta$ the output of the correlator is then proportional to

$$F = 2\sin(2\pi ft)\sin 2\pi f(t - \tau_g) \tag{2.25}$$

This can be manipulated thus:

$$F = 2\sin(2\pi ft)\sin(2\pi ft - 2\pi f\tau_g)$$

Using $\sin(A - B) = \sin A\cos B - \sin B\cos A$

$$F = 2\sin(2\pi ft)\left(\sin(2\pi ft)\cos(2\pi f\tau_g) - \sin(2\pi f\tau_g)\cos(2\pi ft)\right)$$

Simplifying and using $\sin 2A = 2\sin A\cos A$

$$F = 2\sin^2(2\pi ft)\cos(2\pi f\tau_g) - \sin(4\pi ft)\sin(2\pi f\tau_g)$$

Using $\sin^2 A = \frac{1-\cos 2A}{2}$ and multiplying out yields

$$F = \cos(2\pi f\tau_g) - \cos(4\pi ft)\cos(2\pi f\tau_g) - \sin(4\pi ft)\sin(2\pi f\tau_g)$$

Considering that the higher frequency terms are easily filtered out, this leaves the fringe function F.

$$F = \cos(2\pi f\tau_g) = \cos\left(\frac{2\pi D\sin\theta}{\lambda}\right) \tag{2.26}$$

Figure 2.10 [44] shows a simple case where $\frac{D}{\lambda} = 3$. Alternate lobes give rise to positive and negative interferometer output as indicated on the diagram. This pattern assumes source tracking by the antennas or isotropic responses,

directional antennas clearly differ from this pattern. The fringe patten can be thought of as the interferometers directional power reception pattern.

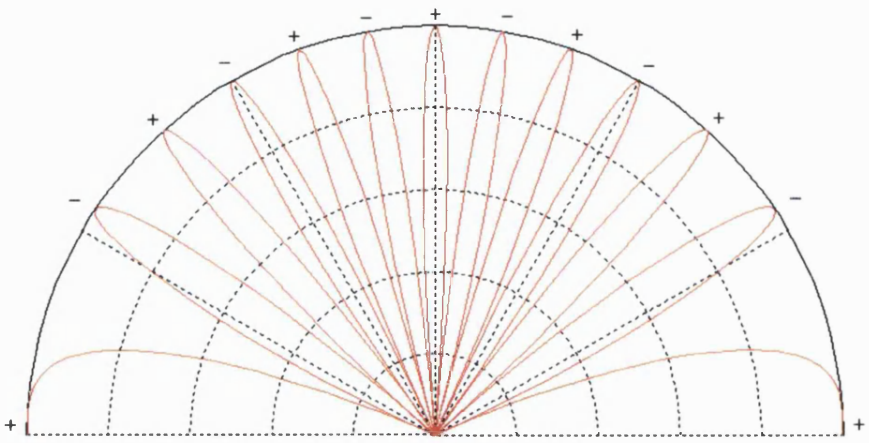

Figure 2.10: Polar plot of Equation 2.26, the interferometer fringe function

Summary

This chapter has introduced propagation through the Troposphere and examined the effects of various hydrometeors. The refractive index and its various scales have been considered together with turbulence.

Energy flows within turbulence have been discussed through the consideration of the Kolmogorov spectrum, Reynolds number and Taylor's 'Frozen-in' hypothesis. The effects of turbulence on millimetre wave propagation were then considered. Finally interferometry has been introduced by examining the principle and how the design of interferometers has developed.

Chapter 3 moves on to look at how propagation through the Troposphere can be modelled.

Chapter 3

A review of Propagation Modelling Techniques

This chapter introduces the Parabolic Equation method and the approaches taken to its calculation in the modelling of radio wave propagation. The chapter also considers the ray optics method for calculating radio wave propagation.

3.1 The Parabolic Equation

The PE is an approximation of the wave equation. Introduced initially to model the diffraction of radio waves around the Earth [46], the method soon found other applications after the advent of digital computers in waterwave propagation and geophysics [47],[48],[49],[50],[51].

Much earlier than this though, the PE was used in problems involving atmospheric refraction. The need for approximations to Maxwell's equations are due to the very large domains being considered in relation to relatively small wavelengths. Early methods involved geometrical theory, commonly called geometric optics, these were superseded by the numerically more efficient PE

Several different implementations soon emerged including split-step / Fourier and finite-difference algorithms [52]. Researchers soon realised that the PE could cope with cases outside the flat terrain and sea cases on which

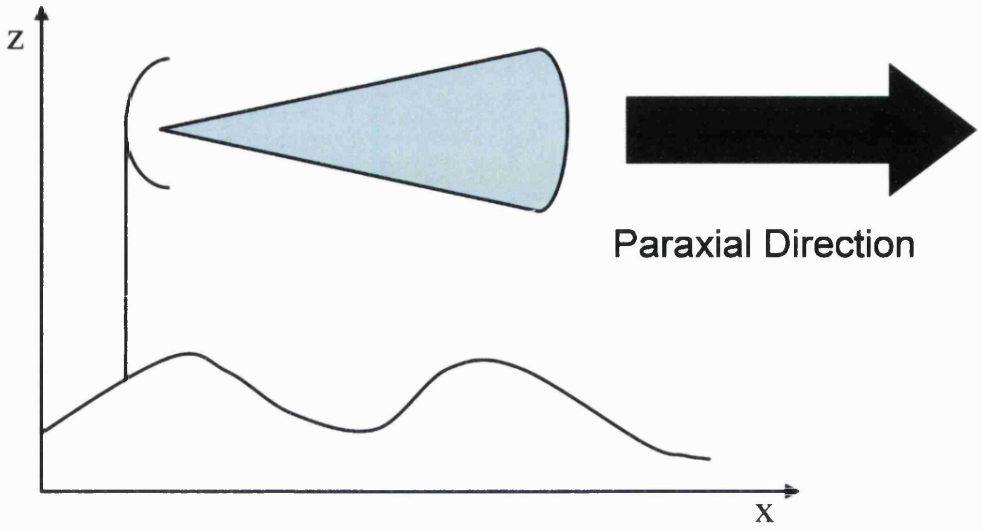

Figure 3.1: Narrow angle paraxial propagation in the troposphere

they were initially used. Once the PE became widely used on more complex cases, the issue of computational speed came to the fore. The answer to this problem was the hybrid model. These models combine the geometric optics approach with the PE to provide fast solutions to complex propagation cases.

3.1.1 Basic PE Derivation

Referring to Figure 3.1 which shows a basic propagation case and taking the approach of [52], the reduced function for propagation, u, in a paraxial cone is:

$$u(x,z) = e^{-ikx}\psi(x,z) \tag{3.1}$$

where ψ is the field component, k is the wave number, $i = \sqrt{-1}$, x is the range from the radio source and z is height. This function varies slowly with distance x for energy propagating in or at angles close to the paraxial direction leading to mathematical convenience.

The scalar wave equation in terms of u is

$$\frac{\partial^2 u}{\partial x^2} + 2ik\frac{\partial u}{\partial x} + \frac{\partial^2 u}{\partial z^2} + k^2\left(n^2 - 1\right)u = 0 \tag{3.2}$$

Which can be factorised [52] thus

$$\left\{\frac{\partial}{\partial x} + ik\left(1 - Q\right)\right\}\left\{\frac{\partial}{\partial x} + ik\left(1 + Q\right)\right\}u = 0 \tag{3.3}$$

where

$$Q = \sqrt{\frac{1}{k^2}\frac{\partial^2}{\partial z^2} + n^2\left(x, z\right)} \tag{3.4}$$

From the factorisation it is possible to split the wave equation into two terms, one corresponding to forward and one to backward propagation. The forwards term is

$$\frac{\partial u}{\partial x} = -ik\left(1 - Q\right)u \tag{3.5}$$

Using first-order Taylor expansions of the square root and exponential functions, it is possible to derive the simplest approximation of Equation 3.5 thus

$$\frac{\partial^2 u}{\partial z^2}\left(x, z\right) + 2ik\frac{\partial u}{\partial x}\left(x, z\right) + k^2\left(n^2\left(x, z\right) - 1\right)u\left(x, z\right) = 0 \tag{3.6}$$

This is the Standard Parabolic Equation (SPE) which is useful for solving long range tropospheric propagation problems however it suffers problems handling large propagation angles. This equation forms the basis of implementations of PEs in propagation cases which cannot be solved using Fourier transform techniques.

3.1.2 Split-Step PE

The split-step method for solving the PE leads to a numerically efficient solution however it doesn't behave well at the domain boundaries. This approach is best suited to cases where the field is defined at zero height. This case forms the basis of a whole class of propagation cases, namely those

over the sea.

Recasting the SPE

$$\frac{\partial u}{\partial x} = \frac{ik}{2}\left\{\frac{1}{k^2}\frac{\partial^2}{\partial z^2} + \left(n^2(x,z) - 1\right)\right\}u \tag{3.7}$$

Applying the Fourier transform directly in height to this yields a convolution term involving the Fourier transform of the refractive profile. To achieve a simple solution it is therefore necessary to consider the refractivity term separately. This leads to two cases, the range dependent and range independent. Only the latter will be presented here.

With range independent refractivity, n depends only on height z. The solution can therefore be expressed as.

$$u(x + \Delta x, z) = e^{\delta(A+B)} \cdot u(x,z) \tag{3.8}$$

where

$$A = \tfrac{1}{k^2}\tfrac{\partial^2}{\partial z^2}$$

$$B = n^2(z) - 1$$

$$\delta = \tfrac{ik\Delta x}{2}$$

The aim is to split the two terms in the exponent, the simplest split being

$$S_1 = e^{\delta B}e^{\delta A} \tag{3.9}$$

This commutes only for a homogeneous medium, that is one in which the refractive index doesn't change with height (in addition to range). If the refractive index does change with height then

$$\frac{\partial^2\left\{\left(n^2 - 1\right)u\right\}}{\partial z^2} \neq \left(n^2 - 1\right)\frac{\partial^2 u}{\partial z^2} \tag{3.10}$$

However, if the refractive index varies slowly with height then the error introduced by splitting the exponent terms up will remain small. More accurately the commutator can be stated:

$$[A, B] = AB - BA \tag{3.11}$$

from the earlier definition of A and B

$$[A, B]\, u = -\frac{1}{2k^2}\left(\frac{\partial^2 n^2}{\partial z^2} u + 2\frac{\partial n^2}{\partial z}\frac{\partial u}{\partial z}\right) \tag{3.12}$$

The error resulting from the split is

$$E = e^{\delta B} e^{\delta A} - e^{\delta(A+B)} \tag{3.13}$$

Expanding this using Taylor series, it is possible to express this error in terms of Δx, the dominant error term in that series can be written as

$$\epsilon = \frac{k^2}{8}(\Delta x)^2 [A, B] \tag{3.14}$$

This shows that the error is of second order in the range step. From Equation 3.12 it is clear that the error also depends on height variations of refractive index. The split step solution can now be expressed as

$$u(x + \Delta x, z) = e^{\delta B} \cdot \left\{e^{\delta A} \cdot u(x, z)\right\} \tag{3.15}$$

The split step solution can be visualised as a field propagating through a series of phase screens. The field first propagates through a homogeneous medium represented by term A and then a phase screen modulated by the refractivity index variations, term B. This is shown in Figure 3.2. This split separates the diffractive (A) and refractive (B) effects.

In Figure 3.2 the free-space propagator is $\exp\left(\frac{i\Delta x}{2k}\frac{\partial^2}{\partial z^2}\right)$ and the phase screens are $\exp\left(\frac{ik\left(n^2-1\right)\Delta x}{2}\right)$.

This, the simplest split, is adequate for most radio propagation problems. However, for underwater acoustics where sound speed gradients can be large, a split with an error of 3rd order in Δx is necessary. Such a split is

$$S_2 = e^{\frac{1}{2}\delta B} e^{\delta A} e^{\frac{1}{2}\delta B} \tag{3.16}$$

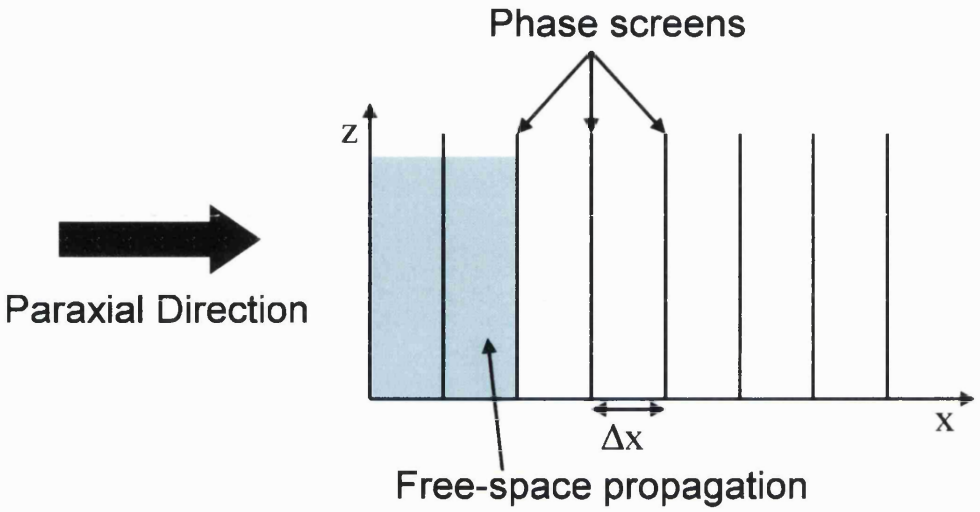

Figure 3.2: Phase screen visualisation of the split step PE solution

3.1.3 Finite-Difference PE

Finite-difference algorithms are used where complex boundaries exist. This technique is also suited to scattering cases (object scattering) where the domain size in question can be significantly smaller and therefore computational efficiency is a lesser consideration.

The implementation presented here is also taken from [52] and is of the Crank-Nicolson type.

The first assumption is that the lower boundary is located at $z = 0$ and is horizontal. The integration grid is defined as being fixed in the vertical direction but not by range. This allows it to adapt to terrain profile.

Let

$$z_j = j\Delta z, \qquad j - 0, N \tag{3.17}$$

be the vertical grid points (see Figure 3.3) and $x_0, ..., z_m, ...$ be the successive range points. To advance the solution from range x_{m-1} to x_m we consider the midpoint

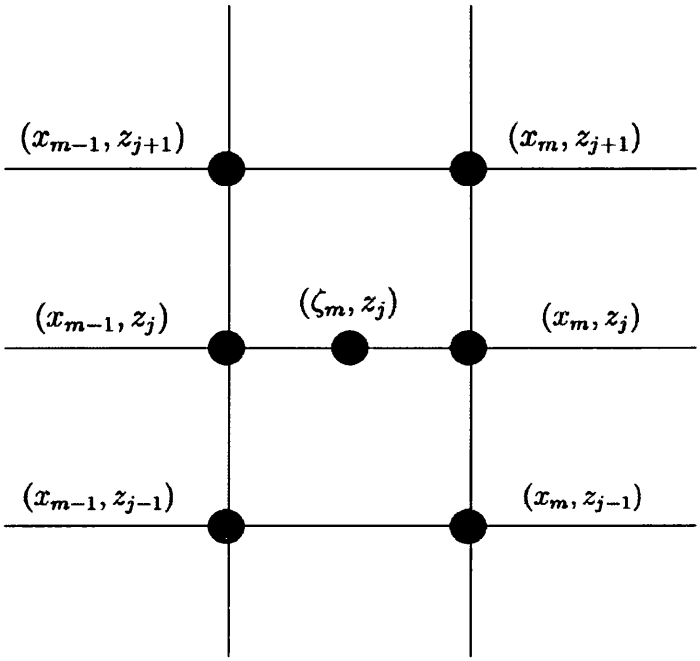

Figure 3.3: Finite-difference grid for the Crank-Nicolson scheme

$$\xi_m = \frac{x_{m-1} + x_m}{2} \tag{3.18}$$

The aim is to create expressions for the partial derivatives at point $(\xi_m, \_j)$ based on values of the function u at adjacent grid locations, see Figure 3.3. The central finite-difference approximation in range is

$$\frac{\partial u}{\partial x}(\xi_m, z_j) \sim \frac{u(x_m, z_j) - u(x_{m-1}, z_j)}{\Delta x_m} \tag{3.19}$$

where

$$\Delta x_m = x_m - x_{m-1} \tag{3.20}$$

Taylor series expansion reveals the error of this approximation is of the order of $(\Delta x_m)^2$. The central finite-difference approximation in height is

$$\frac{\partial^2 u}{\partial z^2}(\xi_m, z_j) \sim \frac{u(\xi_m, z_{j+1}) + u(\xi_m, z_{j-1}) - 2u(\xi_m, z_j)}{\Delta z^2} \tag{3.21}$$

The error in this approximation of of the order of $(\Delta z)^4$. Worth of note is the limitation of this approximation in that it only holds while j is not 0 or N. Thus additional expressions are necessary to accommodate the boundary conditions.

Combining Equations 3.19 and 3.21 with the SPE gives

$$\frac{u(\xi_m, z_{j+1}) + u(\xi_m, z_{j-1}) - 2u(\xi_m, z_j)}{\Delta z^2} + 2ik\frac{u(x_m, z_j) - u(x_{m-1}, z_j)}{\Delta x_m} + k^2\left(n^2(\xi_m, z_j) - 1\right)u(\xi_m, z_j) = 0 \quad (3.22)$$

By averaging the values at the ranges x_{m-1} and x_m we reach an approximation for ξ_m

$$u_j^m = u(x_m, z_j) \quad (3.23)$$

$$b = 4ik\frac{\Delta z^2}{\Delta x} \quad (3.24)$$

$$a_j^m = k^2\left(n^2(\xi_m, z_j) - 1\right)\Delta z^2 \quad (3.25)$$

which gives

$$u_j^m\left(-2 + b + a_j^m\right) + u_{j+1}^m + u_{j-1}^m = u_j^{m-1}\left(2 + b - a_j^m\right) - u_{j+1}^{m-1} - u_{j-1}^{m-1} \quad (3.26)$$

for j=1,...,N-1. This gives N-1 equations. To complete the solution, two more expressions corresponding to the top and bottom of the domain are necessary. The simplest approach is to assume a perfectly conducting ground imposing $u(x, z_N) = 0$ and an absorbing layer at the top to prevent parasitic reflections.

So far, the values at range x_m have been given in the form of a linear system. In order to obtain u at x_m, we have to perform a matrix inversion. Mathematically this is expressed as

$$A_m U_m = V_m \tag{3.27}$$

where U_m is a vector of the field at range x_m

$$U_m = \begin{pmatrix} u_0^m \\ \vdots \\ u_N^m \end{pmatrix} \tag{3.28}$$

and A_m is the tridiagonal matrix

$$A_m = \begin{pmatrix} 1 & 0 & 0 & 0 & 0 & \dots & 0 & 0 \\ 1 & \alpha_1^m & 1 & 0 & 0 & \dots & 0 & 0 \\ 0 & 1 & \alpha_2^m & 1 & 0 & \dots & 0 & 0 \\ \vdots & & & & & & & \vdots \\ 0 & \dots & & & & 1 & \alpha_{N-1}^m & 1 \\ 0 & \dots & & & & 0 & 0 & 1 \end{pmatrix} \tag{3.29}$$

where

$$\alpha_j^m = -2 + b + a_j^m \tag{3.30}$$

The term V_m is obtained from U_{m-1}, the field at the previous range step, by means of the matrix multiplication

$$V_m = \begin{pmatrix} 1 & 0 & 0 & 0 & 0 & \dots & 0 & 0 \\ -1 & \beta_1^m & -1 & 0 & 0 & \dots & 0 & 0 \\ 0 & -1 & \beta_1^m & -1 & 0 & \dots & 0 & 0 \\ \vdots & & & & & & & \vdots \\ 0 & \dots & & & 0 & -1 & \beta_{N-1}^m & -1 \\ 0 & \dots & & & & 0 & 0 & 1 \end{pmatrix} U_{m-1} \tag{3.31}$$

where

$$\beta_j^m = 2 + b - a_j^m, \qquad j = 1, \dots, N-1 \tag{3.32}$$

The matrix A_m is tridiagonal thus inversion with a Gaussian elimination

scheme is straightforward provided A_m is non-singular. Index m has been omitted for simplicity. In the first of two sweeps, the lower sub-diagonal is eliminated with a forward loop.

$$\Gamma_0 = \frac{v_0}{\alpha_0}\Gamma_j = \frac{V_j - \Gamma_{j-1}}{\alpha_j}, \qquad j = 1, \ldots, N \tag{3.33}$$

The upper sub-diagonal is then eliminated using a back-solving loop giving the solution

$$U_N = \Gamma_N U_j = \Gamma_j - \frac{U_{j+1}}{\alpha_j}, \qquad j = N-1, \ldots, 0 \tag{3.34}$$

The number of operations is N, the Crank-Nicolson scheme therefore has good numerical properties.

3.2 Geometrical Optics

Geometrical Optics or Ray Shooting formed the basis of early models and do still play a significant part in hybrid propagation models. Their main advantages are speed and simplicity. They do not model diffraction and they in general do not give a good indication of field strength however they do provide a qualitative picture of propagation. They can additionally yield wave polarisation.

Geometrical Optics rely on two assumptions:

- The wavelength is small, thus wavenumber, k, is high.
- The wave is observed far away from the source

This approach also gives a good indication of the angle of propagation in environments in which changes in refractivity are smooth and continuous. This is particularly useful in determining angle dependent reflection effects.

Snell's law is probably the most obvious approach to take when evaluating propagation along a terrestrial link. Snell's law simply stated is;

$$n_1 \sin\theta_1 = n_2 \sin\theta_2 \tag{3.35}$$

Where n_1 and n_2 are the refractive index of medium 1 and 2 respectively. The angles θ_1 and θ_2 are the angles of incidence and refraction made by the wave to the normal at the interface between the two mediums of different refractive index. This is more easily understood when visualised, for such a representation see Figure 3.4.

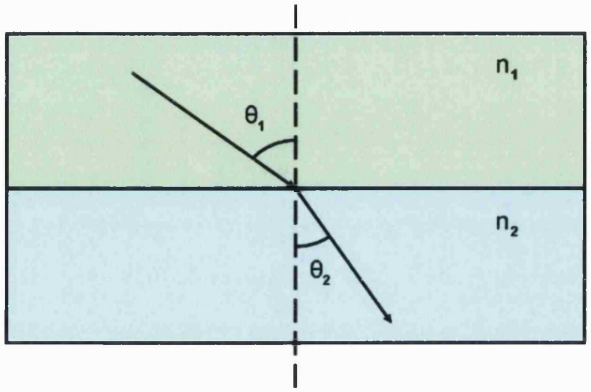

Figure 3.4: Illustration of Snell's Law

The assumptions for terrestrial radio propagation are that the propagation media is horizontally stratified, n, the refractive index, varies with height and at each boundary which the ray meets, Snell's law is applied. Clearly as n generally decreases with increasing height, the angle on the RHS of the equation increases, bending the ray toward the horizontal. Anomalies in the refractivity profile give rise to bending both toward and away from the horizontal.

This technique is relatively simple to implement however care must be taken as the angle approaches the horizontal. If the algorithm uses a fixed height step as defined by the stratified atmosphere, the horizontal step calculated using the angle can become excessively large.

Snell's law also describes ducting inversion and case where a radio wave is reflected by one or more interfaces between layers of differing refractive index. At some incident angle θ_c, referred to as the critical angle, the refracted ray makes an angle of 90° to the normal. If the incident ray makes a greater angle to the normal line then reflection occurs. As already noted, when

a ray crosses a boundary towards a medium of lower refractivity, it bends away from the normal hence why in an atmosphere of smoothly reducing refractivity with increasing height, radio waves are bent downwards. Figure 3.5 illustrates the refractive, critical and total reflection cases.

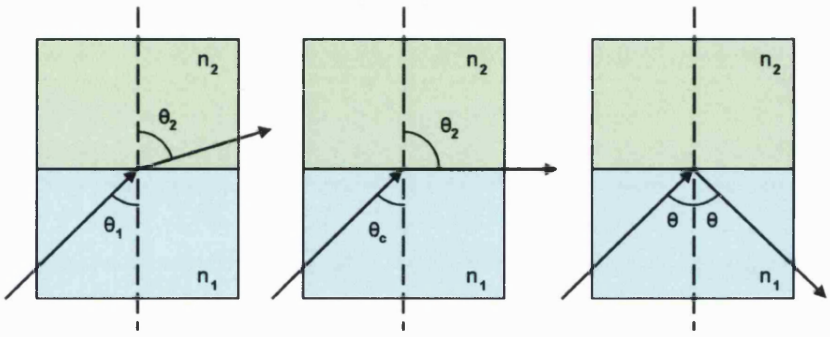

Figure 3.5: Refractive, critical angle and total reflection cases for ray passing from higher refractive index medium to a lower one.

In the case of ducting, the angle of incidence at two refractive index boundaries meets and exceeds the critical angle causing the ray to repeatedly reflect of the boundaries as it propagates. These cases are usually formed by a single band of anomalously high refactivity. Total reflection can only occur when the ray is moving from a medium of high refractivity to a medium of lower refractivity.

In the case of radio wave propagation, it is the refractivity which alters to create ducting or capping conditions. The critical angle may be determined using Equation 3.36.

$$\theta_c = \arcsin\left(\frac{n_2}{n_1}\right) \tag{3.36}$$

Summary

This chapter has reviewed the PE and several methods used to implement its application to tropospheric propagation problems. Geometric Optics have also been considered.

For a full description of Parabolic Equation methods and implementations see [52]. Presented here are reproductions of relevant portions of the mathematical background to accompany the written descriptions of the methods.

Chapters 4 and 5 will introduce the experimental equipment and the work carried out to prepare it for use. Later, Chapter 6 will go on to discuss an implementation of the PE.

Chapter 4

Design and Implementation of Propagation Experiment - Transmitter

This chapter and the next, describe the equipment used for this study. There is a logical split between the transmitter and the receive array with each chapter considering one.

The equipment as supplied from its previous use in a propagation experiment, was not ideally suited to a long term data collection campaign, certainly not in the field with a remotely sited transmitter. The previous study established a link between two buildings, consequently the more sensitive equipment could be housed indoors. The necessary work undertaken to prepare the equipment for the experimental link used in this study is described in detail, particular emphasis is placed on the aspects to the work which introduced new hardware and software to the design.

4.1 Hardware Description

The equipment used in this study consists of a Continuous Wave (CW) transmitter and a five element superheterodyne multiple configuration receiver array. The transmitter produces a CW signal at 36.57 GHz which the receive array elements detect, down convert and amplify. The Intermediate Frequency (IF) signals are further down converted, filtered and amplified be-

fore demodulation within the Demodulation Unit (DU). The DU uses one channel as a reference to which all the other signals are compared, the result is N-1 difference In phase, Quadrature phase - (I/Q) signal pairs where N is the number of receive array elements. These signal pairs are captured using an Analogue to Digital (A/D) converter (Microstar Laboratories iDSC1816) capable of sampling all eight of its input channels simultaneously.

The DU also meets all the power derivation, conditioning and distribution needs of the array. This is in addition to producing the two Local Oscillator (LO) frequencies for the down conversions at 17.43 GHz and 1570 MHz and outputting the line driven Direct Current (DC) signals for the A/D converter.

By making relative measurements, rather than absolute, this design approach offers the considerable advantage of making the measurements independent of the actual path lengths within the equipment.

4.2 Transmitter Overview

The transmitter unit was originally designed as an up-converter. Requiring a reference signal (nominally 10 MHz) and an IF signal from external sources to operate it was not suitable for immediate deployment. During the previous study [38] it was sited indoors where a laboratory signal generator was used to supply both the reference and IF signals. With no such equipment available for this study in the field, the transmitter needed to be modified to incorporate an on board signal generator enabling it to become a self-contained unit. The transmitter also needed to be made weatherproof as its original housing consisted of a standard vented laboratory instrument case and a canvas splash-proof cover. While this type of case is not suitable for outdoor use, the case was fitted with a tripod mounting bracket enabling it to be easily sited and aligned with the receiver array, which by comparison is immobile and extremely hard to align. This mounting method was retained in the design of the new case.

In order to produce the 36.57 GHz on which this experiment is based, the transmitter uses a Phase Locked Dielectric Resonator Oscillator (PDRO). The block diagram in Figure 4.1 shows the Transmitter Design. The PDRO

synthesizes an 11.43 GHz signal using the 10 MHz reference. The PDRO can in fact operate from a reference signal between 1 and 100 MHz which offers a degree of flexibility however 10 MHz is a commonly used reference and is easily obtainable. The 11.43 GHz signal is tripled, filtered and mixed with an IF of 2.28 GHz. The lower frequency image is rejected and the 36.57 GHz is amplified and transmitted.

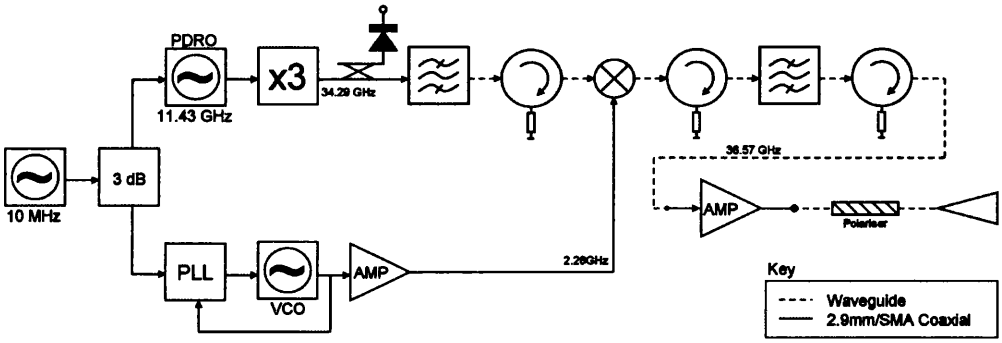

Figure 4.1: Block diagram of transmitter

The transmission is by means of a weatherproofed lens horn antenna with a beam width of approximately 2° and is feed by means of a circularly polarizing waveguide transition. Circular polarisation was used for ease of receiver/transmitter alignment.

The transmitter operates from a 24 V DC power supply, requiring 4.1 A at start up and 2.5 A while transmitting thereafter.

4.3 2.28 GHz Intermediate Frequency Generation

The first modification necessary involved the addition of a 2.28 GHz signal generator to the transmitter. The design aim was to fit this within the existing case to retain the option of tripod mounting and single unit installation. The case had considerable space remaining within it however very little mounting space on the base plate. The solution adopted was to introduce an aluminium plate, fitting into preformed grooves on the sides of the case.

This plate covers approximately 75% of the depth of the case, the lens horn antenna limiting this. The plate can be seen in Figure 4.2.

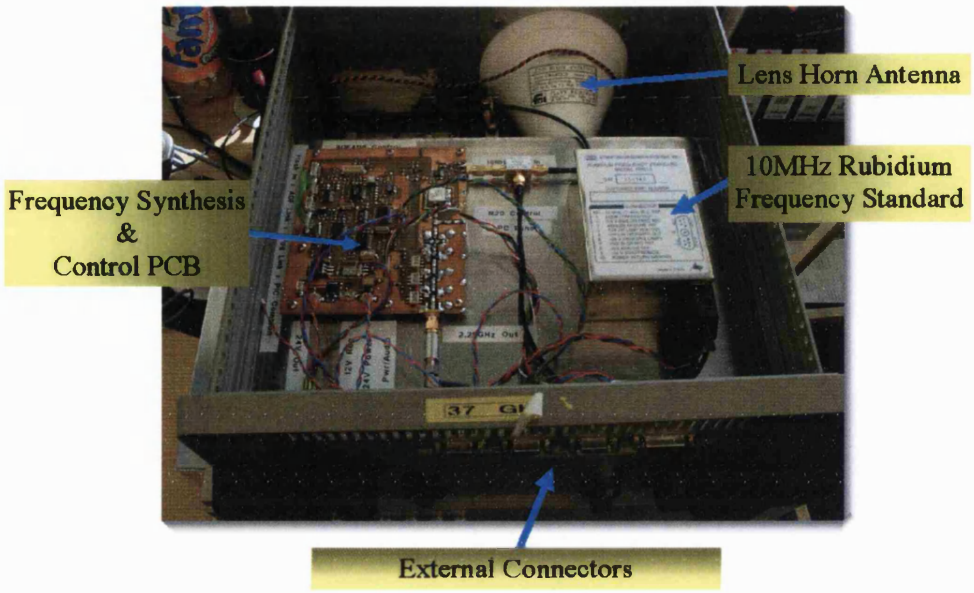

Figure 4.2: Transmitter viewed from the rear showing newly installed frequency generation hardware.

4.3.1 ADF4118 Frequency Synthesizer

To satisfy the requirement for a 2.28 GHz signal, a frequency synthesizer Integrated Circuit (IC) from Analogue Devices was selected. The IC, the ADF4118, operates in conjunction with a Voltage Controlled Oscillator VCO and a reference signal to synthesise a range of frequencies, programmed via a Personal Computer (PC) parallel port interface or direct connection to a microprocessor.

The design of the frequency synthesiser circuit was generated using free software available from the device manufacturer, Analogue Devices. The software enabled the parameters of a third party Voltage Controlled Oscillator (VCO) to be entered for use in the circuit design. The necessary programming parameters for the ADF4118 were calculated by the software along with the Phase Locked Loop (PLL) loop schematic.

The ADF4118 can operate from a range of reference frequencies however it was decided to use a standard 10 MHz reference. This frequency is suitable for both the PDRO and the ADF4118 and is readily available.

The ADF4118 requires the three internal counter parameters to be programmed at each power-up. During initial testing the PC based software was used to program the device but clearly in order for the equipment to operate remotely it would be necessary for this function to be performed within the transmitter itself, the most obvious solution being a microprocessor. This is an important requirement since the transmitter needs to have the ability to shut-down the Radio Frequency (RF) stages and reactivate them without requiring external physical intervention.

4.3.2 Rubidium Frequency Standard

The accuracy and drift of the frequency synthesiser is directly related to the reference since the ADF4118 uses counters to track the output frequency of the VCO. Without a stable reference the ADF4118 cannot accurately assess the output frequency and maintain close lock on the programmed target frequency.

A key feature of the design is the use of a single reference for both the 2.28 GHz synthesiser and the PDRO. This ensures that the two frequency components do not drift independently.

The remote location of the transmitter may be subject to temperature variations which would adversely affect the accuracy by affecting the reference. The result would be an output which varies in frequency as a function of temperature. To counteract this an ovenized oscillator was selected and is pictured in Figure 4.2. The PRS10 Rubidium Frequency Standard manufactured by Standford Research Systems is an ultra low noise frequency standard. It disciplines an SC-cut ovenized oscillator to a hyperfine transition in the ground state of rubidium [53]. The most important feature of the device is its ability to maintain the correct operating temperature for the oscillator while the case temperature varies between -20 and $+65\,°C$. This temperature range more than covers the anticipated field temperature range.

4.4 Transmitter Control

As previously established, some form of control is necessary for the transmitter since it will be operating remotely and since the ADF4118 is not capable of powering up into an operational state without assistance. The terms of the Office of Communications (OfCom) license also place a requirement upon the design. The transmitter must be turned off within 30 minutes of a request being issued to do so. Since the remote site is further than 30 minutes away by car and given that a request could be received at any time of the day or night, physically attending site to turn the transmitter off is not a practical solution. At the time of the design, it was not known what access to the transmitter there would be, particularly in terms of rapid, 24 hours per day access. With this uncertainty it was necessary for the transmitter to be controlled by a means which does not require physical intervention on site.

The obvious solution is a radio based remote control system. There are several possibilities on this front from license exempt short distance radio modules to separate high power radio links operating on a separate licensed frequency. All these solutions demand a reciprocal radio link and would require the control commands to be issued from a single or small number of locations. This is not ideal since it may not be possible to reach the control point to issue the control signals within the 30 minutes, especially during holidays or at the weekend.

The solution was found in a Global System for Mobile communication (GSM) communications module (pictured in Figure 4.6) which operates on the mobile network and permits both voice and data calls to be made and received. It also sends, receives and stores text messages. With an RS232 control port and external audio output connections, it is a very versatile communications module, ideally suited to this task. This solution enables the control commands to be issued from anywhere within the network coverage of the global mobile phone network, potentially from anywhere in the world with mobile phone coverage.

4.4.1 Siemens M20 GSM Module

The Siemens M20 is a fully functional mobile phone, minus the keypad, LCD display, speaker and microphone. It boasts some additional features for control, including an RS232 port and a power/audio port enabling external control and a headset port for voice call use.

The various features of the Siemens M20 GSM module were explored to determine those most suited to the task. It quickly became apparent that while the module boasts more than adequate text message handling features, the practicalities of using these features were prohibitively complex, mainly due to the format in which the messages were stored to the SIM card. The other major drawback of text messages for a control system is that they do not come with guaranteed delivery times, if the network is busy or experiencing difficulties, text messages get put to one side as a low priority service. Text message based control was therefore rejected as a practical solution to the problem due to uncertainty over the reliable delivery of a shutdown command.

The phone call capabilities of the M20 were of more direct use to this application, particularly as this is a switched circuit service. The next choice to be made was between data and voice calls. In data mode, the M20 is effectively a modem and operates as such using the RS232 port for all communications, both call control and data. This is obviously a highly efficient and effective means of communications with a remote computer/microprocessor based control system however it requires that both ends of the call are operated by computers. This places a requirement for terminal equipment at the control end of the call which is not always practical or convenient.

For practical purposes and to maintain the freedom afforded by the mobile network solution, the transmitter needs to be controlled by a human without the requirement for additional communications devices to perform translation. Voice calls were therefore selected, making use of Dual Tone Multi-Frequency (DTMF) codes to bridge the human/computer interface. Since all mobile phones are able to generate DTMF tones as are almost all land line telephones the human user would have all the signalling equipment

necessary by default.

The M20 module is also capable of generating DTMF codes but in common with mobile phones, it cannot understand them, consequently it was necessary to use an external DTMF decoder IC fed with the audio signal from the M20.

On a similar note, humans are not best equipped to decode DTMF codes either. Since this is the only form of audio communication the M20 can generate during a voice call, it is necessary for the vocabulary of the system to be kept to a minimum. This makes it possible for humans to decipher a few simple indications from the M20 such as 'OK', 'Error', 'On' and 'Off'. This is adequate for the basic control of the transmitter and does not require extra hardware for the generation of audio signals for transmission.

By forming simple patterns of DTMF codes it is possible to distinctly indicate these conditions. There is not that much scope within DTMF as each 'tone' is formed from pairs of frequencies arranged on a matrix basis yielding small groups of similar tones at slightly different pitches. While it is possible to decipher rising or falling tones and to count tones, identifying an individual tone is beyond what is reasonably possible. The indications were therefore formed by groups of tones in patterns arranged in a clear predetermined and predictable order.

4.4.2 PIC Microcontroller

In order to gel the separate elements of the design together into a robust functional system it was necessary to incorporate a microprocessor at the heart of the design. The microprocessor needs to monitor and control the M20 GSM module, read the decoded DTMF codes and act appropriately. It also needs to be able to switch the transmitter on and off and provide the ADF4118 with the target frequency settings.

There are a multitude of different microprocessors on the market, each boasting different capabilities. The design decision of which to use centred around the speed of reprogramming. Previous experience of Erasable Programmable Read Only Memory (EPROM) ICs and the associated 20 minute

erasure times, not to mention the difficulties of poor erasure during the design loop made this an unattractive option. The flash programming technique not only greatly simplifies the circuit design as program memory and the microprocessor are housed within a single package but makes programming and reprogramming almost instant. The PIC range of microprocessors offer not only fully integrated processors having on board program memory, Random Access Memory (RAM) and in some cases Electrically Erasable Programmable Read Only Memory (EEPROM) but also feature flash programming capability.

The selected processor, the PIC16F826, boasts EEPROM memory space which allows data to be stored and retained without any requirement for electrical power. The device also boasts a serial Universal Synchronous-Asynchronous Receiver/Transmitter (USART) for RS232 communications, a watchdog timer to generate automatic reset signals in the event of the processor (or software) entering an infinite loop and an external interrupt which the DTMF decoder IC can use to signal the arrival of a new code. Furthermore, the microprocessor can be programmed in circuit meaning a surface mount package could be used in the design.

During the design cycle, the microprocessor not only had to communicate with the M20 GSM module but also a PC running a terminal program since there was no other means of determining what the system was doing. With only one USART for RS232 communications, it was necessary to multiplex the RS232 Receive Data (RD) and Transmit Data (TD) lines thus allowing the microprocessor to selectively communicate with either the M20 or the PC.

4.4.3 PIC - GSM Interface

The interface between the PIC and the M20 module is crucial to the design. As already explained the M20 shares its communication lines with the PC in a multiplexed system controlled by the microprocessor. This has its relative benefits and draw backs. Firstly, the M20 operates in an environment which is inherently unpredictable and in adapting to this, can issue unsolicited mes-

sages. Clearly, whilst the PIC is communicating with the PC, anything the M20 announces will be missed. Similarly when the PIC begins communicating with the M20, the M20 may itself be attempting to communicate with the PIC.

The interfacing requirements were determined to begin to narrow down the likely scenarios and vocabulary necessary for successful control. The unsolicited messages from the M20 consist of a welcome message, issued after the M20 resets itself and a 'Ring' indication when an incoming voice or data call is detected. All other unsolicited messages, such as text message arrival, are to be ignored as they have no relevance to the core design requirements.

To address the potential issue of two devices attempting to transmit at the same time, resulting in garbled messages, the PIC treats any message which is incomplete or unrecognisable as a failed entry and after a time-out moves on. This prevents the PIC hanging after such an event. The mechanism also forces the USART buffer to be cleared which resets the overflow flag, another potential for system hang.

The design philosophy is based on both a certain level of predictability and the repetition of the most important messages. This allows the design to implement self-protecting features which sacrifice a guarantee of responding to everything in preference to remaining operational.

The start-up routine operates on the predictable. The M20 begins with a self check which terminates with a welcome message. The PIC's start-up routine is significantly shorter than that of the M20 and it therefore waits until the M20 has successfully completed its checks before continuing. This does represent one part of the design where the 'carry on regardless' philosophy was not adopted, simply because the system cannot do anything useful without the M20 functioning, thus there is no point in the PIC continuing to execute the program without the M20 being confirmed as functional.

Once the M20 has indicated its readiness, the M20 begins to search for a network, based on the Subscriber Information Module (SIM) card fitted. This search completes without confirmation so it is necessary for the PIC to poll the M20 for its network status. This is obviously a fairly intensive period during which the M20 is operating two communications channels si-

multaneously. The PIC will therefore continue even if the M20 fails to reply as expected or indeed at all to a status request.

The same network status request is the basis of the automatic shut-down feature of the system. If the GSM network signal level drops below a predetermined level for 25mins the PIC will turn the RF stage off since it is not possible to guarantee that a shut-down call would actually be received. Once the network link is re-established, the system makes a fresh start-up request from a human operator. This ensures compliance with the OfCom license without unnecessarily keeping the transmitter switched off.

Once the PIC has confirmed the network link, it makes a start-up request call, commanding the M20 to dial each of three pre-programmed numbers in turn, a maximum of three times each until a successful communication is achieved. Once this sequence is complete, the role of the PIC becomes one of periodic monitoring, checking approximately every 4.5mins that the network status is still above the threshold and monitoring the M20 interface for an incoming call indication. If none of the communication attempts succeed, the system ensures the transmitter is off and becomes passive, waiting for a human initiated call.

During a call, either incoming or outgoing, the PIC also maintains an active interrupt link with the DTMF decoder IC which has a direct audio link to the M20 via its power/audio port. This enables the PIC to control the call progress, commanding the M20 to issue DTMF tones and reading the decoded code output from the decoder IC received from the human end of the call.

4.4.4 PIC - PC Interface

The PIC must provide feedback in order for an effective debugging process to take place. The system, while designed to operate without a PC or other data logging device attached, none the less provides a commentary on the activity of the system. The level of detail is sufficient to determine where within the program memory, the PIC is currently executing.

The PIC briefly switches the Multiplexer (MUX) from M20 to PC in order

to issue an American Standard Code for Information Interchange (ASCII) string to the PC. The PIC does not accept commands from the PC simply because the system has to be reliably controlled from the mobile link. Problems with this form of communication need to be resolved rather than circumvented by direct serial communications. The PC link is therefore purely a diagnostic link.

4.4.5 PIC - ADF4118 Interface & Control

The PIC16F628 chosen for this design suffers a common problem with many microprocessors, a lack of port pins. For many reasons microprocessors have a limited number of port pins, these further often have more than one function. The PIC16F628 is no different and in order to implement an interface with the ADF4118 it was necessary to make this a second use for port pins already assigned to another function. The most obvious candidates for this are the programming port pins as these only operate as programming pins during the programming phase of the design cycle, they are otherwise unused.

These port pins were brought to a physical header allowing a wire harness to be constructed which allows the pins to be physically connected to either the programming circuitry or to the circuitry used by the PC parallel port interface. This solution leaves the ADF4118 programming circuitry intact and electrically isolated permitting use of the PC interface if required. It also ensures that the programming circuitry is disconnected during normal operation and does not therefore present any additional load to the pins which although not strictly a problem, is desirable.

The interface is made possible using the programming pins due to the face that despite the 9 pin interface between the PC and the ADF4118, only 3 lines are necessary for programming, the remainder allow the PC software to read board voltages etc. The 3 pins necessary for programming are data, clock and latch. The programming takes place asynchronously using the clock line to load each bit on the data line into a buffer. The latch line is then pulsed to store the contents of the buffer in the ADF4118 memory. The configuration word contains an identifying bit pattern determining which of

the three words it is, thus no address lines are required.

4.4.6 Circuit Description

The circuit schematic is divided into four sections, Power Supply & Control, PIC Microcontroller, ADF4118 Frequency Synthesiser and Analogue Devices Software Communications. The final PCB is shown in Figure 4.3 with the four sections and specific devices marked, Figure 4.4 shows the block diagram for this board.

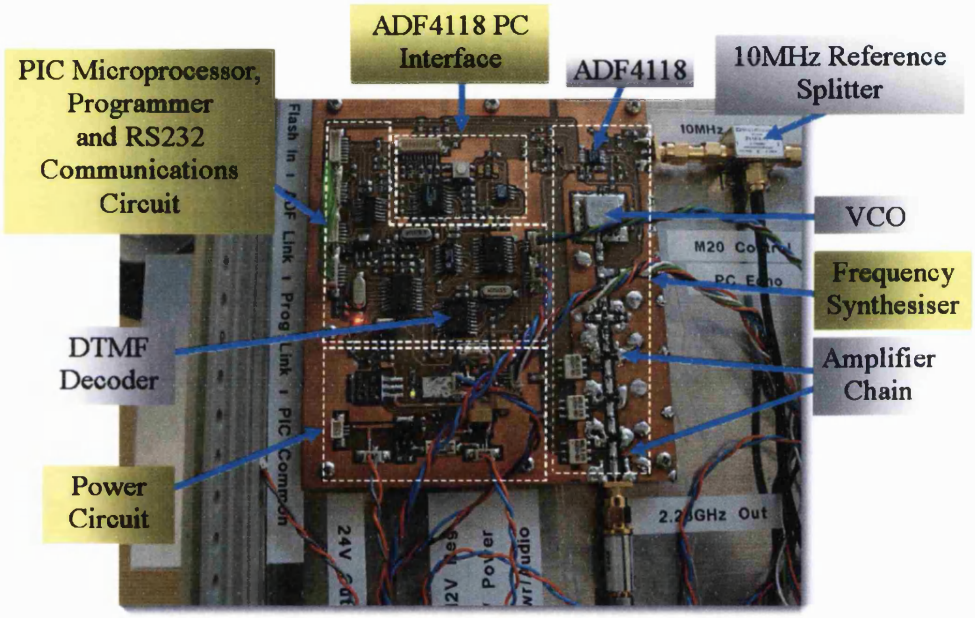

Figure 4.3: Transmitter frequency synthesiser PCB

4.4.6.1 Power Supply

The transmitter is supplied with 24 V DC which is fused on board within the power supply section. The two lower operating voltages are obtained from this supply using fixed voltage regulators. The logic circuitry operates on 5V while the M20 module and the PIC programming and RF amplification stages

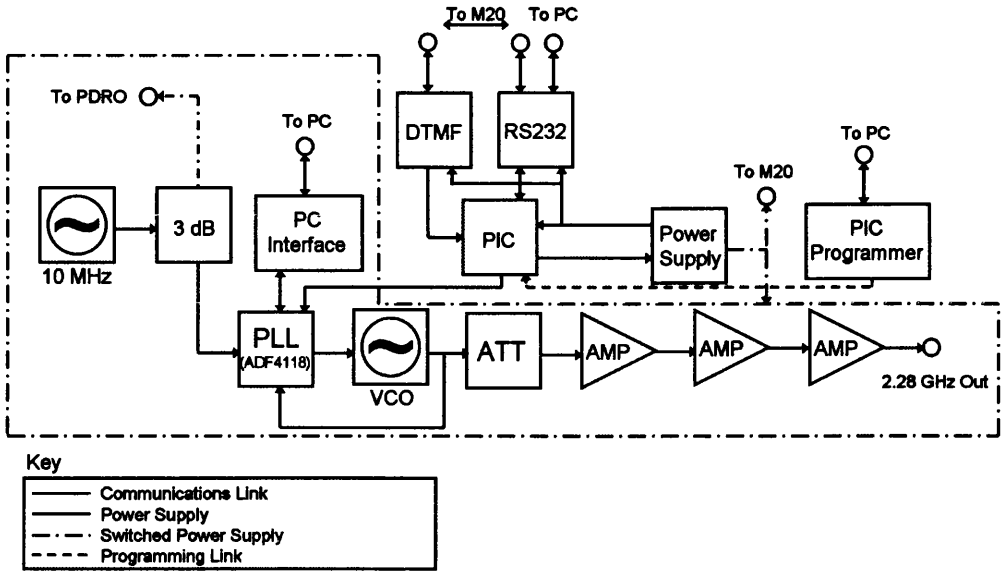

Figure 4.4: Frequency synthesiser block diagram

operate nominally on 12 V however to achieve the correct PIC programming voltage, the 12 V regulator ground potential is elevated with series diodes.

The 5 V and 24 V supplies are broken into two circuits, un-switched and switched. The two switched supplies power the parts of the circuit and transmitter which actively participate in radiating. Thus the ADF4118, VCO, Rubidium Reference, PDRO, Tripler and power amplifier are all connected to the switched supplies.

The single control signal for the Metal Oxide Semiconductor Field Effect Transistor (MOSFET) switching circuit comes from the PIC and drives two bipolar switching transistors which in turn drive the high current MOSFETs. It is necessary to drive the MOSFETs in this manner due to the voltage differential between the 24 V rail and the low state of the PIC port pin, the MOSFET Drain to Gate voltage limit would otherwise be exceeded resulting in failure of the device.

4.4.6.2 PIC Microprocessor

The PIC Micro section contains the communications elements of the circuit. The audio signal from the M20 is obtained from the same port as the M20

power supply. The signal is filtered and presented to the MT8870DS DTMF decoder IC. This IC has five connections to the PIC, four data lines and an interrupt line.

4.4.6.3 Analogue Devices Software Communications

The ADF4118 circuit has been designed to include some of the functionality of the evaluation board designed by Analog Devices. The circuit uses an A/D converter to measure the voltage levels present on the two supply lines of the ADF4118 which are connected via a small value resistor. This allows the software to determine the current currently being drawn by the device in addition to the voltages. This is not of any direct benefit to the design however it does allow the evaluation software to operate as intended.

Two of the three programming lines for the ADF4118 are isolated from this circuit, making direct connection with the PC interface. The exception is the data line which is used for programming the ADF4118 and reading the A/D value back via the PC interface. While the software is communicating with the A/D converter, the Chip Select (CS) line of the A/D is held low permitting it to use the data line. This pin floats when the board is not connected to a PC which together with the absence of a serial clock signal from the PC prevents the A/D circuit interfering with serial communications to the ADF4118.

4.4.6.4 ADF4118 Frequency Synthesiser

The Frequency Synthesis circuit is the most critical in terms of layout design on this board. While the Analog Devices software designed the loop filter and basic circuit structure based on the VCO specifications, the actual track design and RF amplification design was not and had to be designed separately.

The 10 MHz reference is terminated by a 50 Ω load before being received by the ADF4118. The ADF4118 produces a pulsed error output signal which is filtered by a loop filter before driving the VCO. The VCO output is split using a 'T' network, one of the spurs being terminated with a 50 Ω load. This

spur is used to provide feedback to the ADF4118 forming the Phase Locked Loop (PLL). The other spur is attenuated by what is in effect another 'T' network however the parallel resistor is split into two to make the structure symmetric. The use of an attenuation pad and coupling capacitors ensures that the VCO is not loaded by impedance mismatches further down the amplification chain. The design used is in accordance with the design note advice given for the Z-Comm VCO employed in the design.

Three stages of amplification then follow to raise the signal to a suitable level. The monolithic amplifiers are biased from the boosted 12 V supply via wide band RF chokes. The amplification along the chain is too large to prevent hard limiting unless the signal from the VCO is attenuated. The attenuation pad used to isolate the VCO from the amplifier chain has resistor values which reduce the signal level sufficiently to prevent this occurring.

The output power at approximately +12 dBm is too high for the mixer in the transmitter so attenuators are used to reduce the signal power so the safe limit of +7 dBm is not exceeded.

The ADF4118 provides a programmable output which can be used to indicate that it is in lock. This output has a very low drive capability so a Darlington arrangement is required in order that an Light Emitting Diode (LED) indicator can be used. This lock indicator doubles as an indicator that the transmitter is switched on since lock is achieved rapidly after power up and frequency programming and is maintained thereafter until power down.

The circuit layout is crucial to the performance of the design, particularly the RF section. The width for all tracks on the RF side of the VCO is 2.6 mm. This is the width which corresponds to a 50 Ω impedance on the FR4 copper clad board used for the Printed Circuit Board (PCB).

$$Z_0 = \frac{120\pi}{\sqrt{\epsilon_r + 1.41}} \ln\left[\frac{5.98q}{0.8w + t_h}\right] \tag{4.1}$$

For the FR4 board used in the design; ϵ_r = 5.4, q (board thickness) = 1.6 mm = 0.0016 m, t_h (track thickness) = 35 microns = 35x10^{-6} m and Z_0 = 50 Ω. w, the track width is the calculated result from Equation 4.1 [54] and is 0.0026255 m = 2.6 mm.

At high frequencies, it is not just the track width that is important, the earthing becomes critical too. The design of the board is such that the underside of the board is a single copper plane, connected to ground on the upper surface by vias. These vias are concentrated around the 2.28 GHz track and associated components. The ground plane on the upper surface is broken into two sections which while electrically connected, provides a separation between the high frequency and the digital portions of the board.

The issue of correct grounding became apparent during testing when the amplifier chain failed to achieve the anticipated output power and began to overheat. Following investigation, additional vias were inserted at the edge of the board to prevent the run off of the board acting as a capacitor. Further vias close to the ground pins of the amplifiers were also required to prevent the amplifiers resonating.

4.5 Remote Control Software Overview

Once the transmitter combined frequency synthesis and remote control board was constructed, it was necessary to write the control software. The basic requirement for the software was to accept an incoming call with a request for a shut-down and perform the required task. This is the only function the board must perform. It is however both relatively easy and desirable to extend the range of functions to include transmitter start-up and other functions to provide more control over the transmitter.

Initial plans included several features which were eventually not necessary, useful or simply too time consuming to implement reliably. The software is consequently fairly unsophisticated in the sense that it operates in a linear manner, reacting only to the expected chain of events and simply deals with unexpected situations by ignoring them.

The operation of the software can be summarized as follows. The program begins by confirming code execution to the PC and then waits for a few seconds. This delay allows the M20 to perform its own start-up routine. This concludes with the issuing of a welcome message of 'OK'. The M20 then begins a search for base stations. The control program then makes a request

to the M20 for its status. The program allows for communication failures during this process and will not proceed should the M20 fail to successfully link to a network and report a satisfactory status.

The program continues by determining the previous state of the transmitter from the PIC EEPROM (on/off) before beginning a calling cycle. The intention being that following a power failure, the transmitter will make contact and report its previous status to the human recipient of the call. Based on this information the transmitter can be instructed to remain off or to resume transmission. The default for the transmitter is off regardless of the previous state and only a successful command will cause the transmitter to switch on.

The dialling sequence uses three preprogrammed numbers in turn with each number being tried three times consecutively. Each attempt is limited to 30 seconds which prevents the call being diverted to voice mail if the call reaches a mobile but does not get answered. By the same token a call diverted to answer phone due to the target mobile not being available will be terminated to cap call costs.

It has been foreseen that it is not always desirable for the transmitter to contact certain numbers. A simple flag system is therefore used to switch the numbers on and off again via the remote link. This allows a number to be temporally disabled e.g. while someone is on holiday etc.

Irrespective of the outcome of the attempts to contact a human, the program enters the main loop which waits for incoming calls. This loop breaks once every 4 minutes or so to check the signal strength of the M20 link. This break also provides an opportunity, if the transmitter is switched on, to send the configuration sequences to the ADF4118. This is necessary because during a brief interruption in the power supply, the ADF4118 loses its settings before the PIC registers the power failure. In this situation the transmitter would be operating without the 2.28 GHz signal and would therefore transmit at 34.29 GHz.

The program checks the M20 signal quality every 4 minutes and either resets or decrements a counter based on the result. If the quality falls below 10 (corresponding to -93 dBm) then the counter is decremented. If the counter

reaches zero, then the transmitter is powered down and the program loops until a satisfactory level of signal is restored. The reason for this approach is to ensure that the maximum time the transmitter can operate without a remote link is less than the period in which the license requires the equipment to be turned off.

Once the program has established that the link signal strength has returned to an acceptable level, the dialling process is initiated as the transmitter cannot be restarted without a command to do so. A similar procedure is followed to that used following power failure, if the dialling sequence fails to yield a command the program becomes passive, waiting for an incoming call with the transmitter still switched off.

4.5.1 Call Structure

The structure of the calls both incoming and outgoing are important as they rely on DTMF tones for all communication. The procedure therefore relies on a small number of distinctive tone combinations, pauses and a consistent structure to produce a usable interface.

Outgoing call:

The outgoing call is designed to only determine the desired state of the transmitter power. No other options are accepted and simply result in the process starting again. The call lasts until either completed successfully or until three attempts have failed. The user has only a few seconds to make entries otherwise the program considers the entry a failure and continues. This avoids calls lasting too long and therefore costing too much. This is especially important for the outgoing calls as they drain the credit from the SIM card in the M20 and although this can be replenished via the internet it is not desirable to have credit wasted.

Incoming call:

The incoming call differs only in two respects, firstly that the status of the transmitter is not stated at the beginning of the call and second that an additional option is available. The additional option is that of controlling the flags for the three numbers dialled after a power failure or mobile signal

Table 4.1: Call Structure

Step	Notes
Call answered	2 second pause allows recipient to place handset to ear
Open call	Three tones rising in pitch
3 second pause	
Previous transmitter status	1 tone for off, 2 for on
User logon	6 digit sequence
Acknowledge or reject logon	2 tone acceptance, single tone rejection
	Failure - back to beginning
Accept user command	two digit sequence
Accept user option	single digit
Implement option	
Confirm command acceptance	Two tone acceptance or repeat from beginning
Pause for 2 seconds	
End call	Three tones of decreasing pitch
Terminate connection	

loss. The user can opt to confirm the current status of the flags or to modify them. In either case, the status of each of the three numbers is stated either as on or off by two tones either rising or falling in tone respectively. If modifying the flags, after each number the user has the option to set or clear the flag by pressing 1 for on and 0 for off. The settings are then repeated for confirmation before the call is terminated.

In order to communicate with both the PC interface and the M20, the program needs to store commands as data. There are a number of different methods for achieving the storage and more importantly, the retrieval of data from the PIC memory. The choice of where to store such data is obviously limited to EEPROM and ROM. The location of primary choice is ROM as the retrieval of the data is both faster and less complex. The method employed is the table read method. This involves the program counter being set to a location corresponding to the beginning of a data list. The instruction at this location uses a pre-stored offset to affect a jump to a data byte within the

table. Program flow then returns to where the table read was called with the data byte in the accumulator. Repetitive calls with an incrementing offset allow data to be sequentially read.

The limitations of the program memory however do mean that verbose messages and commands are not possible if a sizeable program is also to reside within the ROM, as in this case. The messages therefore have been kept short and where possible repetition has been avoided. So for example two messages which include the same word will be constructed using separate concatenated table calls to collect the necessary data.

The EEPROM data is used by the program to store information which is variable but which is useful to have preserved during a power failure. The data which falls into this category is the power status of the transmitter. This could potentially be used to ensure the transmitter recovered from a power cut in the same state as it was before the power loss as it would minimise down time. The problem is that there would be no distinction between a short outage and a long one, thus the equipment may have been moved and not properly shut-down. If the transmitter simply begins transmission as soon as it plugged in it could potentially be operating in close proximity to people, in a laboratory for example. For this reason, despite having the previous transmission status, the transmitter always requires an explicit command to begin transmission.

All other variables are only of short term consequence and are initialized either at the beginning of the program or immediately before use. This ensures that at power up all variables are in a known state and are unaffected by previous events.

4.5.2 Transmitter Housing and Deployment

The transmitter housing as previously stated was not waterproof. In addition the transmitter relies on a number of external components to operate, none of which are waterproof either. It was therefore necessary to find a housing into which all the equipment could be housed.

The solution chosen was a large fibreglass cabinet. This has locks which

are outside the waterproof seal which ensures that the seal integrity is not affected. To allow the transmitter to radiate, a window was cut in one end of the cabinet and covered and sealed using radome material. This material is the same material used to seal the lens horn antennas themselves. This ensures that it appears transparent to the signal yet allows a good tough seal to be made over the aperture. The cabinet and the radome window can be seen in Figure 4.5.

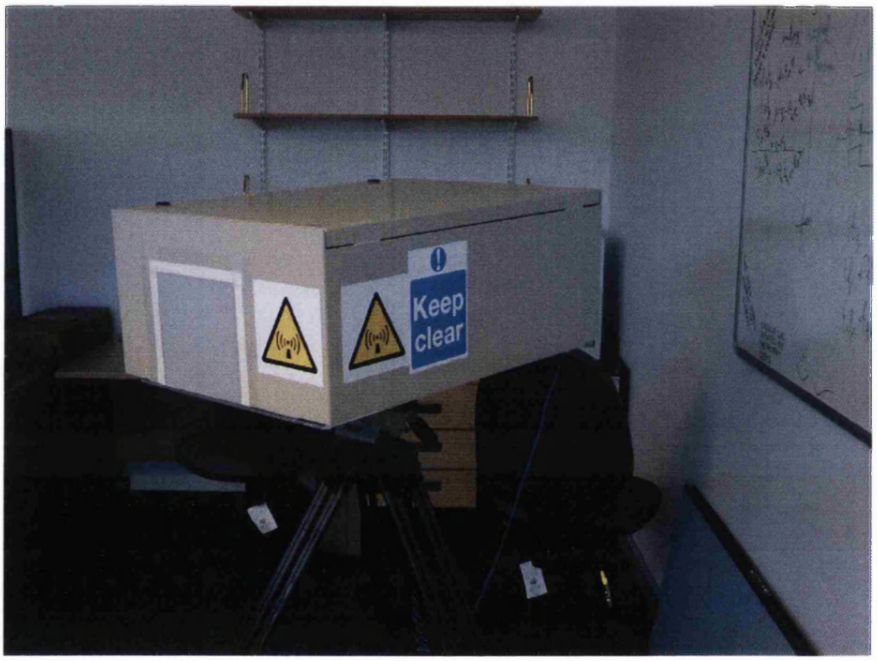

Figure 4.5: Transmitter waterproof cabinet on tripod mounting base plate

In addition to sealing a rectangular piece of the radome material over the circular hole ensuring significant overlap, the edges were taped down with strong, waterproof tape specially designed for such applications. It has reinforcing threads in a criss-cross pattern for strength and is backed with a very strong adhesive.

This approach to the transmitter housing was preferable to directly mounting the lens horn antenna, which is waterproof, to the cabinet because it keeps the transmitter separate. This allows the transmitter to be

operated independently of the larger cabinet, allows the transmitter to be repositioned within the cabinet for fine alignment and required no modification of the waveguides within the transmitter.

The transmitter cabinet needed to have two additional holes for mains and GSM antenna connections. These were made with waterproof connectors. The power supply, housed in a small instrument case, fitted with a cooling fan and the GSM module could then be located within the cabinet, directly behind the transmitter as seen in Figure 4.6.

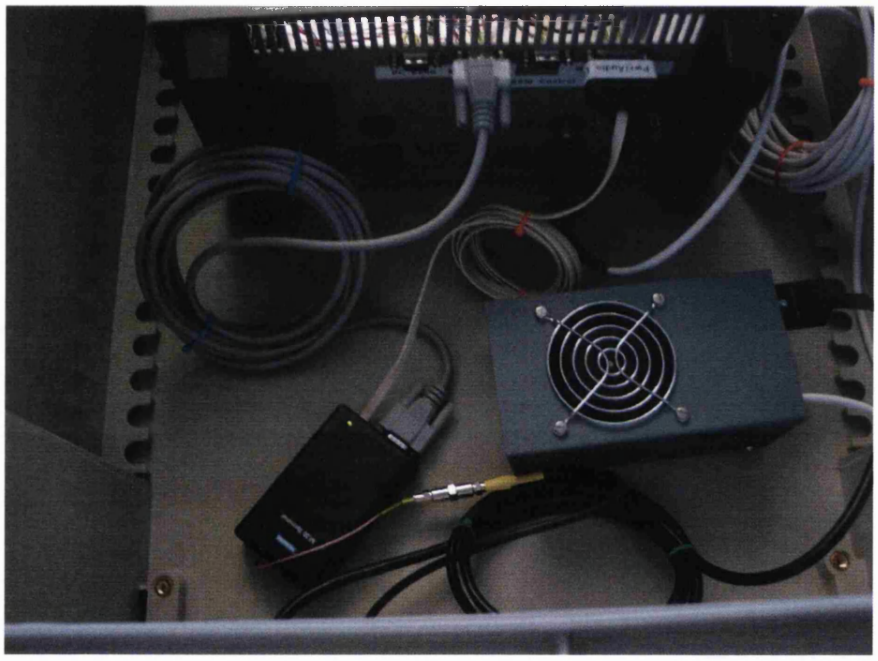

Figure 4.6: Power supply and GSM module housed in transmitter cabinet behind transmitter

The two fans (transmitter amplifier and power supply) circulate the air within the cabinet to ensure good heat transfer from those components which generate heat and it also ensures that the two silica-gel moisture absorbers are exposed to the air allowing moisture to be absorbed efficiently. This helps combat condensation. To further protect the new frequency synthesiser and control PCB the lid of the original housing was positioned to protect from moisture dripping from the centre of the cabinet lid. The original housing

Figure 4.7: Transmitter on site with power supply, GSM module and silica-gel absorbers

lid no longer fits due to the increased height of the strip lines connections of the new amplifier.

The GSM antenna is fitted with a magnetic base allowing it to remain firmly attached to a miniature equipment case fitted with spikes to anchor it into the ground on the reservoir mound a short distance from the transmitter cabinet.

Summary

This chapter has reviewed the Transmitter design and discussed the work carried out to prepare it for deployment on the experimental link. Chapter 5 now examines the receiver array which forms the other end of the link.

Chapter 5

Design and Implementation of Propagation Experiment - Receive Array

5.1 Receiver Overview

The receive array consists of five receive head units and one Demodulation Unit (DU). The receive heads each contain a lens horn antenna, a MMIC down converter, an IF amplifier and a MMIC protection PCB as can be seen in Figure 5.9.

The DU contains a power distribution board with over voltage protection circuitry which generates all the necessary voltages for itself and the receive heads from a single $\pm 24\,V$ DC supply. The DU is also responsible for providing five LO outputs for the MMIC down converters at 17.43 GHz and a further five internal LO signals at 1570 MHz for the second down conversion stage which takes place in the DU. Figure 5.1 shows the design of the DU in block diagram form. The oscillators are derived from a pair of ovenized crystals.

The 140 MHz IF resulting from the second down conversion is filtered, amplified and demodulated within the DU using the middle receive head signal as a reference. The four resulting I/Q pairs are amplified and output using line drivers.

The receive array was received toward the start of the project and clearly

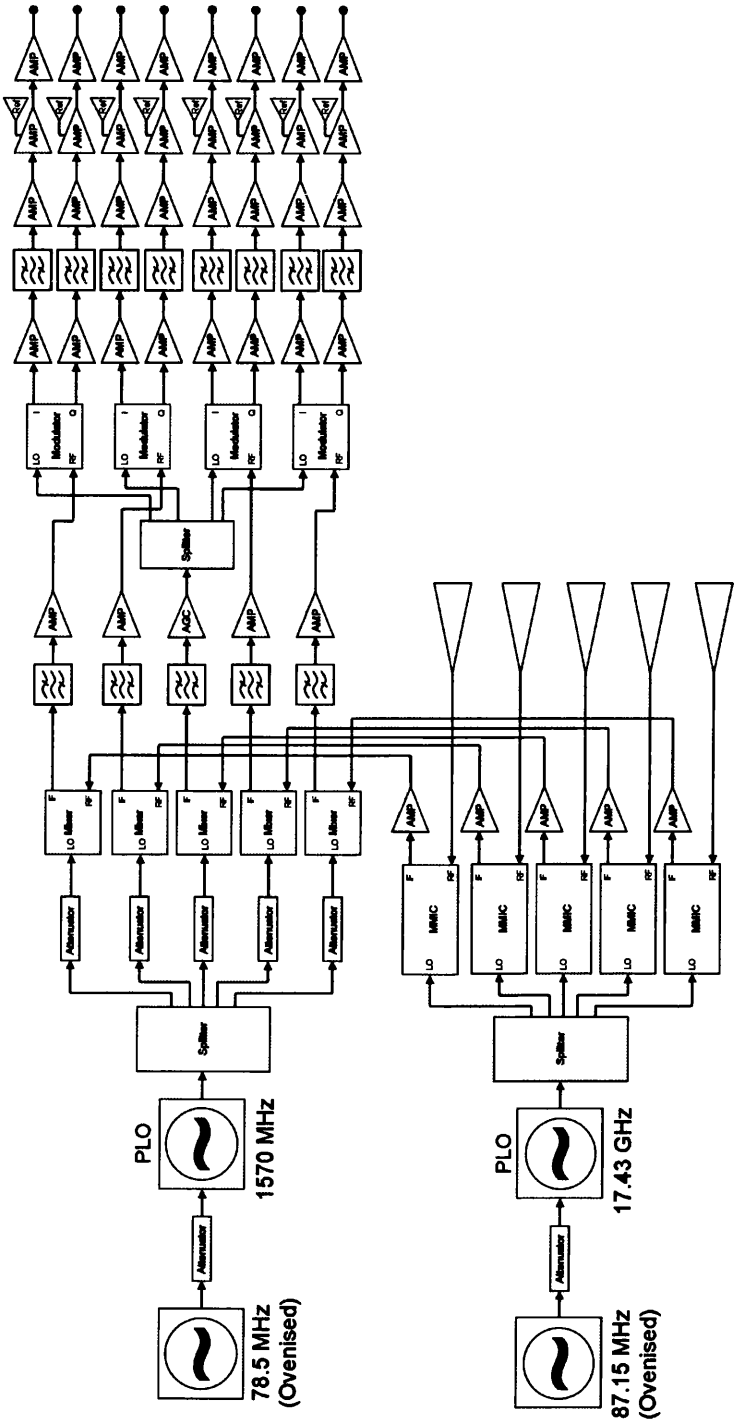

Figure 5.1: Demodulation unit block diagram

demonstrated some problems. The construction of the DU is a two layer design with all the components, except front panel mounted controls, mounted on aluminium base plates. These plates showed evidence of water ingress. Of more concern however were the two power distribution boards, one of which showed signs of serious over heating, was dramatically bowed due to poor support for its size and indeed was not mounted using all of the available mounting points.

The whole receive array was constructed with no insulation and the design relied heavily on variable voltage regulators. This last observation caused concern since it had been made clear that the MMICs were particularly sensitive to voltage irregularities and were not economically replaceable should they become damaged. The potential for electrical faults to occur within the design was considered high, particularly as loose mounting hardware was present in proximity to uninsulated electrical connections.

The array was therefore deemed unsuitable for deployment and was dismantled and rebuilt, incorporating modifications to protect the MMICs and other components.

5.1.1 Mechanical Rebuild

As previously noted the DU required remedial work to ensure successful operation over a long period of time. Part of this process involved rebuilding the unit having cleaned, insulated and sealed the case.

The unit consists of two aluminium base plates which are mounted above each other. To these all the RF components are fixed, connected together by lengths of hard line. The layout was noted and these plates were stripped of all components. This allowed the water staining and other damage to be removed by skimming the aluminium. The plates were then lightly oiled, drilled to accept the new distribution board and repopulated with components.

All the front panel devices (switches, LEDs and connectors) were removed, their terminals insulated and then resealed into place with silicon sealant to prevent water ingress from the front of the case.

The cabinet locks were resealed as were unused hinge points to prevent water ingress during operation. The difficulty being the orientation of the cabinet, the design expects the door to be vertical not horizontal. Using the cabinet in a horizontal orientation allows standing water to form around the seals, increasing the likelihood of ingress.

A similar water proofing procedure was necessary for each of the five receive heads which are also orientated horizontally. This was complicated by the fact that the base of each unit is punctured by four mounting holes which proved hard to seal effectively.

5.2 Demodulation Unit - Power Distribution

First on the priority list was the replacement of the power distribution board. In hindsight the single distribution point design for the array isn't the best however the existing design philosophy was adopted and a single power board was designed.

The original design used variable voltage regulators to provide design flexibility, allowing the output voltages to be adjusted if required. It had been anticipated that the MMICs might require a slight increase in supply voltage due to the fact that the devices were made as a short production run of a custom design. Since, when tested it was discovered that no such adjustment had been made to the original supply it was concluded that there was no necessity to use variable voltage regulators. Introducing a resistor into the ground path of the fixed regulators was left as a design option however to ensure the option of adjustment was retained. The opportunity was therefore taken to replace the variable regulators with fixed ones which have the benefit of not allowing the output potential to rise to the input potential in the event of an open circuit in the control circuit.

5.2.1 Supply Protection

To further protect the MMICs and indeed the whole unit, it was decided that over voltage protection circuitry should be incorporated into the design. This

was deemed important since the laboratory bench power supply unit which was to be used as a power source for the array has easily adjusted outputs and is capable of supplying potentials in excess of the maximum ratings of the fixed voltage regulators. This type of power source is also open to the potential for cross/reverse connection, particularly given the bipolar nature of the supply requirements.

To mitigate these potential power supply issues, a diode and fuse based protection circuit was incorporated which ensures that the three power connections are correctly ordered and powered. The use of fuses allows the rating of the diodes to be reduced since they would only conduct briefly before fuse failure. This is then followed by a MOSFET switched over-voltage protection circuit which uses the zener avalanche effect to trip a MOSFET with a low on state resistance. This gives the circuit the necessary switching capability to handle the high supply currents while introducing minimal resistance on the supply rails.

The original key operated Double Pole Single Throw (DPST) switch was replaced with two illuminated push buttons which allow the two supply rails to be switched independently since it was determined that the key switch was allowing switch bounce causing false trips in the protection circuits. This change also allowed the status of the main protection circuits to be visible from the front panel which is particularly useful during power up.

5.2.2 Regulation

The new board features fixed voltage regulators for all the supplies including the $\pm 15\,\mathrm{V}$ supplies which were originally unregulated being taken directly from the main supply rails. This clearly required the supply to be correctly adjusted to prevent damage to the large number of expensive components connected to one or both 15 V circuits.

The introduction of these 15 V regulators does make it necessary to supply a higher voltage to the DU to ensure the regulator drop-out is adequately compensated for.

Each regulator has an output indication LED which allows easy confir-

mation of the functioning of each supply. The original design used two +6 V regulators to supply the +6 V required by the five MMICs however due to the length of cable between the DU and the receiver heads and the high current demand, there was a significant voltage drop. This was initially mitigated by inserting diodes and resistors into the ground path of the regulators however this did not provide satisfactory results in increasing the output voltage. It was also noted that the regulators were becoming excessively hot, generating quantities of heat which were not easily removed from the chassis plate. It was decided to replace the fixed regulators with a high current switched regulator which dissipates considerably less heat under the same load conditions. This regulator was built on a separate PCB (see Figure 5.2) allowing the regulator to be directly fixed to the chassis plate for heat sinking purposes.

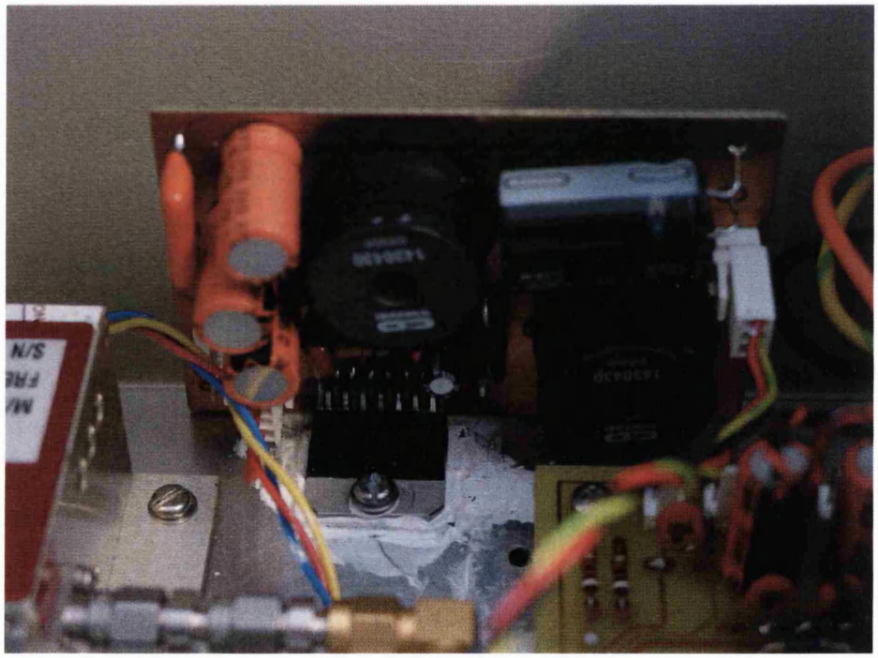

Figure 5.2: Switched 6V regulator board, mounted with IC in contact with the lower aluminium plate for heat sinking

This has the drawback that the regulator is a variable output device which relies on feedback to maintain the output however its construction on a custom built PCB and the use of fixed resistors was deemed to be reasonable

mitigation of the risk.

The issue of heat dissipation was a problem encountered early on in the testing and as a result of the on board heat sinks being insufficient to dissipate the heat being generated, all the regulators were removed from the PCB, connectorised and mounted directly on the chassis under and around the PCB.

It was necessary to remove some of the more heavily loaded regulators and place them on a forced-air cooled heat sink fitted with four 12 V PC processor fans, see Figure 5.3. This was necessary because heat was not being transferred from the aluminium chassis plate to the steel cabinet as expected, heat therefore built-up within the unit reducing heat transfer and resulting in the chassis plate reaching excessive temperatures.

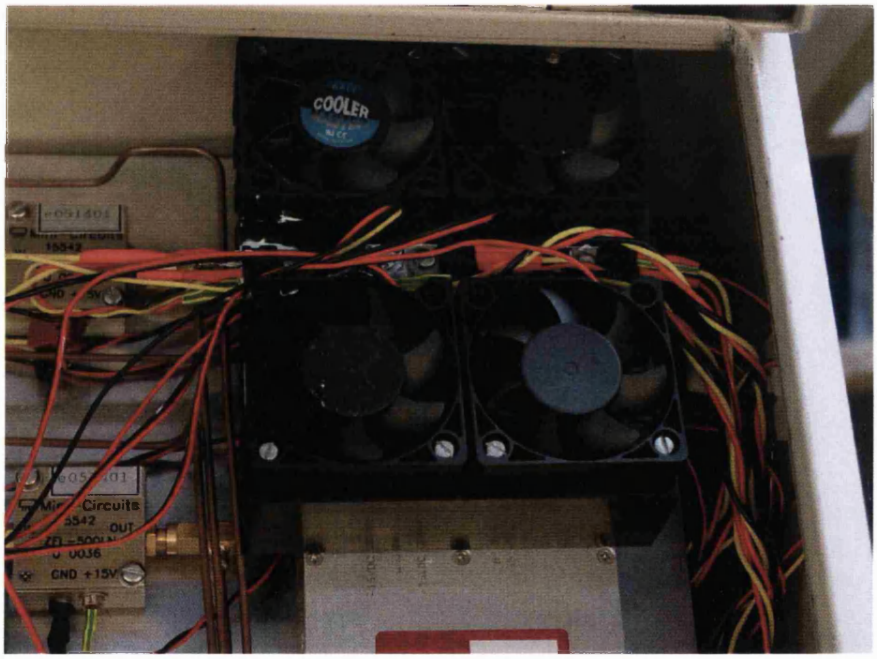

Figure 5.3: Heat sink fitted with voltage regulators and four cooling fans

In order to complete the cooling, the end inspection cover was fitted with a large case fan and a vent (Figure 5.4), protected by a folded aluminium hood (Figure 5.5) to cycle air through the cabinet. The fan speed is controlled by

a thermistor located near a hot spot at the opposite end of the cabinet. This allows heat to be removed from the case rather than allowing it to simply build up. It was noted that the ovenized crystal oscillators were having difficulty maintaining their operational temperature due to the effectiveness of the cooling fan. A shield was therefore fitted to protect the oscillators from the direct air flow.

5.2.3 Output Control & Protection

To protect the MMICs further, another set of over-voltage protection circuits were placed on the output of the ±6 V regulators. Whilst these were originally there to provide protection against the catastrophic failure of a regulator or a direct short circuit, these circuits also provide protection against feedback failure within the switched regulator circuit fitted to the +6 V supply.

These circuits were also fitted with a degree of flexibility to allow them to trip at a higher voltage if it was necessary to increase the 6 V rails. By introducing a resistor in series with the zener diode, a potential divider is created. This can be used to elevate the effective trip voltage of the circuit.

These circuits were deemed to be a crucial addition to the design, providing protection against a multitude of fault conditions which cause the voltage rails to exceed a threshold. The aim was obviously to protect the devices most at risk and least easily replaced.

Once again MOSFETs with low on state resistance are used providing a rapid switching capability, which is highly desirable under fault conditions, without adversely affecting the supply during normal operation.

5.2.4 Board Layout

In common with the electrical design, the physical layout of the new power supply board followed the original. There is a logical flow along the front panel controls from the power connector, main switch and warning indicators to the power output sockets. Figure 5.6 shows the block diagram for the power board. The positioning of the output connectors along the front edge

Figure 5.4: Fan and vent fitted to end plate of demodulation unit cabinet

Figure 5.5: Hood fitted over fan and vent to protect them from water ingress

of the board was also dictated by this layout. The new design does address the issue of connectorisation, the original failed to completely conectorise the board meaning that while most connections could be simply disconnected, the front panel warning LED signals were hard wired to the ovenized crystal oscillators and PLLs. This prevented the board from easily being removed from the DU.

Since the new board replaces the two original boards, there are a significant number of connections which need to be made to the top level within the DU. Figure 5.7 shows the new board in position on the lower plate. All these connections are made along the edge of the board which runs parallel to the end of the plate. This makes it possible to reach the connectors with both plates in-situ but the top plate loosened on its mountings. This solution also keeps the cable runs short.

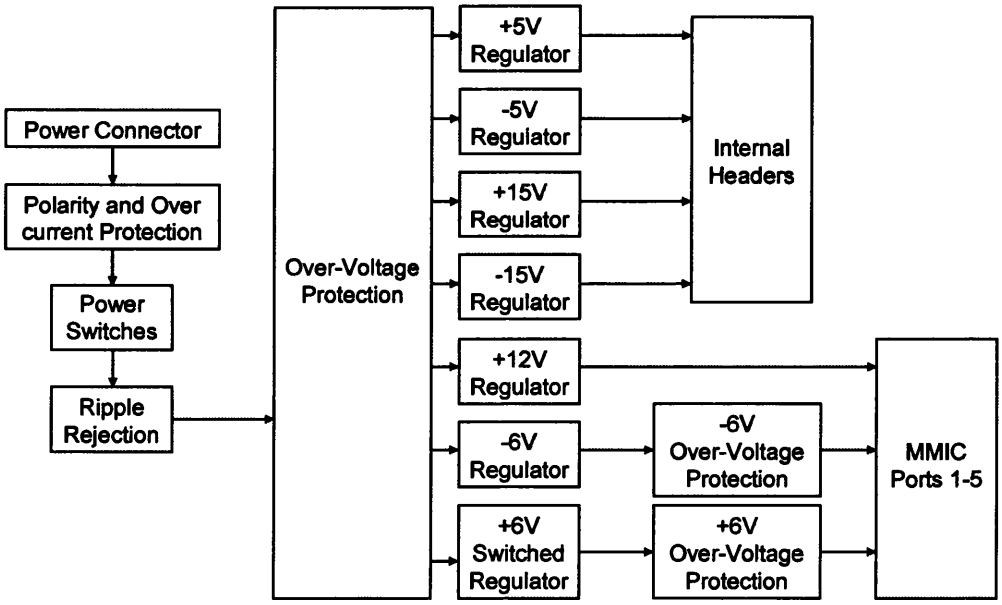

Figure 5.6: Block diagram for demodulation unit power board

5.2.5 Testing

Clearly the circuit had to be tested to ensure it was capable of supplying the various and high current loads demanded by the equipment.

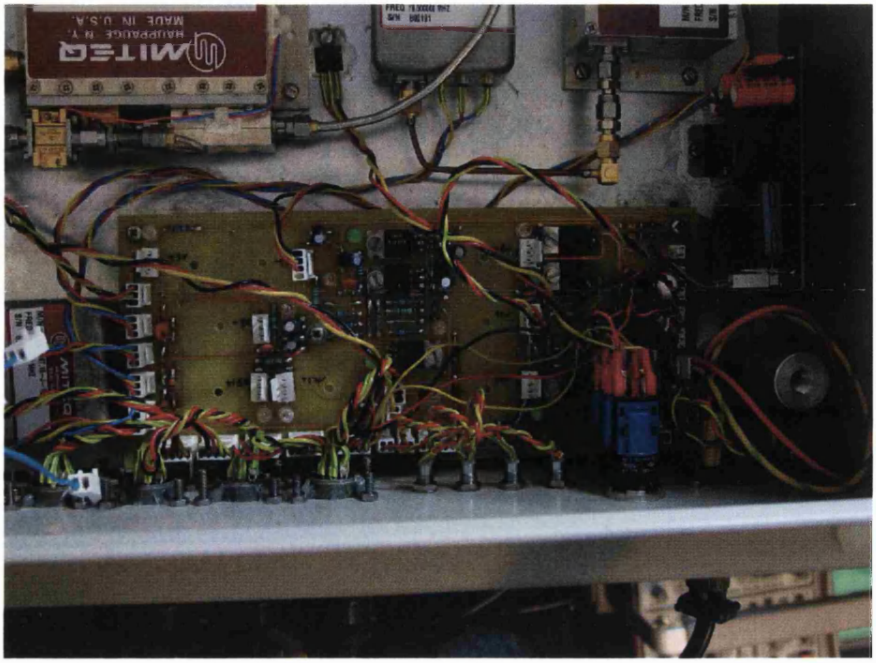

Figure 5.7: New combined power supply PCB

Testing was undertaken with wire wound variable resistors set to appropriate loads. During many tests the current drawn by the load exceeded the maximum anticipated in use. This was due to the difficulty of accurately setting the resistors to the correct values and the fact that the resistance often varied over time due to heating or unreliable wiper contacts. The tests showed that the circuit performed correctly and was not adversely affected by the higher loads.

5.3 Demodulation Unit - Demodulation Board Testing & Calibration

5.3.1 Hard Line Testing

During the mechanical rebuild of the two plates, each piece of semi-rigid coaxial cable (hard line) was tested across the frequency band at which it

operates to ensure linearity. Several lengths exhibited non-linearities and were reworked to rectify the problem. All such lengths passed a subsequent test.

5.3.2 Demodulation Board Testing

In order to test the operation of the demodulation board it was necessary to build a variable phase shifter. This allowed a variable phase shift to be introduced between the reference channel and any one of the other four channels in turn. The phase difference could be manually swept or automatically swept by an arbitrary signal generator.

Using this phase shifter, it was possible to adjust the phase shift continuously and capture the output of the demodulation circuit using the A/D converter card in the data logging PC, plotting the result almost in real time. By doing so, it was possible to see in a graphical form, what effect the adjustments were having on the output.

Achieving similar phase shifts with the head units would have been possible however it would not have been possible to continuously vary the shift in the manner possible with the variable phase shifter. Safety and technical considerations would also require serious consideration for such operation of the equipment. Not only would the radiation pose a risk to people working close by but it would also expose the receivers to higher signal levels than they were designed to accept. For the lab based tests, the phase shifter option was therefore selected.

The demodulation circuits use an I/Q modulator operated in reverse. The modulator is fed with the signal from its corresponding head unit and the split reference signal from the middle array element. The two resulting signals are then amplified, filtered by switched capacitor filters and amplified once again. The resulting signals are still too weak to be passed along long lengths of cable so line driver IC's buffer them to coaxial cables connecting the demodulation unit and the PC A/D interface.

5.3.2.1 Phase Shifter Design

The phase shifter design uses a splitter to create two signal paths. One path is phase shifted with respect to the other by two Mini Circuits JSPHS-150 variable phase shifters. As a consequence the phase shifted signal is attenuated. To rebalance the output signal magnitudes, the pass-through path contains a π network attenuator, providing attenuation of approximately 2.4 dB.

Each of the phase shifters provides up to at least 180° of phase shift by means of a DC control signal. As a result a phase shift of more than 360° was possible using this circuit. This was important because it allows the full range of the demodulation circuit to be tested within a single sweep.

The phase shifter circuit was originally designed to be manually adjustable however the surface mount resistors used in the design were insufficiently robust for continuous adjustment. While larger wired connected replacements proved more reliable, for ease and accuracy of adjustment these were replaced with a swept output signal generated by an arbitrary signal generator.

5.3.2.2 MATLAB Software

To accompany the phase shifter, a sample Matrix Laboratory (MATLAB) program, supplied by the manufacturer of the A/D PC card was modified. The modifications allow the program to collect data from the card and plot the position given by the I and Q signals from one of the four channels. A circle is first drawn on the plot by the program for reference during adjustment of the gain settings on the demodulation board.

The A/D card continuously collects data and stores it in RAM until MATLAB collects it. The measurements do not therefore depend on the speed of the program however there is a noticeable lag on the plot. The program strikes a balance between constantly collecting small quantities of data from the card before redrawing the plot on screen and collecting data in larger chunks less frequently.

The program uses a MATLAB library dedicated to the A/D card for all the communications, control, configuration and data transfer. The program

collects 500 words of data from the card before updating the plot. This process is repeated 50 times before additional calculations are performed on the collected data. The plot is then cleared and the process repeats a number of times. These nested loops allow the program to run for a considerable period of time, periodically clearing the display and summarizing the data. The advantage is that no user intervention is required during the adjustment process.

5.3.2.3 Results of Testing

One of the main purposes of performing the tests on this board was to ensure the effect of the adjustments was known and understood so once in the field, adjustments could be made with confidence.

The tests involved adjusting the gains and offsets of the two stages of amplification while the phase difference was swept through more than 360°. The reference circle being the target.

It soon became clear that the adjustments for one channel were not having the desired effects and while it was possible to match the reference circle at certain points, the data mapped out a ellipse, skewed with respect to the axes.

Having ruled out hard limiting as a potential cause of this problem and having confirmed similar problems will other channels, the circuit was examined in detail.

Several tests were carried out but only when the switched capacitor filters were removed from circuit did the problem disappear. Having identified the component which was causing the observed effect, a breadboard test circuit was built to check the function of the device.

By applying a frequency swept signal to the filter it was possible to observe its frequency response across its operating range. The response indicated that the component had failed and required replacing. Similar tests were performed on the other seven components identifying other faulty ICs.

Replacements were obtained and tested in a similar manner. These devices produced results which differed from both the faulty components and

those previously deemed functional. As a result further replacements were ordered.

Once a full set of replacements was ready they were fitted one at a time after being tested in the breadboard circuit to verify functionality. Before all the components could be installed it became apparent that those devices already inserted were overheating, something not observed during the breadboard tests. When removed from the circuit and retested on the breadboard these devices exhibited the same failure signatures as the original components.

It transpired that the demodulation board had been fitted with a modification, not shown on the documentation, which created a short circuit causing the ICs to fail rapidly. As a consequence of this modification all the original devices and the replacements already inserted had been destroyed.

The modifications were removed from all eight channels and further replacement parts obtained, tested and successfully fitted.

Once this problem was eradicated, it became easy to adjust the circuit to match the reference circle. As a result confidence can be had that the board can be successfully adjusted in the field.

5.4 Data Logging Software

The receive end of the link needs to record data. The data is in the form of four I/Q pairs from the four receive channels relative to the central one. The signals are connected to the PC via an A/D data acquisition card. This card differs from others in that the samples are truly simultaneous and data is buffered on the card until the PC can accept it and store it on the hard drive. The sampling is therefore not affected directly by the load placed upon the PC which allows operations on the PC to be non-time critical meaning that recovering data from the PC can take place without affecting the continuing data collection process.

There is software supplied with the card which allows data to be captured to a text file however this method only allows data to be recorded in a single file. To specify another file requires a break in sampling and manual

intervention to specify the new file name.

The ideal means of logging data is to perform a continuous collection process but to periodically divert the flow of data into files with logical, sequentially ordered names. This situation is not catered for in the software however the card does have tools and example files which enable it to be easily controlled by various programming languages and mathematical environments.

The tools which allow Matlab to collect data from the card have already been used in a basic program for the calibration of the demodulation board. For long term data collection Matlab was not a favoured option, instead C was chosen as the language in which to write a simple program capable of collecting data from the card, creating the files and storing the data in them. The program is based on an example program which simply logged data to a file. The function of the example code was identical to the stand alone data logging program supplied with the board.

The functionality of the code has been altered to trigger data collection and then collect data from the card memory and write it to an open file. After each block of data has been written the computer clock is checked to determine the day. When the day rolls over, i.e. at midnight, the currently open file is closed and another is opened. The name of the file includes the time and date it was created making it easy to arrange files and be certain about in which order they should be.

To account for noise in the system, the program instructs the data acquisition card to sample at 102400 samples per second. With eight active channels, the card appends 819200 samples to the buffer every second. The program collects the data in blocks of 8192 samples and adds them to eight counters. Each counter holding the sum of 1024 samples for a single channel. The counters are divided by 1024 to yield the average and these results are stored in the data file. One hundred such averages are thus obtained for each channel every second.

The program also ensures that data is not split between nor lost during the creation of log files. It achieves this by flagging a day boundary but only starting a new log file once all the data for the current second is processed.

Collecting data in blocks of a known length ensures accurate file transitions.

The noise in the receiver originates from the phase noise in the local oscillators. The two main types of noise are thermal/shot noise and supply/substrate noise. The former can be determined for an oscillator and sets a lower limit on the achievable system noise performance. While both amplitude and phase are affected by noise, the amplitude noise is less of a problem due to automatic gain controls. In the study of phase differences, clearly noise introduced on the phase is a much more serious problem and some means to mitigate its effects is required.

Over the sampling period of 0.01 s it can be assumed that the signal being measured remains unchanged, thus it may be considered to be the DC component of the signal with noise superimposed upon it. The effect of averaging a number of measured samples is to reduce the noise whilst preserving the DC signal component. The reduction in noise varies as the square root of the reciprocal of the number of averaged samples. So to improve the Signal to Noise Ratio (SNR) for a given sampling rate, it is necessary to increase the real sampling rate and average back to down. In this case, the noise is reduced by a factor of 0.03 by the averaging performed at the card.

Similarly, performing another average over the 100 samples recorded each second yields a further noise reduction by a factor of 0.1 and overall the averaging reduces the noise by a factor of 0.003. Again, this is valid because the measured signal is expected to vary over longer time periods and can therefore be considered to be the DC signal component which is unaffected by averaging.

The costs of averaging at higher sample rates to achieve such noise reductions are two fold. Firstly there is the practical issue of sampling at higher rates and the costs of A/D cards capable of performing the sampling and secondly, there is the issue of the card having to either record the data to be averaged later or perform the averaging in real time. In this design the data acquisition card was capable of performing both the desired sampling rate and the averaging in real time. The level of over-sampling and averaging used in this case was primarily justified as a mitigation technique for not

having the anticipated margin on the link budget.

5.5 Receive Units

The receive units (as seen in Figure 5.9) consist of a lens horn antenna, a Gallium Arsenide (GaAs) MMIC and an IF amplifier as detailed in block diagram form in Figure 5.8. These elements are housed in a notionally water-proof box which can be mounted, by means of a base plate, to the framework in a number of positions.

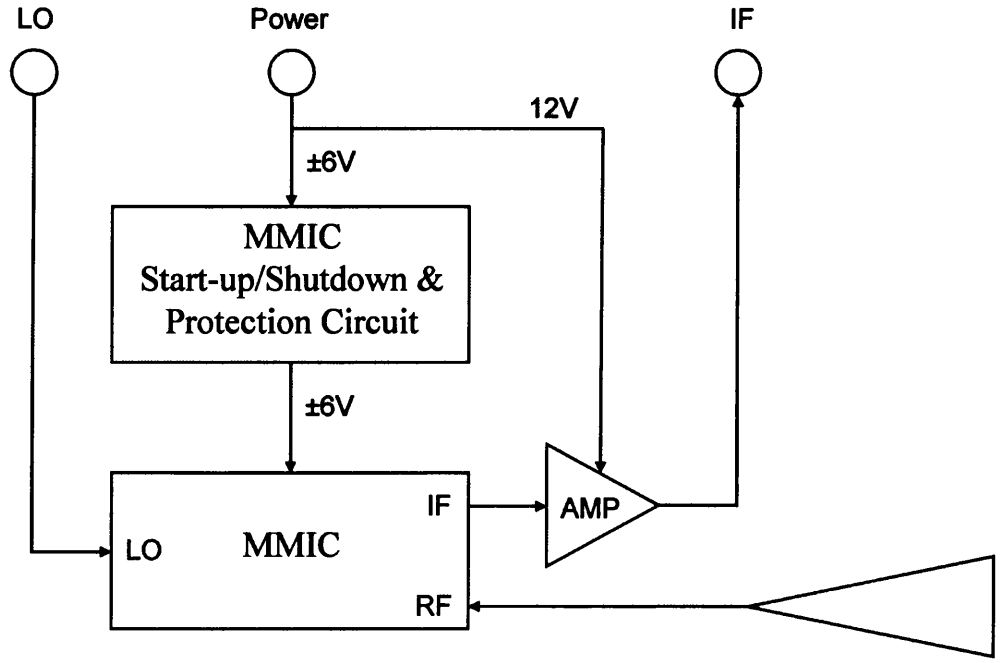

Figure 5.8: Block diagram of receive head unit

Each unit has a power socket for the ±6 V and +12 V supplies along with SubMiniature version A (SMA) connections for the 17.43 GHz LO frequency and output IF of 1.71 GHz.

The transmitted signal 36.57 GHz is received using the narrow beam lens horn antenna which achieves a gain of 34 dB. The lens horn antenna directly feeds into the MMIC where the signal is passed through a Low Noise Amplifier (LNA). The MMIC is also directly fed by the LO frequency of

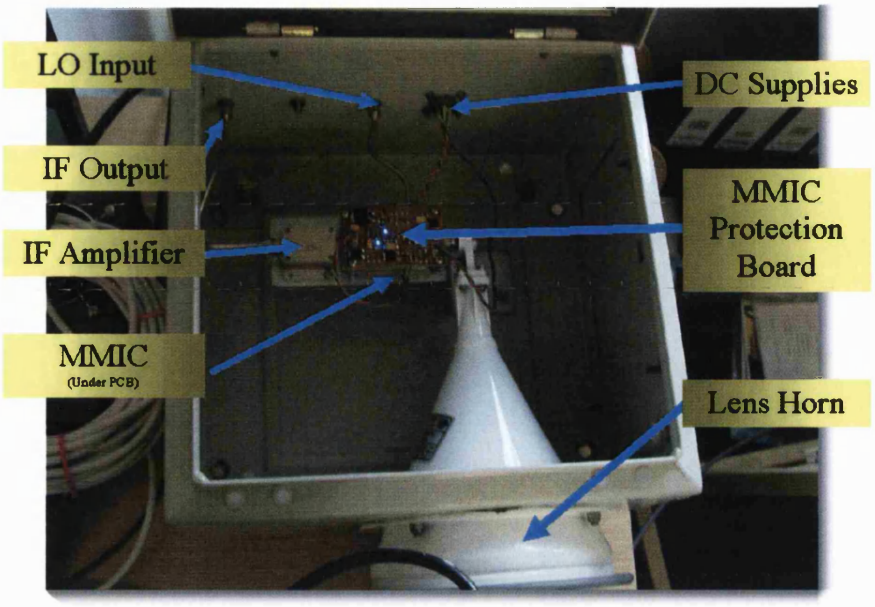

Figure 5.9: Receive head unit

17.43 GHz. The MMIC doubles and buffers the LO before mixing it with the amplified received signal which has also been filtered. The resulting IF signal is amplified within the MMIC before being amplified once more by a stand alone amplifier.

The block diagram of Figure 5.10 shows the internal design of the MMIC devices indicating that there in fact two MMIC wafers and a power supply board.

The MMICs are able to operate over a range of frequencies, the RF range is 34-40 GHz, the LO range is 16-19 GHz.

5.5.1 Monolithic Microwave IC (MMIC) Protection Board

The single most import component of the receive units and indeed the receive array as a whole are the MMIC ICs. These five devices are unique, there are no direct replacements available and the expense incurred in the production of further similar devices would be prohibitive.

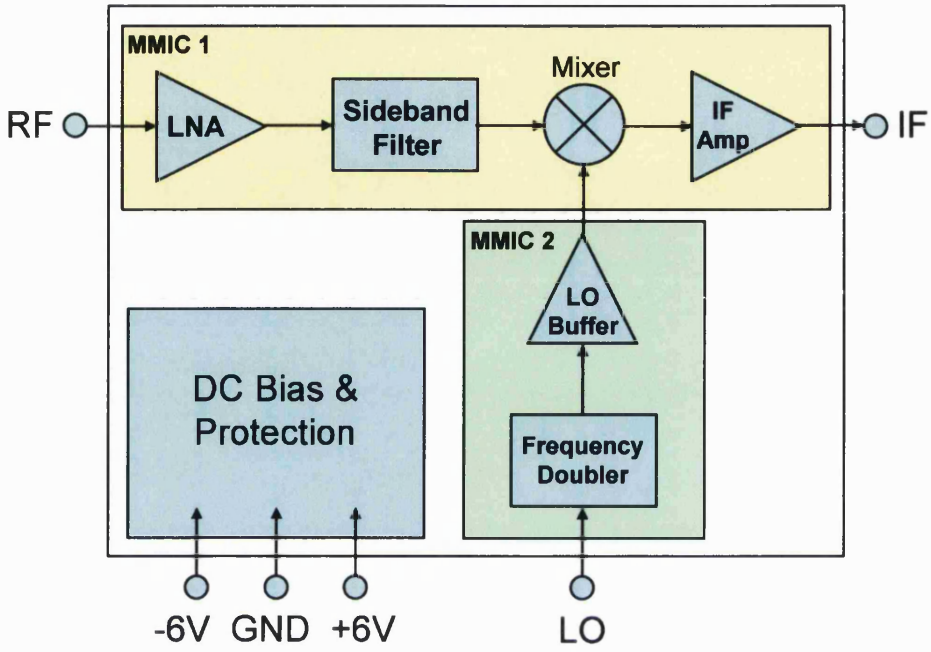

Figure 5.10: Functional diagram of the MMICs used

Unfortunately these devices do not have any accompanying data sheets and consequently the only information available comes from the printed label on the case and Mark Evans' thesis [38].

The lack of detailed information for the MMICs and in particular on their absolute maximum rating means that it is not possible to determine whether the devices are vulnerable to damage if the negative rail is present without the positive. It is possible that the devices already incorporate protective circuitry to ensure conditions likely to damage the GaAs MMIC wafers cannot occur, but equally they may not. Unprotected GaAs Field Effect Transistor (FET)s and MMICs are extremely sensitive to drain and gate voltages and currents as well as the order in which they are applied or removed [55].

With the significant level of uncertainty on this matter and the clear reliance of the project on these devices it was deemed prudent to spend time designing circuitry to protect the MMICs from damage. It was also noted that the over voltage protection circuits designed and incorporated into the

power distribution board made it more likely that one supply rail would be present and one absent. It would therefore be possible for the MMICs to be protected from a potentially damaging over voltage condition but exposed to an equally destructive absent rail condition.

5.5.1.1 Circuit Requirements

The primary requirement for the MMIC protection boards is that the MMICs should only be powered up if both supply rails are present and close to their nominal voltages. When the MMICs are powered up, the negative rail must be present before the positive rail is connected. Similarly during shut-down, either normal or under a fault condition (e.g. missing supply rail) the positive supply rail must be removed first.

It was also noted that the demand the MMICs place on the rails is significantly different, the positive supply current is considerably greater than the negative. The requirements stated thus far would allow for a supply rail failure however losing the ground connection would cause the ground connection of the MMIC to float exposing it to another potentially damaging condition. The final requirement was therefore that the MMIC be shut-down in the event of no ground connection being present.

The circuit design can be broken into three functional blocks, ground sensing, missing rail detection and start-up/shut-down control.

5.5.1.2 Ground Sensing

The function of ground current sensing is undertaken by a UA741 op-amp in a voltage to current configuration. The amplifier senses the ground current as it passes through a $0.33\,\Omega$ resistor placed in series with the ground path. When voltage is present across this resistor, i.e. when current is flowing to ground, the Op-Amp turns on one of two transistors wired in series forming a logical 'AND' function.

Clearly this circuit depends on current flowing through the sense resistor to ground to detect the presence of the ground connection. There would be a significant current flow during MMIC operation however the MMIC

cannot be powered up until the Op-Amp senses the ground current and thus confirms the presence of a ground connection. Consequently a trickle current is necessary to permit the op-amp to confirm the ground connection integrity. A 1 kΩ resistor connected to the positive rail and a 0.1μF capacitor connected to the op-amp output, both connected to the sense resistor provide a detectable trickle current and overcome any start up hysteresis in the Op-Amp circuit.

5.5.1.3 Missing Rail Detection

The next section of the circuit is dedicated to ensuring that both rails are present and close to their nominal values. If both rails are present and there is a ground path back to the demodulation unit (as previously discussed), then the rails are connected to the final stage of the circuit.

The controlling element of the circuit is a 9.1 V zener diode which conducts when the voltage between the two supply rails exceeds approximately 10V due to the potential divider formed by the zener and a 10 kΩ resistor. When the zener diode conducts it turns on the second transistor forming the wired 'AND' function with the ground sense transistor. Together these two transistors complete a circuit between the positive and negative rails. The current in this circuit is used to drive a transistor in a Darlington arrangement which in turn switch MOSFETs which perform the supply rail switching. The MOSFETs used in this design are the surface mount versions of those used in the power distribution board design.

Indicator LEDs are connected to the rails after the MOSFETs to indicate the presence of power to the final stage of the circuit. This is the only visual indication the receive head is powered.

5.5.1.4 Start-up/Shut-down Control

The final stage of the circuit is responsible for ensuring the negative supply is present before the positive supply is connected to the MMIC during start-up and that it remains until the positive supply is removed during shut-down.

The circuit design is based heavily on the circuit presented in EDN Europe

magazine [55]. Once again the properties of a zener diode are exploited. D4, a 3.3 V zener diode conducts when the negative rail reaches approximately 4 V due to the gate-emitter voltage drop of Q6. This breakdown conducts charge from the gate of MOSFET Q2 connecting the positive supply rail to the MMIC.

This portion of the circuit ensures that the positive rail cannot be present if the negative rail isn't. This however is only of use for start-up. During a shut down the circuit has to maintain the negative supply until the positive has been successfully removed.

This is achieved by inserting two large capacitors between the rails and ground. Since the MMIC draws a larger current from the positive rail and given that the same capacitor value is used, the positive capacitor will discharge first.

To ensure that the negative pin of the MMIC is not pulled high by the supply rail an isolating Schottky diode is present. The diode exhibits a rapid response time and a low forward voltage drop.

One final level of protection for the MMICs is provided by this portion of the circuit. Two 6.8 V zener diodes clamp the output of the board to ensure over voltage transients are suppressed.

5.5.1.5 Testing

Before the protection boards were used with the MMICs, they needed to be tested under a range of conditions to ensure that under all normal and anticipated fault conditions, they correctly handled the shut-down/start-up sequence.

The initial tests, conducted on breadboard prototype, revealed some issues. Firstly it became apparent that there was a delicate balance to be struck on the sense resistor selection. The higher the value of the resistor, the easier it is to detect the voltage drop across it but the harder it becomes to ignore the effect on ground elevation. The compromise of 0.33 Ω provides sufficient voltage for the Op-Amp to detect with minimal ground elevation. The reduction in the positive rail can be corrected by adjustment in the 6 V

regulator circuit and the marginal increase in the negative voltage was tolerable as it was believed that running the MMICs slightly above the 6 V stated would not present a problem.

The initial tests also indicated that while the Op-Amp was capable of detecting the ground current, the detection at start-up was somewhat unreliable. The introduction of a capacitor to briefly hold the output of the Op-Amp low at start-up, forcing the ground sense input to the 'AND' transistor arrangement to be logical '1' resolved the issue.

The introduction of a 1 kΩ resistor to provide a trickle current through the sense resistor was also necessary to permit the Op-Amp to to sense the ground connection while the MMIC is off (low voltage rail condition etc). This modification solved an issue with the circuit not restarting after the circuit shut-down the outputs due to a missing rail condition.

After construction, the five protection boards were tested again to ensure correct performance. These tests soon revealed an instability in the negative switching circuit. The MOSFET appeared to bounce during shut-down. Initially the circuit responded as anticipated however as the capacitors discharged, the MOSFET began to conduct before once more switching off. This problem was solved by applying a modification to the board in the form of a 0.1μF capacitor in parallel with the pull down resistor fitted to the MOSFET.

Once these issued were resolved, the circuits were tested to check that each performed correctly under both normal operating and fault conditions. The tests undertaken were;

- Positive Rail Connected & Disconnected with Negative Rail Present
- Negative Rail Connected & Disconnected with Positive Rail Present
- Positive Rail Over-Voltage Shut-down & Restart with Negative Rail Present
- Negative Rail Over-Voltage Shut-down & Restart with Positive Rail Present

- Key Switch Power-up and Shut-down
- Ground Disconnected, both Rails Present

In each case, the outputs were monitored on a digital storage oscilloscope using edge triggering. In each instance the outputs were correctly sequenced.

5.5.1.6 Mechanical Installation

The MMIC and amplifier in each receive head are mounted on an aluminium bracket bolted to the base of the cabinet. This supports the components at the level of the connector on the lens horn antenna. The brackets were however designed to support these two components with no usable free space. The advantage of having these components mounted at this height within the cabinet is that their location is approximately in the middle in all directions and thus they are not likely to be directly affected by water ingress. Ideally the protection board would be positioned close to the MMICs and in a similarly protected location within the cabinet.

The option selected was to mount the boards on pillars above the MMICs as the brackets were constructed to support the amplifier which is wider than the MMIC package. This solution meant that not only could the boards be positioned close to the MMICs but also that the indicator LEDs were easily viewed from the cabinet opening. This is important as it permits easy confirmation of operation of the units which may be only accessible from a ladder once deployed on the receiver array framework.

5.5.2 Weather Proofing

Despite the bracket design used to hold components clear of any water within the receive cabinets, it is highly desirable to ensure water ingress does not occur. All five units showed signs that water had entered the cabinets in the past. Each unit was therefore completely dismantled and rebuilt with each part being sealed back into place with silicon sealant. This included the removal of the lens horn antennas and for the three units which form the horizontal array, the bolts which attach their mounting plates. Each of

the locking mechanisms were dismantled and made waterproof using water repellent grease.

Once rebuilt, the cabinets were subjected to a vigorous hosing which left all five boxes containing differing quantities of water. While some of the water had entered through mounting holes which could not be sealed until the units were installed, other leaks were obviously the result of poor seals around the lids of the cabinets. The seals on the lids appeared to be failing around the front edges. To remedy this, the locking levers were removed and flattened. This makes it necessary for the lids to be pressed closed while the lock is turned. The seal is made by a smooth lip on the cabinet pressing against a rubber gasket, by increasing the pressure between the lip and the gasket, the seal is more effective.

Following this modification, the boxes were again subjected to water, this time succeeding in preventing water ingress. While it is still possible for water to penetrate under harsh conditions, such as a heavy rain storm after a hot sunny period when the pressure within the cabinet will fall rapidly creating a vacuum, the quantity should not present a problem to the operation of the equipment.

5.6 Equipment Difficulties

5.6.1 MMIC Failure

A number of difficulties were experienced during the preparation, deployment and operation of the equipment. This section attempts to explain the more serious difficulties encountered and the measures taken to overcome them.

The most serious problem encountered was the failure of one of the five MMIC devices. The failure was hard to detect because the device initially performed extremely well. There was a spread of performance among the devices from very good to poor. The device in question developed a habit of shutting down randomly and drawing excessive current. Once identified as faulty it was observed that the fault condition could present itself at start up or at any point thereafter, on one test approximately 45 minutes later. The

fault condition duration similarly could last for periods of less than a second through to indefinite periods. Removing and reapplying power was not an effective remedy.

The fault was detected after a significant number of over heating and voltage irregularity issues had come to light. The temperatures being reached by the voltage regulators within the DU had caused concern and attempts to correct the problem initially appeared to work however the issue often resurfaced on subsequent tests. Additionally maintaining the MMIC voltage supplies close to $\pm 6\,\mathrm{V}$ had been proving difficult. All of the issues encountered can be explained by the excessive current being demanded by the faulty MMIC and the irregular and random nature of the fault.

The MMIC was returned to the foundry where it was made at Qinetiq and following the longest period of fault-free operation since the discovery of the problem, it was confirmed to be indeed faulty. Despite the discovery that mechanical shocks to the LO port could trigger and clear the fault condition, the fault was deemed to be a flaw in the wafer or bias circuit. The fault appears to be very similar to the fault which two of the MMICs had during the previous period of operation, detailed in [38].

The array of five elements thus became four as the faulty MMIC, having been returned to Qinetiq for repair, was lost to the experiment due to the prohibitive cost of such a repair. The experiment therefore continued with four receivers, yielding three I/Q pairs.

During the subsequent operation of the array, a further MMIC developed a worryingly similar fault. This device had been selected as being the strongest and best performing device and was therefore used as the reference receiver. During periods of faulty operation, the receiver was operating without a reference and thus the collected data is meaningless. Fortunately the device often failed to start for up to half a day after switch on but following a few further short drop outs, operated continuously.

5.6.2 Amplifiers

The transmitter was supplied with an amplifier fitted (seen in Figure 4.2, immediately to the left of the lens horn antenna) which it was claimed was operational but of a lower gain in comparison to the spare amplifier. This spare amplifier had apparently been fitted to the transmitter when an input exceeding the +7 dB had been applied. The amplifier failed due to excessive input power. The amplifier was sent for repair but upon its return was not refitted.

The implication was that the transmitter could be operated as was, planning the link for the gain available form the existing amplifier. If it were to be discovered that there was insufficient output power, the amplifier could be replaced by the original, repaired, one to boost the output.

Early on the repaired amplifier was tested to determine its gain. It became immediately apparent that the amplifier was not functional and was unusable.

Later it became apparent that the amplifier fitted to the transmitter was also not functional and was in fact operating as an attenuator.

It was therefore necessary to purchase a new amplifier and fit it together with a substantial heat sink into the space previously occupied by the original amplifier which was glued to a bracket, which was in turn glued to the front panel of the transmitter housing. The new amplifier can be seen attached to its fan cooled heat sink in Figure 5.11.

This new arrangement also required a fan to ensure heat was effectively transferred from the heat sink to the air circulating within the waterproof outdoor housing.

5.6.3 Cables

Another cause of difficulties came when the power cables used to distribute power between the DU and the receive head units shorted. The cause of the short appeared to be an unidentified substance present on the inside of the connector which had become conductive due to water ingress through the perished rubber seals. The fault did not cause any damage since the zener diodes fitted to the outputs of the MMIC protection boards conducted,

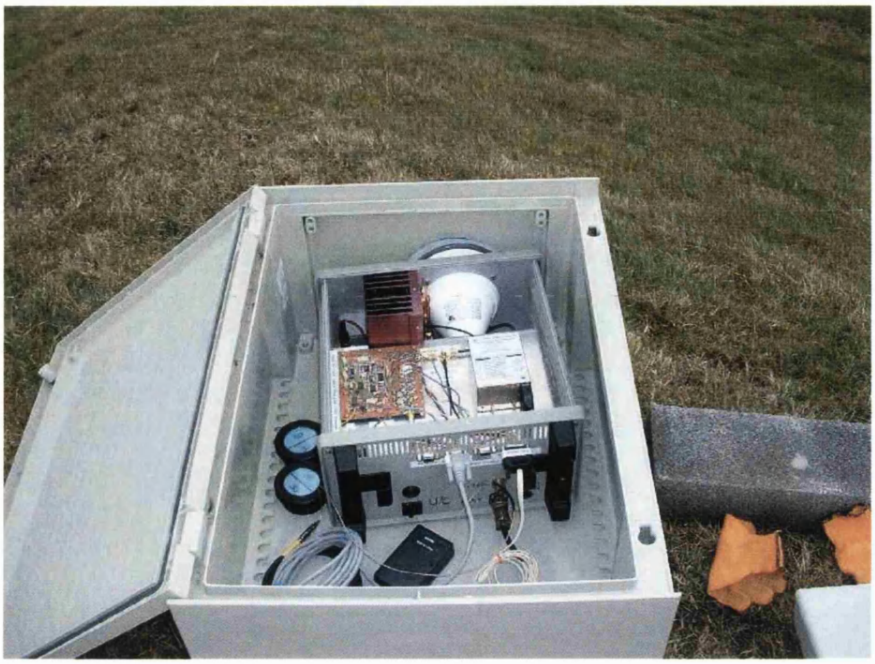

Figure 5.11: Transmitter fitted with new amplifier, aligned in cabinet on site

holding the voltage down. The fault was remedied by cleaning the affected connectors and back filling all of the connectors with silicone sealant to encase the solder connections.

5.6.4 Equipment Deployment

One of the most frustrating issues which was faced during the deployment of the equipment was establishing communications with and gaining permission from the relevant bodies. A significant amount of time was taken trying to gain formal permission to site the transmitter on Bristol Water's Mast Reservoir site. The proposal was accepted in principle at an early stage however progressing to the formal agreement stage proved more time consuming than expected. The physical deployment stage however was both rapid and trouble free.

A more frustrating situation was encountered with respect to gaining access to the roof of the Norwood House accommodation block on the Uni-

versity Campus in order to site the receiver array. The difficulties centred around a reluctance to communicate by any means other than email and a reluctance or inability to respond to emails. Permission was eventually gained however further bureaucracy was encountered in respect to lifting the mast onto the roof. The metalwork for the array could be carried up to the roof by hand however the length of the mast and the fixed plates made it impossible for it to pass up through the tight stairwell.

The mast was hauled up the south elevation because it has no windows and the lift could commence from the roof of the Mechanical Engineering department, whose permission was also required, rather than the ground. This required detailed risk assessments, a significant number of personnel, favourable weather conditions and the presence of a senior member of the estates department.

While access to the Bristol Water site is on a 24 hour basis with site keys being held by ourselves, access to the receiver array is only possible during the daylight hours of week days and then only in favourable weather conditions. The keys are otherwise retained by the estates department. This arrangement has prevented inspection of the array when the data has indicated a problem which has proved frustrating.

Erection of the mast occurred at the beginning of June 2005. The mast with anchorage cables can be seen in Figure 5.12, the array was used in this configuration from this point onwards during the data collection campaign.

Both ends of the link have suffered temporary outages for various reasons. On many occasions the mains supplies have been lost. In the case of the receiver, maintenance work has caused unexpected disruption and on one occasion, the receiver lost power due to direct lightning strike to Norwood House which caused the power supply to disconnect its outputs but did not trip the RCD.

The transmitter suffered from a significant number of power failures early in the campaign and due to the RCD unit, each required a site visit to re-set the trip. To mitigate the costs involved in repeated visits, a UPS unit was purchased to maintain transmission during the short repeated outages experienced during lightning storms. The first subsequent mains failure oc-

Figure 5.12: Receive array with mast erected on the roof of Norwood House

curred shortly after installation and exceed the duration for which the UPS can power the transmitter however since then, the transmitter has remained operational.

Summary

This chapter has described the receiver array which completes the description of the equipment and its preparation for deployment on the experimental link. Chapter 6 now describes the application of propagation modelling techniques. It also introduces the experimental link, established with the previously described equipment.

Chapter 6

The Application of Modelling Techniques

This chapter begins by describing the experimental link which was established using the newly prepared equipment described in Chapters 4 & 5 to collect data for analysis in Chapter 7.

This chapter also introduces the Advanced Propagation Model (APM). In doing so, this chapter forms an important link between the modelling theory presented in Chapter 3 and the experimental link analysis in Chapter 7.

This modelling technique and its use in bridging the gap between theory and experiment is then explored in detail. This exploration begins with a description of a method of synthesising atmospheric refractivity profiles. The application of these profiles to the model is then discussed with a description of a database of the model results following.

Finally the chapter examines how the AOA may be obtained from the output of the model. This forms the basis of an important comparison between theoretical and experimental results.

6.1 Link Information

The link chosen crosses a mixture of urban and rural land. Of particular importance is the section which passes directly over the city of Bath which

can be seen in Figure 6.1. This is of interest because warm, moist air masses can be expected to rise from such urban areas creating temperature inversions and potentially ducting.

Due to the design, size and in particular, the power requirements of the receive array the only practical location for a long term data collection campaign was the University of Bath. Given the elevated nature of the main campus and the various buildings featuring flat roofs the options for establishing links were numerous.

Locating the receive array on a roof was necessary to clear local obstructions and was also desirable from data integrity and equipment security stand points. The roof selected belongs to Norwood House (Figure 6.2), one of the two original accommodation blocks. Standing at nine floors, these dwarf the remainder of the campus. The array, at 10 m in length exceeds the width of the building however it does fit at an angle on the south end of the building as seen in Figure 6.3.

From this position the array can be mounted on the framework to face SW or NE and the frame could, if necessary, be rotated to obtain E and W and SE and NW. The 5 m mast provides two elevated platforms for receiver heads allowing a vertical array to be constructed at the centre point of the main frame. Figure 6.4 shows the frame with the receive array facing NW in a purely horizontal configuration for a test on a temporary link. A number of possible links were investigated with the aim of establishing a link of approximately 20 km kept in mind. A tour of possible transmitter sites narrowed the possibilities somewhat. While the transmitter can be run from batteries, it would be necessary to replenish the power supply regularly and thus a site with a mains supply was highly desirable.

The site selected as the most suitable location for the transmitter is a small underground drinking water reservoir owned and operated by Bristol Water (Figure 6.5). The site is located on a hill near the village of Blagdon and is fed from Blagdon lake which is also owned by Bristol Water. The site, while small, is situated on the crest of the hill facing the University and boasts an unobstructed view of the WSW of the campus. The site is secured by a fence which encloses the reservoir mound and a small control/monitoring hut

Figure 6.1: View of link from receiver array on Norwood House

Figure 6.2: East elevation of Norwood House

Figure 6.3: Receive array framework on the roof of Norwood House

Figure 6.4: Receive array facing NW on framework

Figure 6.5: Bristol Water's Mast Reservoir Site

Figure 6.6: Reservoir mound with transmitter positioned on the NE corner

which houses the reservoir monitoring equipment and a mains power supply.

The transmitter is sited on a temporary purpose-built platform, positioned on the NE corner of the reservoir mound (see Figure 6.6) affording it a clear view over the top of the fence and providing additional local ground clearance. The transmitter is weighted down and strapped to the platform to ensure it does not move in adverse weather conditions. Mains power is derived from the control hut via an Residual Current Device (RCD) equipped plug and an armoured cable. Remote control of the transmitter is provided by the Vodafone mobile phone network which covers the area with more than adequate signal levels.

The link profile can be seen from Figure 6.7 which shows the transmitter site at 310 m and the receiver array at 188 m. The receive array is of course approximately 20 m higher by virtue of being located on the roof of Norwood House.

The link budget for the link from Blagdon to Bath can be calculated using

$$P_r = P_t + G_t + G_r + 20\log\left(\frac{\lambda}{4\pi d}\right) \tag{6.1}$$

Filling in the values for the link in question where the lens horn antennas give a gain 34 dBi each, the transmit power is -0.5dB and the link length is ~ 28.6 km.

$$P_r = -0.5 + 34 + 34 + 20\log\left(\tfrac{0.0082}{4\pi 28600}\right)$$

$$P_r = -0.5 + 68 - 152.8 \tag{6.2}$$

$$P_r = -85.3\,\text{dBm}$$

The receiver sensitivity varies between the units from -90 dBm to -110 dBm. This does not leave a huge fade margin however the array is measuring phase differences rather than amplitude differences.

The first Fresnel zone (Equation 2.21) is calculated for the link:

$$f_1 = \sqrt{0.0082 \times 28600} = 15.31\,\text{m} \tag{6.3}$$

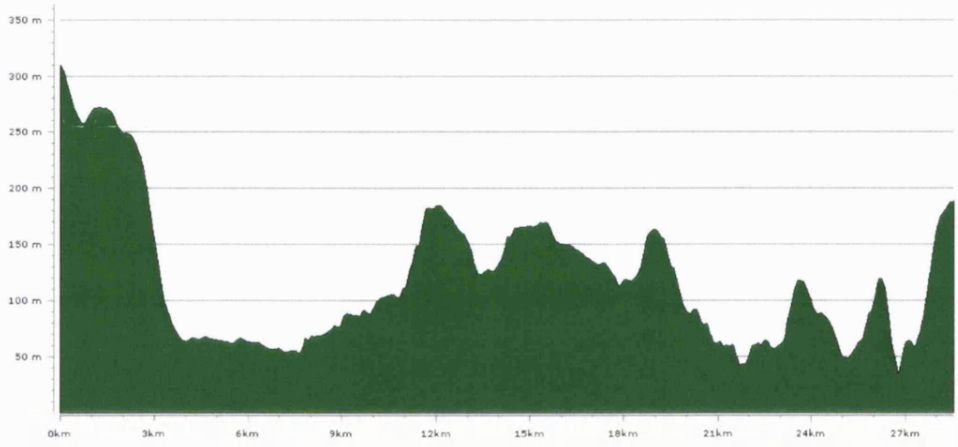

Figure 6.7: Link profile, transmitter (Left) to receive array (Right)

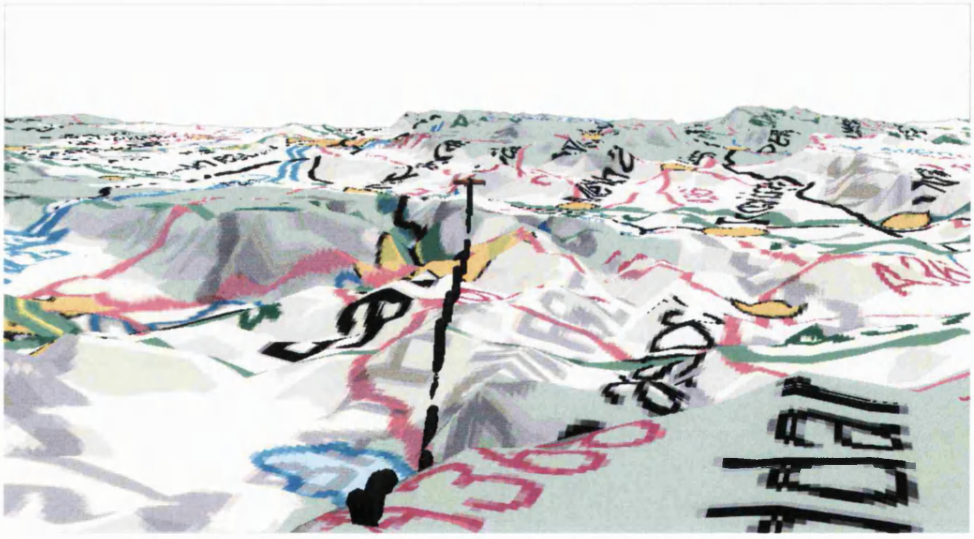

Figure 6.8: 3D link profile, view from transmitter

Examination of the link terrain profile (Figure 6.7) clearly shows that the first Fresnel zone is clear for this link.

6.2 Advanced Propagation Model (APM)

The APM was written by the United States Military. It combines a number of techniques for predicting radio propagation into a single model, capable of operating in several different modes. The modes allow the model to switch the sub-models in or out both dynamically and manually. This permits the user to limit the sub-models applied to a particular problem or allow the model to decide which sub-models are required and when.

6.2.1 Sub-Models

The four sub-models upon which APM is based are Flat Earth (FE), Ray Optics (RO), Extended Optics (XO) and Split-Step Parabolic Equation (PE). By incorporating these four sub-models, the APM merges the Radio Physical Optics (RPO) model and the Terrain Parabolic Equation Model (TPEM) [56].

The APM model has three modes of operation, Full Hybrid, Partial Hybrid and Airborne Hybrid. These modes are dynamically chosen as the model runs, unless that is, the model is forced to use PE calculations alone. This is set by a configuration flag in the input file.

6.2.2 Parabolic Equation Modelling

The APM set to operate with the PE method only is an ideal tool for predicting the clear-air propagation under study in this experiment. The model allows a large number of conditions to be examined by supplying it with refractive index profiles. By repeatedly running the model with different refractive profiles it is possible to build a clear-air propagation database for the link.

By comparing the real dataset obtained using the interferometer with this idealised dataset it should be possible to infer the refractivity profile, or at

least the dominant refractivity profile present on the link at the time in question. Without detailed, not to mention expensive, weather measurements at intervals along the length of the link it is not possible to determine the exact refractivity profile for the link.

The dataset comparison method can of course be combined with knowledge of the weather in the vicinity of the link and documented diurnal refractivity profile changes to further validate the measured results.

The operation of the APM for the construction of the dataset was made slightly complex by the way in which it is written as standard. The model outputs loss values for each height at each step within the specified range. In order to evaluate such properties as angle of arrival it is necessary to extract the electric field values instead.

The source code is written in Fortran 90 which, once a suitable compiler was obtained, ran correctly. It was then necessary to modify the code to output the electric field not the propagation loss. This required significant effort to untangle the internal workings of the model sufficiently to establish where within the program the electric field matrix was valid.

New output routines were introduced. The result was then verified by replicating the steps within the model which derived the loss output values from the electric field matrix. While it was not possible to exactly replicate these operations, sufficient accuracy was obtained to indicate that the differences were due to additional loss calculations.

In order to create refractivity profiles, an algorithm was employed to generate profiles based on a number of parameters. This allowed a range of profiles to be quickly and easily defined within limits and feed sequentially into the APM input file for successive processing.

6.3 Propagation Database

6.3.1 Five Parameter Refractivity Model

In order to test the Advanced Propagation Model (APM) and to provide a reference database of link propagation a model capable of defining realistic

refractivity profiles was sought. The model selected for this task, taken from [57], produces piecewise-linear refractivity profiles.

The surface-based ducts which form in the troposphere can be associated with either convective or stable boundary layers, (see Figure 2.3 in Chapter 2). The model selected is capable of modelling both cases. As can be seen from Figure 6.9, it consists of an evaporation duct profile for the surface layer and line segments for the convective boundary layer. These line segments correspond to the mixed layer, the capping inversion and the free troposphere.

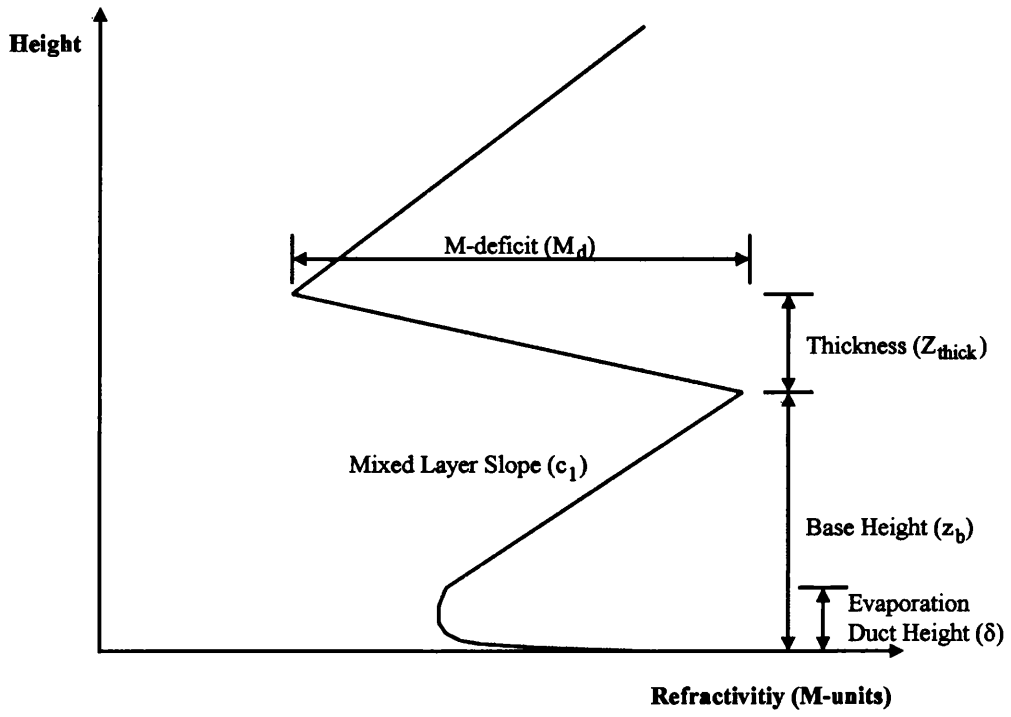

Figure 6.9: Five parameter refractivity model profile

The model allows the line segment corresponding to the mixed layer to take on negative values instead of the fixed 0.13 M units m^{-1} slope and it therefore does not conform to the meteorological definition when a stable layer is present.

The model gives the modified refractivity M as a function of height (z, m) as follows.

$$\mathrm{M}(z) = \mathrm{M}_0 + \begin{cases} \mathrm{M}_1 + c_0\left(z - \delta \log \frac{z}{z_0}\right) & \text{for} \quad z < z_d \\ c_1 z & \text{for} \quad z_d < z < z_b \\ c_1 z_b - \mathrm{M}_d \frac{z - z_b}{z_{\text{thick}}} & \text{for} \quad z_b < z < z_t \\ c_1 z_b - \mathrm{M}_d + c_2 (z - z_t) & \text{for} \quad z_t < z \end{cases} \tag{6.4}$$

where:

- $c_0 = 0.13$
- δ = Evaporation Duct Height, m
- c_1 = Slope in Mixed Layer
- $c_2 = 0.118$ M units m^{-1}
- $z_0 = 0.00015$
- $z_d = \begin{cases} \frac{\delta}{1 - \frac{c_1}{c_0}} & \text{for} \quad 0 < \frac{1}{1 - \frac{c_1}{c_0}} < 2 \\ 2\delta & \text{otherwise} \end{cases}$ while $z_d < z_b$
- z_b = Trapping layer base height, m
- z_{thick} = Thickness of the inversion layer, m
- $z_t = z_b + z_{\text{thick}}$
- $\mathrm{M}_0 = 330$ M units
- $\mathrm{M}_1 = c_0 \delta \log \frac{z_d}{z_0} + z_d (c_1 - c_0)$
- M_d = M Deficit of inversion layer

6.3.2 Database Generation

The variables (z_{thick}, z_b, M_d and c_1) were used to create the range of profiles for the model dataset. The range and spacing used for each variable is given in Table 6.1.

Table 6.1: Parameter Values

Variable	From	To	Step Size / Intermediate Values
c_1	-0.7	0.4	-0.4, -0.1 and 0.2
M_d	0	100	20
z_b	140	500	20
z_{thick}	10	100	10
δ	2	-	Fixed

6.3.3 Propagation Database Analysis

The result of running the APM with the parameters given in the previous section was a database of output images and corresponding refractivity profiles for each of the 5700 parameter combinations. In each case the image pixels represent the electric field strength at the pixel location.

The images indicate the field strength in a visual representation of the case, given a single refractivity profile, homogeneous along the link's length. A vertical slice may however be taken from the image and Fourier transformed to yield the beam pattern. This pattern indicates the direction of greatest field, in other words, the AOA.

There are some considerations in taking this approach. Firstly, the slice needs to represent the receiver. This is achieved by limiting the height range of the slice which is Fourier transformed. Limiting the height range keeps the DC component of the spectrum in check. Otherwise this would dominate the spectrum due to the much larger proportion of the height range which experiences a uniform field. The height range considered represents the receiver array both in hight by matching the height of the synthesised receiver created by the array and in position with respect to the receiver array being on the roof of Norwood House.

The other clear consideration is the physical AOA created in the experimental equipment set-up which is replicated within the model by setting the heights of the transmitter and receiver array together with the terrain which lies in between.

The geometrical AOA resulting from the experimental set-up in this ex-

periment is 0.2° and as a consequence, this will form the direct line of sight offset. In the analysis in this thesis, this is to be considered as a positive shift, i.e. an angle above the horizontal as seen by the receiver array.

In both the experimental and model analysis, the AOA is considered to be the apparent angle from which the strongest component of the received signal makes at the receiver array to the horizontal. In the case of the model, the experimental geometry places the transmitter 0.2° above the horizontal and this is modelled as an absolute offset. AOA fluctuations are expected about this angle for the modelled result.

The experimental results provide relative not absolute AOA about the geometric AOA although this is not numerically added to the results as presented.

Other AOA definitions might try to examine all the angles from which contributory signal components arrive. For the purposes of this study such detail is not required as it is apparent that there is very little spread of AOA about the dominant angle for all but the more extreme cases. An example of such an extreme case is examined however to demonstrate the multiple component angles.

The mathematical background to support the calculation of AOA from the model output is taken from [52].

From definition, the beam pattern for a field component ψ in direction θ is

$$B(\theta) = \lim_{r\to\infty} re^{ikr}\psi(r\cos\theta, rsin\theta) \tag{6.5}$$

In cylindrical coordinates, ψ is related to the PE function u thus

$$\psi(x,z) = \frac{e^{ikx}}{\sqrt{kx}}u(x,z) \tag{6.6}$$

Taking $x_0 = 0$, the far field can be written

$$\psi(r\cos\theta, r\sin\theta) \sim \frac{1}{\sqrt{2\pi}}e^{-i\pi/4}\frac{\sqrt{\cos\theta}}{r}e^{ikr}\int_{-\infty}^{+\infty} u(0,z')\,e^{-ikz\sin\theta}dz' \tag{6.7}$$

Which is proportional to the Green's function. The beam pattern can be rewritten as

$$B(\theta) = \frac{\sqrt{\cos\theta}}{\sqrt{2\pi}} e^{-i\pi/4} \int_{-\infty}^{+\infty} u(0,z)\, e^{-ikz\sin\theta} dz \tag{6.8}$$

Taking an example from the profile database, shown in Figure 6.10, a clear bending of the radio path can be seen. The main beam appears to strike the hill below the summit. Taking the Fourier transform at this point should yield a clear AOA deviation. Using simple geometric techniques, the angle of this beam can be determined and the thus the method may be validated.

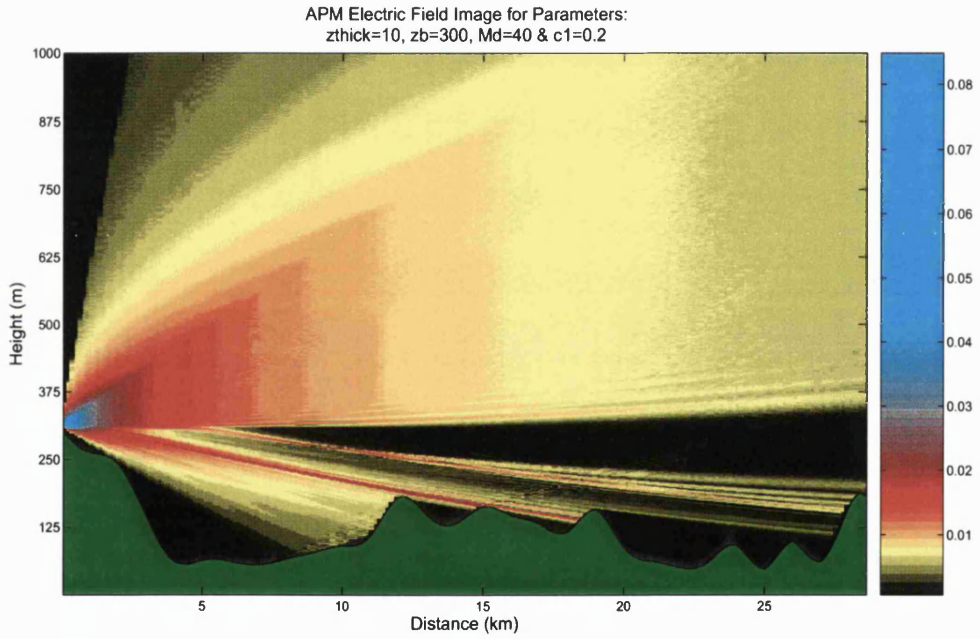

Figure 6.10: Electric field for APM propagation case with an interpolated terrain superimposed.

Taking a geometrical approach, shown in Figure 6.11 which is a magnified portion of Figure 6.10, horizontal distance $27750 - 23000 = 4750\,\text{m}$ and vertical distance $181 - 158 = 23\,\text{m}$, the AOA for the main beam is 0.28°.

Using an average of the 4096 point Fourier transforms of the field between

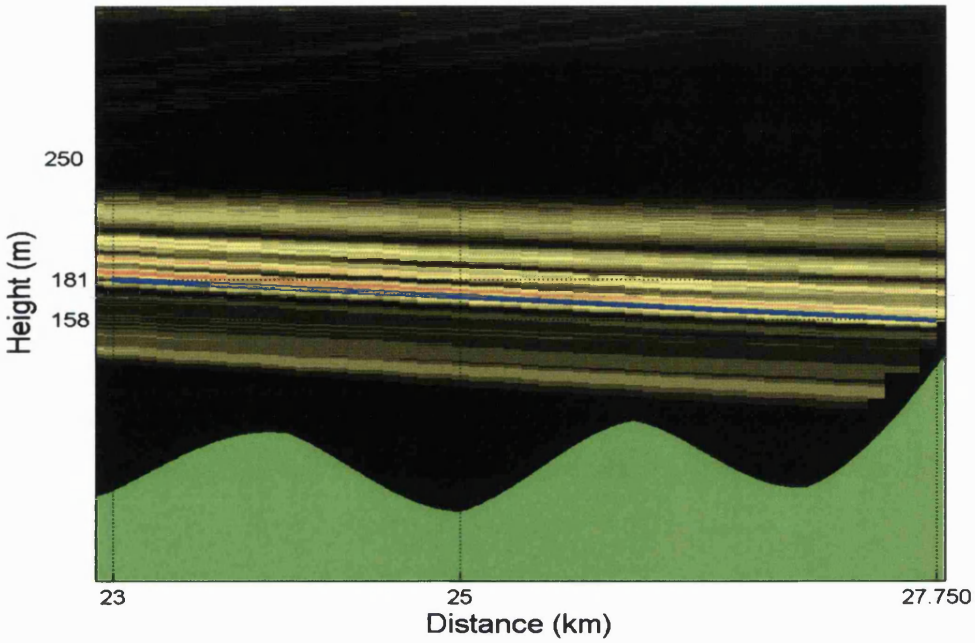

Figure 6.11: Magnified portion of Figure 6.10 with superimposed blue calculation line.

23000 and 27500 over an appropriate height range, the Fourier method yields the beam pattern of Figure 6.12.

This shows that the dominant AOA appears quite spread with peaks at an angles of 0.3°, 0.45° and 0.6°. This appears to support the approximation made using the geometrical approach, given that the figure of 0.28° falls close to one of the peaks. Clearly the Fourier technique has revealed more than the simple geometric approach in this case.

To test the effect of the averaging used in the above example, that same example is again used with the average of Fourier transforms from only three range points; 27300, 27400 and 27500 m. The result, shown in Figure 6.13, indicates and increased number of peaks within the band 0.2° - 0.6°. Also worthy of note are some angles from which significantly less power is originating, demonstrating that there are a number of distinct angles of arrival.

This difference is to be expected given the reduction in range locations

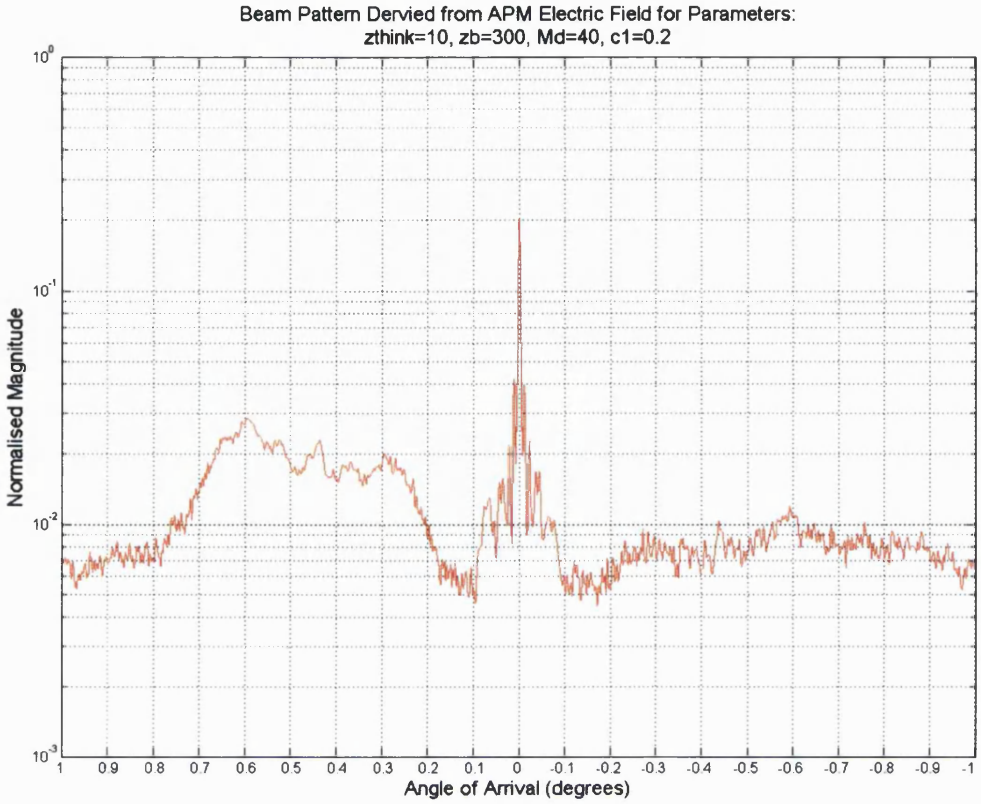

Figure 6.12: Beam pattern for ducting case

being averaged together. The broad estimate is not corrupted to the point of obscurity by this smaller range set and more detail of the individual angles from which the signal appears to arrive is revealed. This is an important result because to obtain a realistic AOA measurement from the electric field at the receiver site it is necessary to limit the average to those range points which can be argued to be on the receiver site. Clearly this can be done without affecting the estimate of the dominant AOA and the spread of component angles is also revealed.

Taking the same example, this time considering the electric field at the end of the link, where the receiver is situated, the method yields the beam pattern shown in Figure 6.14.

The beam pattern of Figure 6.14 shows that there is a band of AOA

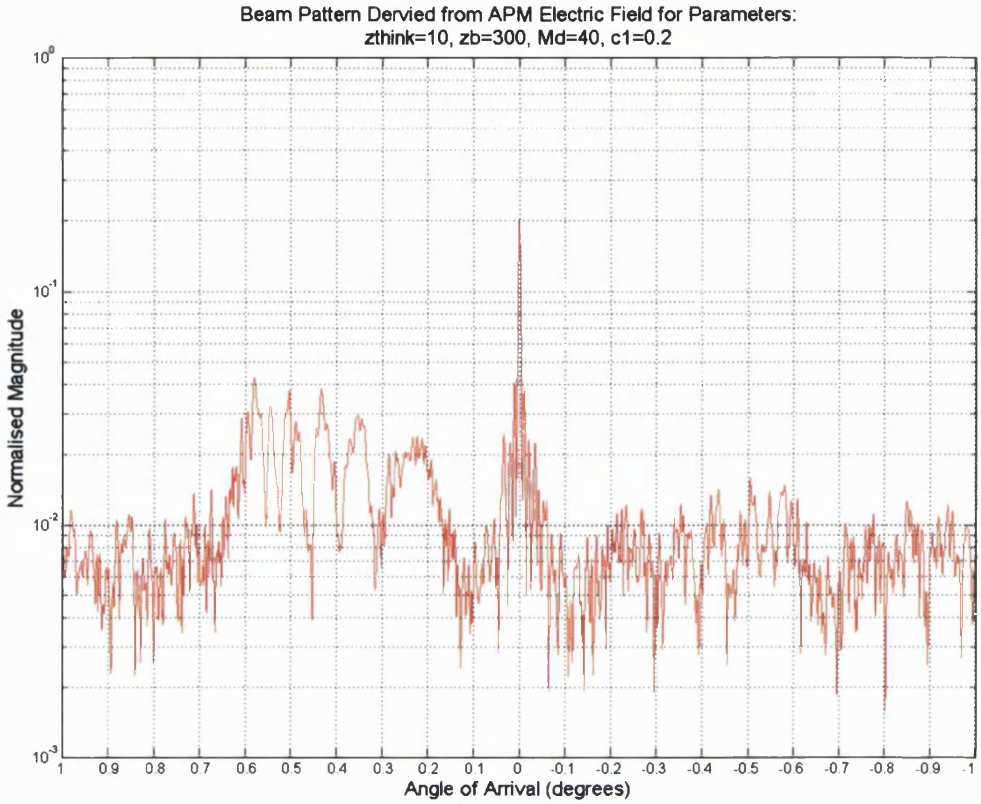

Figure 6.13: Beam pattern for ducting case with only three range points averaged

roughly centred about 0.2°. The implication is that although this is a significant ducting case, the effect has been to split the signal early in the link path, creating a dead band above the receiver site. The apparent AOA is therefore not too far from the geometric slant of then link. Further, the image of Figure 6.10 does indicate an upward curve to the beam as it approaches the end of the link. It can be seen that the part of the beam which reaches the receiver site is affected more so than the portion of the beam considered in the earlier Figures.

Having examined a case of ducting, it is appropriate to look at a less severe case (Case 1), shown in Figure 6.15, which does not lead to ducting. The corresponding Beam Pattern is given in Figure 6.16. This shows that

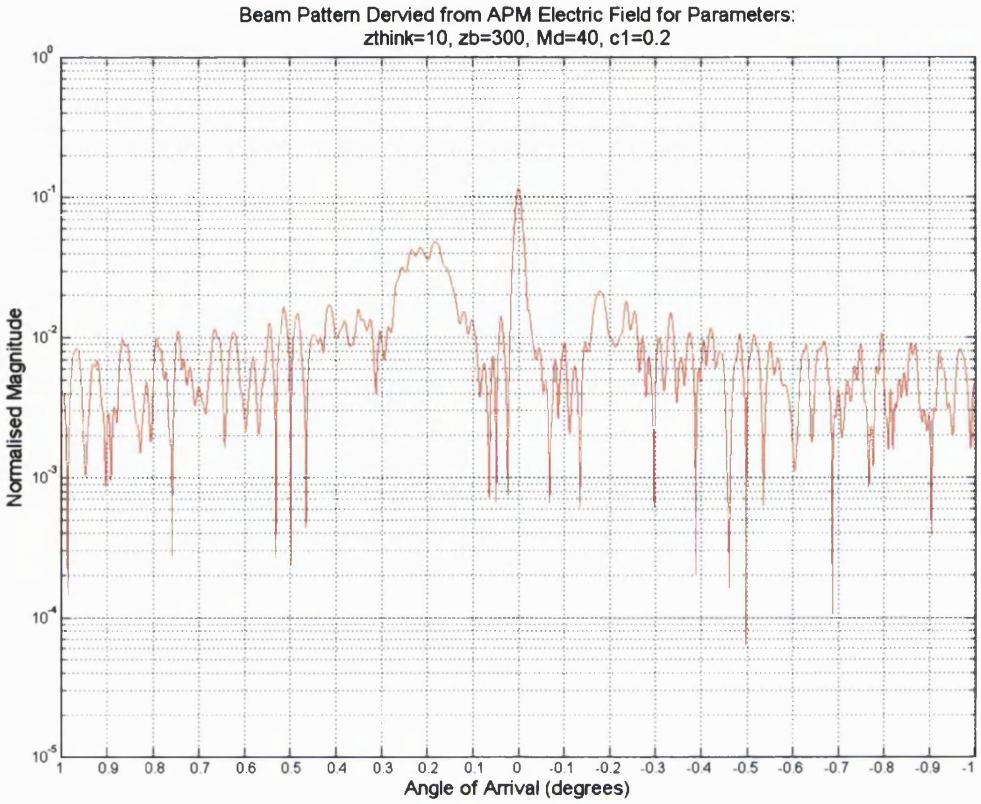

Figure 6.14: Beam pattern as seen by receiver for ducting case

the AOA in this case is centred on the geometric AOA of 0.2° and has an almost even contribution from the angles in the range 0.1° - 0.3°.

Finally another extreme case is considered (Case 2), shown in Figure 6.17. In this case it is clear that the electric field near the receiver is zero or close to it as the signal is refracted away from the line of sight path. Examining the beam pattern obtained in this case (Figure 6.18) it is clear that there is no AOA which is as expected and demonstrates that the previous analysis is valid. With no signal reaching the receiver site, the model has yielded no AOA. This could be used as a baseline case to separate the background from the AOA by means of deconvolution.

In the following, the electric field of Case 1 has been written as Electric Field $(Case1)$ and the mathematical operator $*$ denotes convolution.

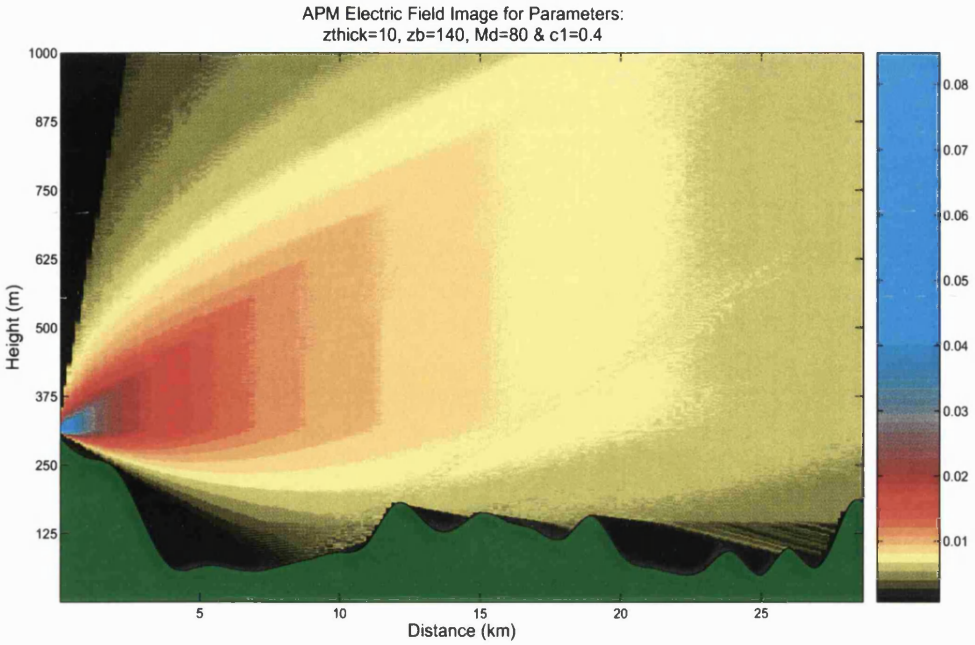

Figure 6.15: Electric field showing the effects of a less severe refractivity profile - Case 1

$$\text{Electric Field}\,(Case1) = \text{Electric Field}\,(Case2) * \text{Refractivity Effect} \quad (6.9)$$

Bearing in mind that the Fourier transforms of these are the beam patterns it is necessary to perform the deconvolution thus;

$$F\left[\text{Electric Field}\,(Case1)\right] = F\left[\text{Electric Field}\,(Case2)\right] \times \text{Refractivity Effect} \quad (6.10)$$

Thus

$$F^{-1}\left[\frac{F\left(\text{Electric Field}\,(Case1)\right)}{F\left(\text{Electric Field}\,(Case2)\right)}\right] = \text{Refractivity Effect} \quad (6.11)$$

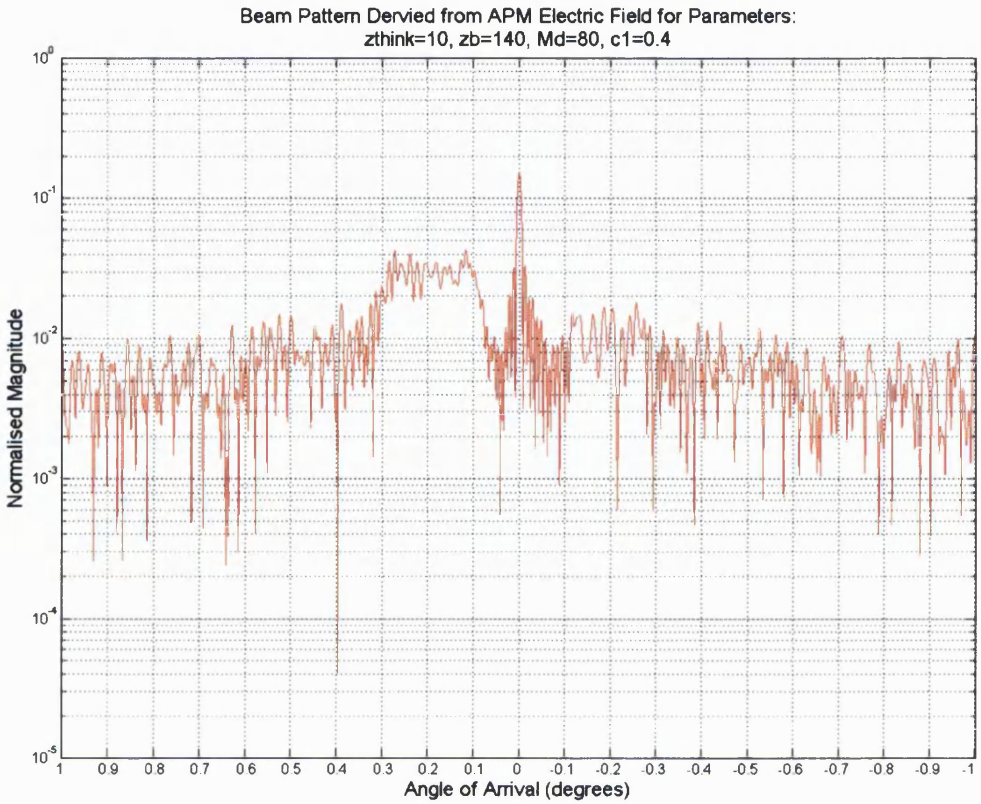

Figure 6.16: Beam pattern as seen by receiver for Case 1

The result (shown in Figure 6.19) in this case is not useful. The technique suffers from high instability and the propensity to remove the wanted signal.

The conclusion has to be that the deconvolution technique can play a useful role in analysing beam patterns but its use is not universally appropriate and some degree of caution is necessary in its application due to its instability. It is also not necessary for the purposes of this study to use deconvolution because the AOA and its behaviour can be clearly seen without using such techniques.

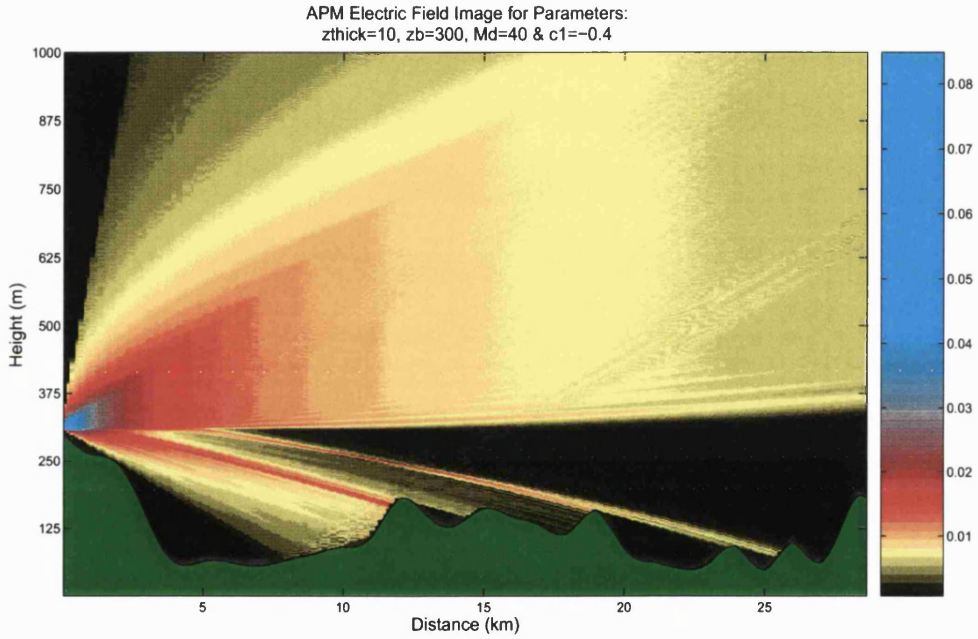

Figure 6.17: Electric field showing ducting resulting in no signal at receiver location - Case 2

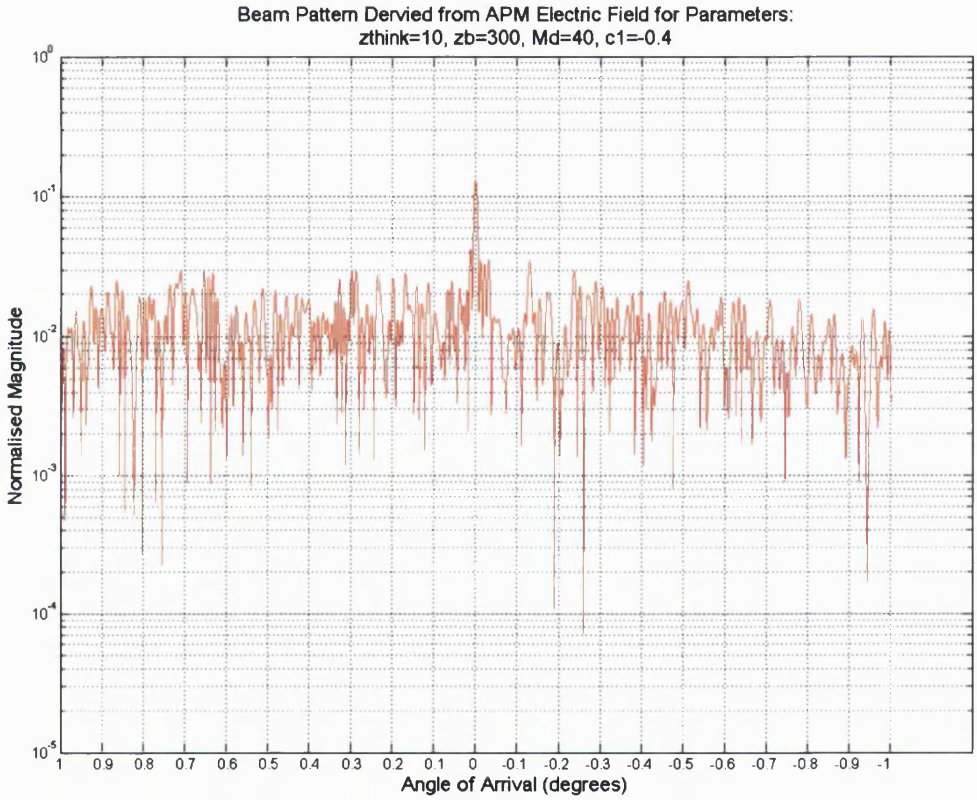

Figure 6.18: Beam pattern as seen by receiver for Case 2

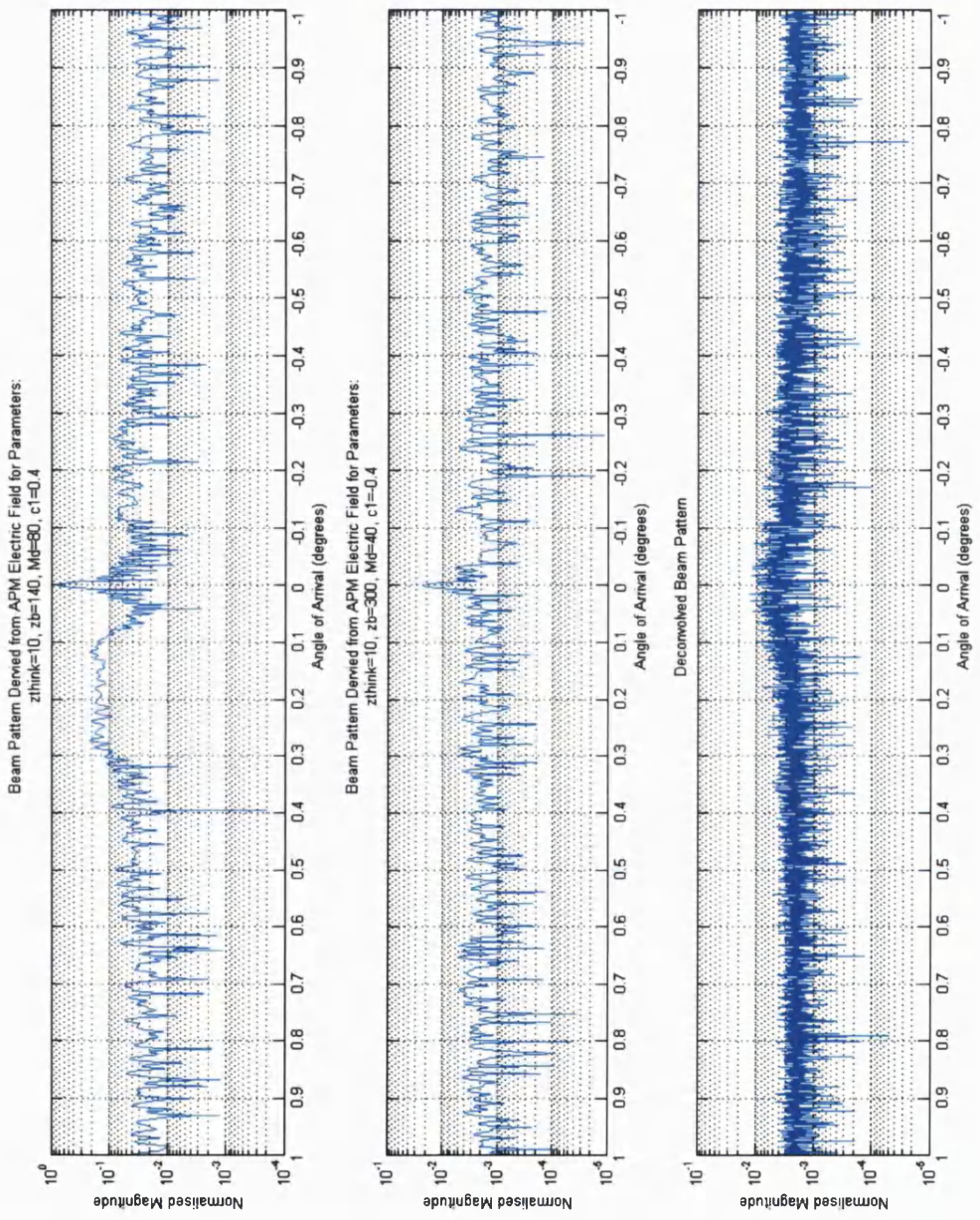

Figure 6.19: Expanded view of beam patterns for Case 1, Case 2 and their deconvolution

Chapter 7

Analysis of Link Data

7.1 Analysis Overview

This chapter takes the data collected using the equipment, detailed in Chapters 4 and 5, over the course of the data collection campaign. The nature of practical experiments leads to unforeseen problems and equipment related difficulties which give rise to periods of outage. The term outage covers a multitude of different scenarios but is used because it accurately describes the net result, no data or meaningless data.

Clearly an outage at the transmitter site does not stop data being collected at the receiver, however the data collected during this event would be meaningless since there is no signal to which the interferometer can lock.

This experiment is no different to any other and it has suffered a number of outage events during the course of the data campaign arising from a range of causes. In deciding how to analyse the substantial quantity of data collected, it was clear that these outage events lead to natural breaks in the dataset. In addition to large outage events, the data is affected by the random drop-out issue with the reference MMIC (see Section 5.6.1). These events range in duration but are clearly identifiable and they can easily be classified as either a 'blip' or an outage. No attempt to correct the blips has been made nor have they been excluded from the data. Measured data by its nature has outlying points and these are considered as exactly that. In the analysis we are examining trends, the presence of the odd blip or two should not

Table 7.1: Analysis Periods

Period	Start	End	Summary
1	04/06/05	17/06/05	Warm, mostly dry
2	06/07/05	12/07/05	Hot and dry
3	19/07/05	27/07/05	Warm, some rain
4	06/09/05	21/09/05	Warm, heavy showers
5	07/01/05	22/01/06	Cold with snow

adversely affect the result.

The periods of data identified as being free from outage events and suitable for analysis are shown in table 7.1.

7.2 Analysis Techniques

In order to analyse the vast quantity of data collected by the interferometer it was necessary to process the data in manageable chunks. The sampled data (102400 samples s^{-1}) is averaged by the logging software prior to being written to disk (100 samples s^{-1}). The data is then automatically decimated by a factor of 100 providing a high resolution archive (100 samples s^{-1}) and a smaller lower resolution file (1 sample s^{-1}) covering 24 hours for analysis.

These decimated files, containing one sample per second form the basis of the analysis process. The raw data can be plotted to indicate the status of the link. These plots reveal the tell-tale signs of outage events and severe weather effects and are used to provide effectively a heartbeat check on a day-to-day basis.

To conduct a meaningful analysis over the periods selected, it was necessary to develop a suite of analysis tools. The size of the decimated files is still considerable and manually handling the data within MATLAB is not an option.

The first tool developed in the suite processed the data to yield the phase measured by each of the three channels. These are the phase differences between each of the three receive elements and the reference, including an

arbitrary system phase shift. The key information available from these plots is the phase change with time, from this, fluctuations in AOA may be determined.

In addition to the data collected by the interferometer, several external sources of data are used to build up a picture for the purposes of analysing the data in context. The first of these additional sources is weather data collected locally by amateur meteorologists. Amateur, because they own and maintain their own private weather monitoring stations as a hobby though that's not to belittle the investment and effort expended on this venture. Additional meteorological data was obtained from a logging station located on the roof of Norwood house, operated by another research group.

The location of the weather station used is Horfield/Filton, Bristol. This is a station of sufficient complexity to indicate that it belongs to someone with more than a passing interest in meteorology. As a substitute to a weather station sited on the link path it is reasonable. It certainly gives an indication of the conditions on the link which is adequate for the purposes of this investigation. Unfortunately the weather station which is sited in the same location as the receiver failed to operate either reliably or accurately during the periods being examined. Since it is owned and operated by a third party, it was not possible to influence this situation.

The meteorological data provides a measure of temperature, humidity, pressure and by calculation from these, surface refractivity. The resulting plots yield the first indication of how the link data is affected by meteorological conditions. Whilst some lead or lag can be expected due to the relative locations of the weather station the the link, it serves to expose the general trend viewed over 24 hours.

The next major contributory source of data is the MM5 model. This provides meteorological data for the link itself. In order to produce the high resolution profiles for the link, it requires historical weather data to initiate its calculations and a period of 'run up' to achieve the desired accuracy. It is then able to supply similar parameters to the weather station which can once again be used to calculate a modified refractivity profile. The difference is that this data much more closely relates to the link path.

Further discussion of the MM5 model may be found in Appendix A. At this juncture though it is sufficient to say that the implementation of the MM5 model isn't a trivial exercise, requiring a working knowledge of Unix and significant investment in computer hardware, the author is therefore extremely grateful for the assistance of Mr Duncan Hodges for supplying this data.

Once again, plotting the received phase data together with the modified refractivity profile from the MM5 model permits qualitative analysis of the trends.

The next tool in the analysis toolbox is Snell's Law. Herein lies a problem of implementation, however a reasonable attempt is made nonetheless.

The use of Snell's Law is aimed at providing a very basic estimate of the AOA given the modified refractivity profile from the MM5 data. This bridges the gap between the modelled weather data and the modelled propagation model APM.

Snell's law is implemented for a range of launch angles for the MM5 modified refractivity profile at 6 am, 12 noon and 6 pm on each day of the analysis period. This provides a snapshot AOA estimate, useful for obtaining a feel for the effect of refractivity on the AOA.

Finally, the modified refractivity profile from the MM5 model can be passed to the APM to generate the propagation conditions along the link. As this model is computationally more efficient than the implementation of Snell's Law, it can be used to take hourly snapshots and generate the AOA spectrum for each.

Throughout the analysis of the periods, the receive units are referred to by a colour coding scheme. Referring to Figure 5.12, the units are colour coded, from the top of the mast, Yellow, Red and Blue with the Orange unit located further along the framework. The 'Red' unit is connected as the reference unit.

7.3 Period 1 Analysis

The first analysis period spans 14 days in the first half of June 2005. This period experienced almost no rain, the rain which did fall affected the 1st, 2nd & 12th days of the period. The quantity of rain was low on these occasions, the 12th day seeing the most with approximately three hours of intermittent rain with a peak rainfall of $20\,\mathrm{mm\,h^{-1}}$.

The temperature statistics for this period are given in Table 7.2 and indicate that period 1 was generally warm. The definition of daytime and night-time used in the generation of these statistics is 6 am-6 pm and 6 pm-6 am respectively.

Table 7.2: Period 1 Weather Statistics

	Period	Daytime	Night-time
Max	$24.7\,°C$	$24.7\,°C$	$21.7\,°C$
Min	$5.3\,°C$	$5.4\,°C$	$5.3\,°C$
Avg	$15.0\,°C$	$16.4\,°C$	$13.7\,°C$

With that noted, examination of the phase difference graphs of Figure 7.1 in conjunction with the weather traces of Figure 7.2, makes it apparent that there is a trend towards an increase in the phase jitter during the daylight hours. Further there is a shift in the mean phase differences which also follow this pattern.

While this relationship is clear to see, it is less obvious why this occurs. It would be easy to conclude that this is the result of small scale refractivity changes (scintillation) caused by solar heating of the ground and therefore that the effect was real. There is however another blindingly obvious explanation, that of solar heating of the equipment. During warm weather in a month such as June it is not abnormal for the equipment to cycle through a significant temperature range. Such a heating effect would lag the daylight hours due to the latent heat capacity of the equipment housings. Some effect from the wind could also be reasonably expected. A light breeze at ground level tends to coincide with a significantly cool wind 10 floors up on the roof

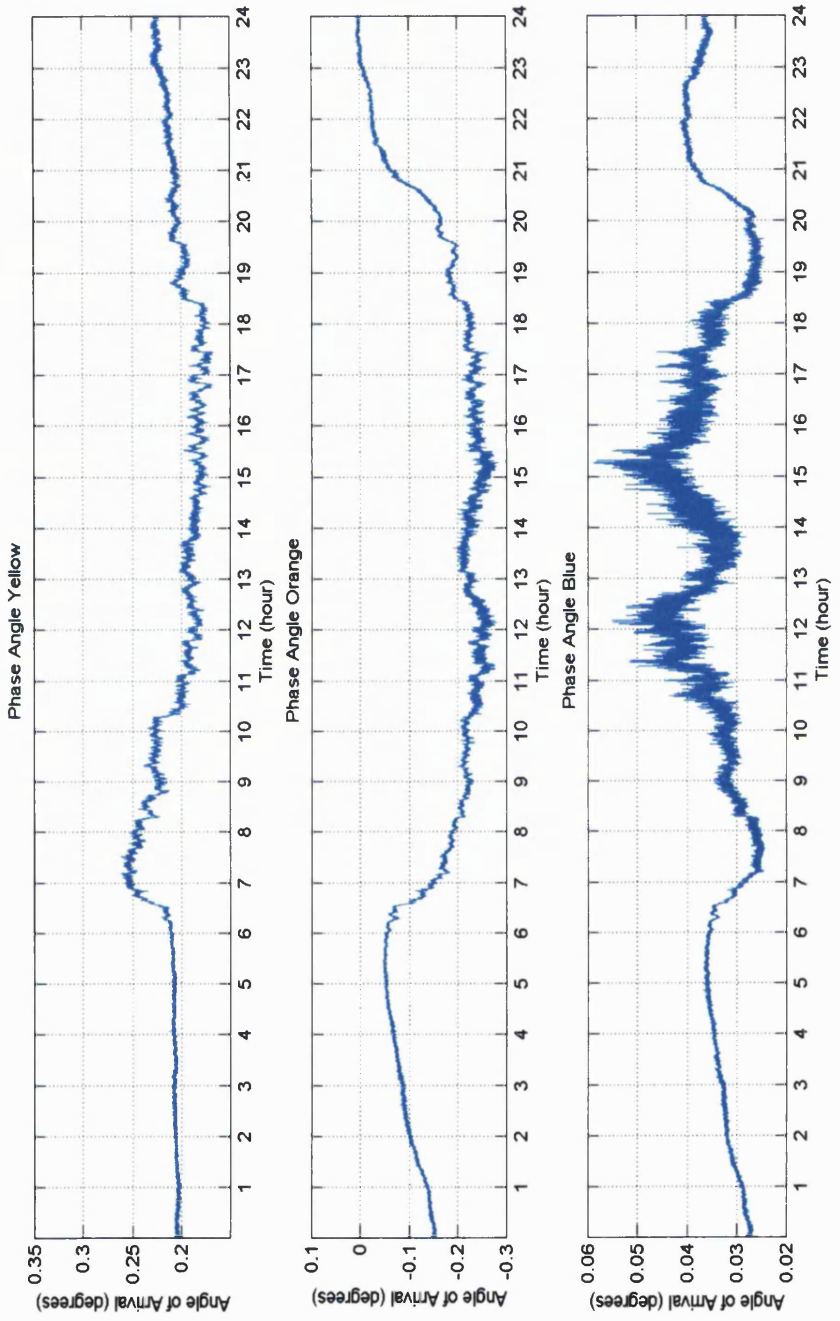

Figure 7.1: AOA difference plots, day 7

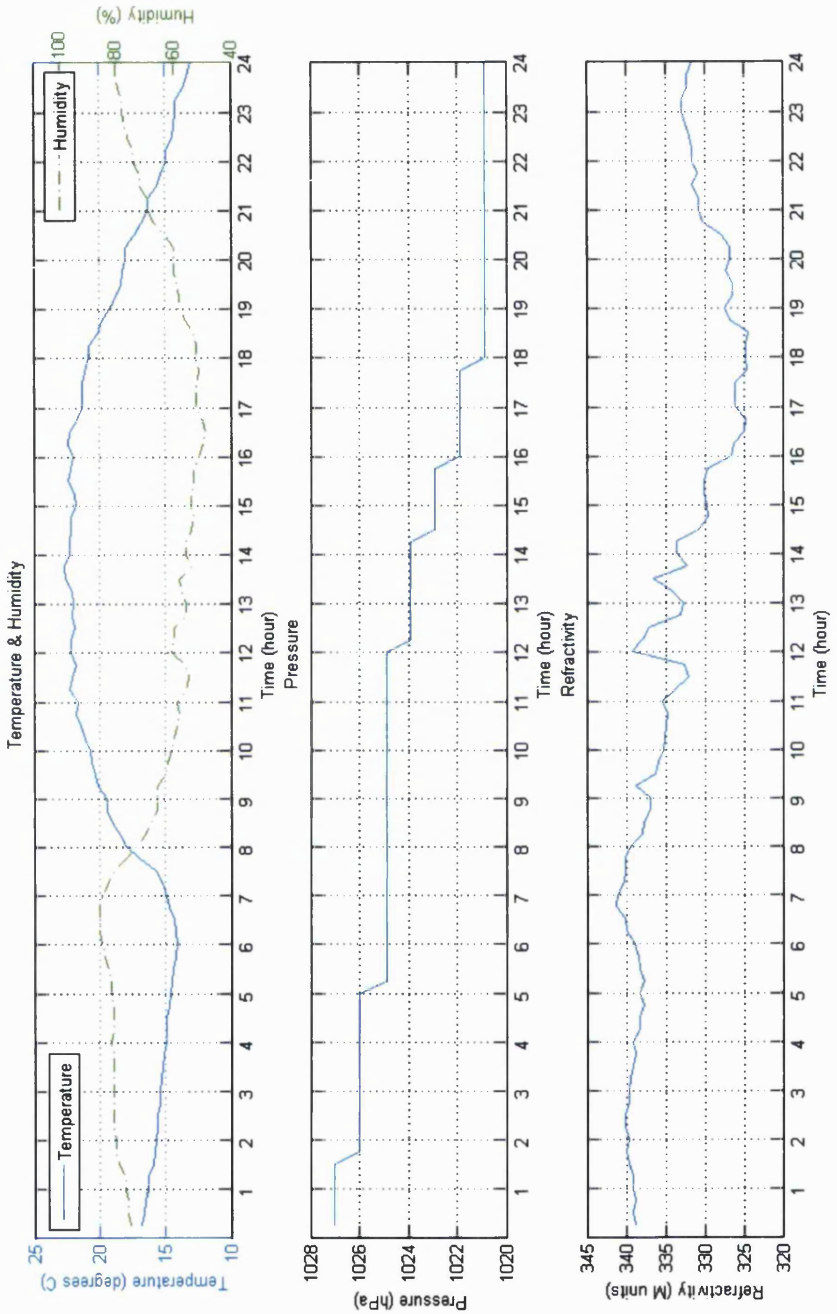

Figure 7.2: Weather plots, day 7

of a building, especially when that building is in an exposed hill top position as in this case.

Close inspection of the plots for the period yields a confidence that a simple temperature relationship is not present since there are instances of events affecting the phase which cannot be associated with temperature events. Further, there is no noticeable latency between the temperature cycle and the phase. Given the knowledge that the receive units generate heat whilst operating and are somewhat thermally isolated from the sealed cabinets themselves it would be reasonable to expect a significant lag between the air temperature and any temperature dependent phase effect.

The conclusion is therefore that the cycle of phase activity spanning a 24hr period is the result of real effects on the microwave link and not merely an equipment temperature effect.

The next step in the analysis is to examine the phase plots in conjunction with the surface refractivity, as given by the meteorological data and MM5 modified refractivity profiles.

Visually identifying periods of interest, reveals an event on Day 7, beginning at midnight. The phase differences indicate a gradual but sustained change over the first six hours, this is followed by a rapid change. Examining the MM5 modified refractivity plot reveals a corresponding period with distorted contour lines.

Plotting the modified refractivity given by the MM5 at hourly steps throughout the day shows that an inversion develops during the course of the early hours. The duct appears at around 1 am and develops over the next 4 hours before rapidly reducing until non-existent at 7 am. A slight ground based duct forms at 8 am but is gone by 9 am. The refractivity is uniform throughout the remainder of the morning. Developing from 9 pm there is a ground based duct which develops reaching a peak at 10 pm. It reduces slightly thereafter but is still present and significant at midnight.

In order to obtain a better understanding of how the refractivity changes during the course of the day, a larger number of plots can be combined in an animated gif file which can be played as a movie. Figure 7.3 shows key frames from such a file, over the course of a day. The result reveals significantly

greater detail than the hourly plots. From viewing the images at speed it becomes clear that a slight inversion develops shortly before 01:00.

At about 500 m this slight, barely detectable kink in the refractivity becomes more significant. The refractivity in the lower 500 m becomes curved indicating the development of a ground based duct. The bend in the profile increases in sharpness as the early hours of the morning progress. The duct reaches a peak sharpness at 04:30. This feature then decays and at 06:15 it begins to move up in height as it continues to decay. This clearly occurs as the sun rises, causing the refractivity to homogenise as the inversion air layer also rises due to thermal convection.

Shortly after 18:00 a slight bend in the refractivity profile is observed which steadily grows until shortly before 21:00. This bend reduces in the next half an hour before slowly increasing in height towards midnight.

The descriptions arising from the hourly plots and the more detailed animation clearly differ in detail. The gradual rise of the morning inversion was not clear from the hourly plots as the reduction in the severity of the inversion was significant between snapshots. Clearly the animation offers a clearer understanding of the events and is therefore a useful tool for use in analysing such events.

When the description of the refractivity is compared to the phase difference traces from the interferometer (Figure 7.1) it becomes clear that the equipment has detected AOA fluctuations caused by these events. The ground based duct which forms in the early hours (midnight to 5am) appears to cause a AOA change of approximately 0.5° in one trace, significantly less in the other two. All three traces show very little jitter during this time and some slow AOA change.

The traces then mark the rapid decay of the duct with an equally rapid change in AOA and the onset of increased phase jitter. This jitter increases during the day superimposed on a slower trend. These fluctuations are believed to be caused by scintillation as the ground is heated by the sun.

When the 2^{nd} ground based inversion appears shortly after 18:00, the phase plots record a lessening in jitter and the beginning of a trend of significant AOA variation which persists throughout the evening, the most rapid

change taking place between 20:00 and 21:00. Clearly once the sun has set, the air temperature falls and the warm ground continues to heat the air immediately above it creating a temperature inversion. The generation of scintillation reduced hence a reduction in phase jitter is noted.

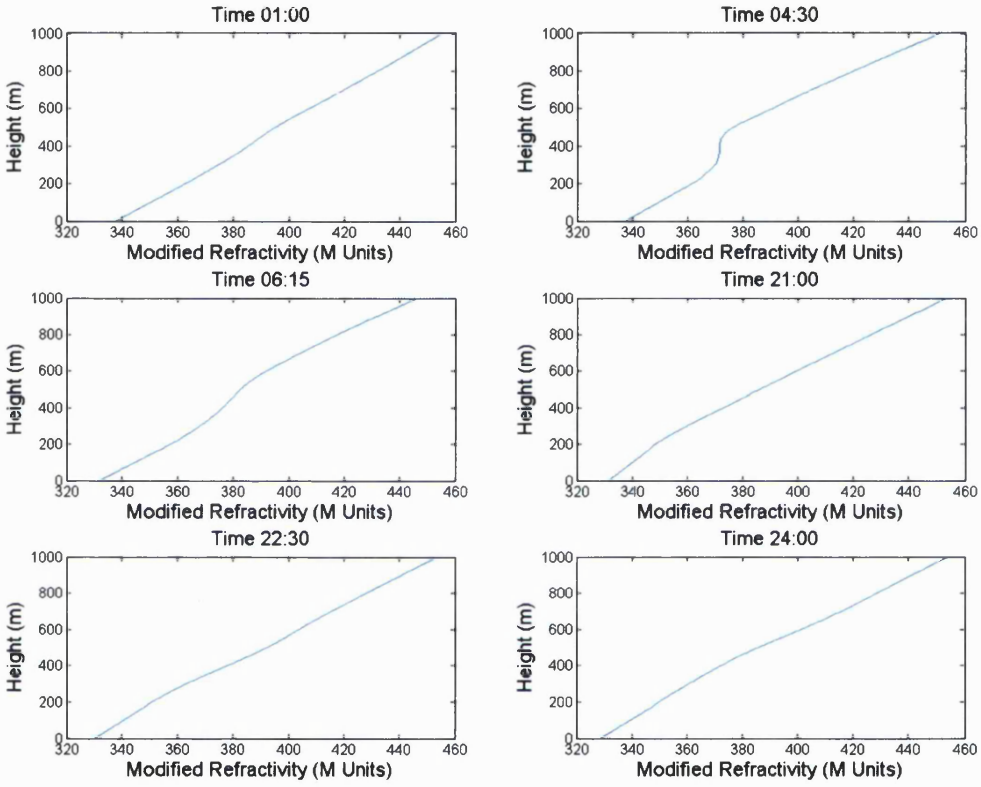

Figure 7.3: Key refractivity profiles from day 7

The use of the variable speed movie technique was next employed to investigate how the electric field is expected to alter throughout the day as the refractivity changes. The APM was used to generate images every 15 mins throughout the day, this was considered a reasonable compromise between movie resolution and speed of calculation. This same analysis generated the data for the AOA plots discussed later in this section.

The APM plots had previously been produced on an hourly basis and in

common with the hourly refractivity plots did not tell a particularly clear story. By playing the 96 images which make up the analysis at relatively high speed, it is clear that the APM predicts periods of relative calm and activity (Figure 7.4).

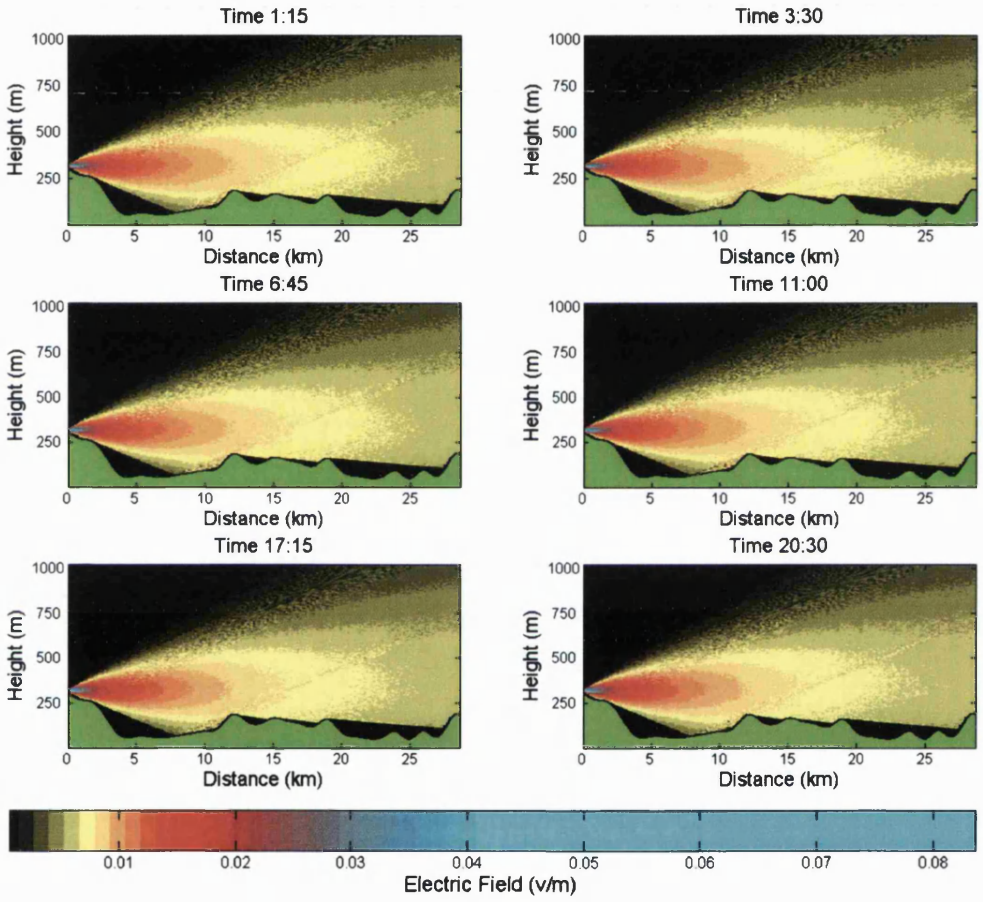

Figure 7.4: Key APM frames from day 7

Between 00:15 and 03:30 a downward sweep effect can be seen as a direct line path develops. This describes a departure from the ordered radiation pattern. This feature remains, beginning to reduce at 05:15. Clearly this is the result of the developing duct seen on the refractivity plots.

Alongside this feature, there is a clear change at about 08:00. Prior to

this time there is significant alteration in the electric field. From 08:00 until approximately 18:00 the bulk of the field remains noticeably steady with only small scale jitters. This corresponds to the interferometer observations.

One final observation is that there are some graceful changes in the diffraction pattern seen at the third major hill, ~19 km. These changes mimic the slow changes noticed on the interferometer phase difference plots.

The conclusion we draw from this analysis is that the APM is validating the experimental results.

The next logical step is to use the final state of the electric field to estimate the AOA and examine the trends over the day. From initial examination of the AOA plots viewed as a movie, it becomes clear that there are identifiable trends.

Since the patterns aren't particularly clear when viewed using the movie technique, the FFT plots were considered as a surface plot (Figure 7.5) instead. This type of plot, when viewed from above with an adjusted colourmap yields an clearer indication of how the AOA varies over the course of the day.

The surface plot shows the DC peak with a second substantial peak which varies during the course of the day, the dominant AOA. With a value constantly over 0.2° which is the physical angle created by the geometry of the experimental set-up, this indicates an additional AOA component of between 0.05° and 0.1° as a result of the refractivity along the link.

For ease of comparison, Figure 7.6 displays the relevant portion of the APM Model result from Figure 7.5 alongside the experimental results from Figure 7.1.

A period of particular note exists, from approximately 02:30 until 07:00 the AOA varies the most, a change which is matched in the experimental results by changes of a similar significance. This is further evidence that the experimental data has detected genuine AOA variations on the link and equally that the model is indeed modelling the physical environment.

Also of note is the period around 20:00 where the experimental link shows a change in AOA. In the model, the AOA appears to alter but this is more transient in nature than the more gradual change observed in the experimental data.

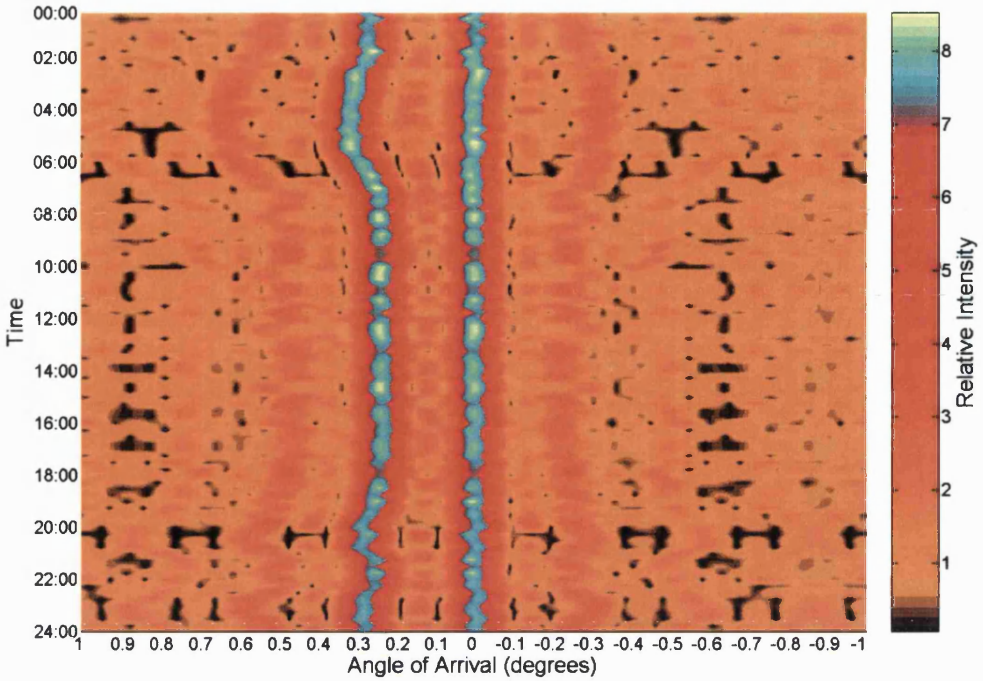

Figure 7.5: AOA surface plot, day 7

The model does indicate other greater angles with not completely insignificant signal contributions. It should be noted however that the antennas in the experimental link have low side lobes, some 30 dB below the main lobe. It is believed that the side lobes therefore do not affect the experimental AOA measurements as such a reduction in power places the side lobes in the noise (see Section 6.1) as far as the MMIC receivers are concerned. The model results could be improved in this respect by applying a window.

Worthy of note, in addition, are the times around 04:30-06:30 & 20:00-24:00 where there seems to be a degree of signal loss from some of the wider angles (shown in Figure 7.5) and of more significance, angles close to the dominant AOA. There is also a degree of signal enhancement to be noted in the dominant AOA during these periods. Clearly this indicates bean focusing as a result of the refractive index changes which are causing the dominant AOA to alter.

Overall, from the study of this single day, it appears that the experimental results and the theoretical ones taken from modelling techniques do indeed match. There are some deviations, particularly in terms of AOA though it should be remembered that in the modelling, the same refractivity profile is assumed to be present along the entire link, the experimental results are the result of numerous (arguably infinite) refractivity profiles interacting with the signal over the length of the link.

Analysis of the remainder of this period did not reveal any further points of significant interest, that is to say that in each case, either similar patterns were found or the refractivity profile did not lead to ducting. Two days within the period unfortunately did not have associated MM5 data available.

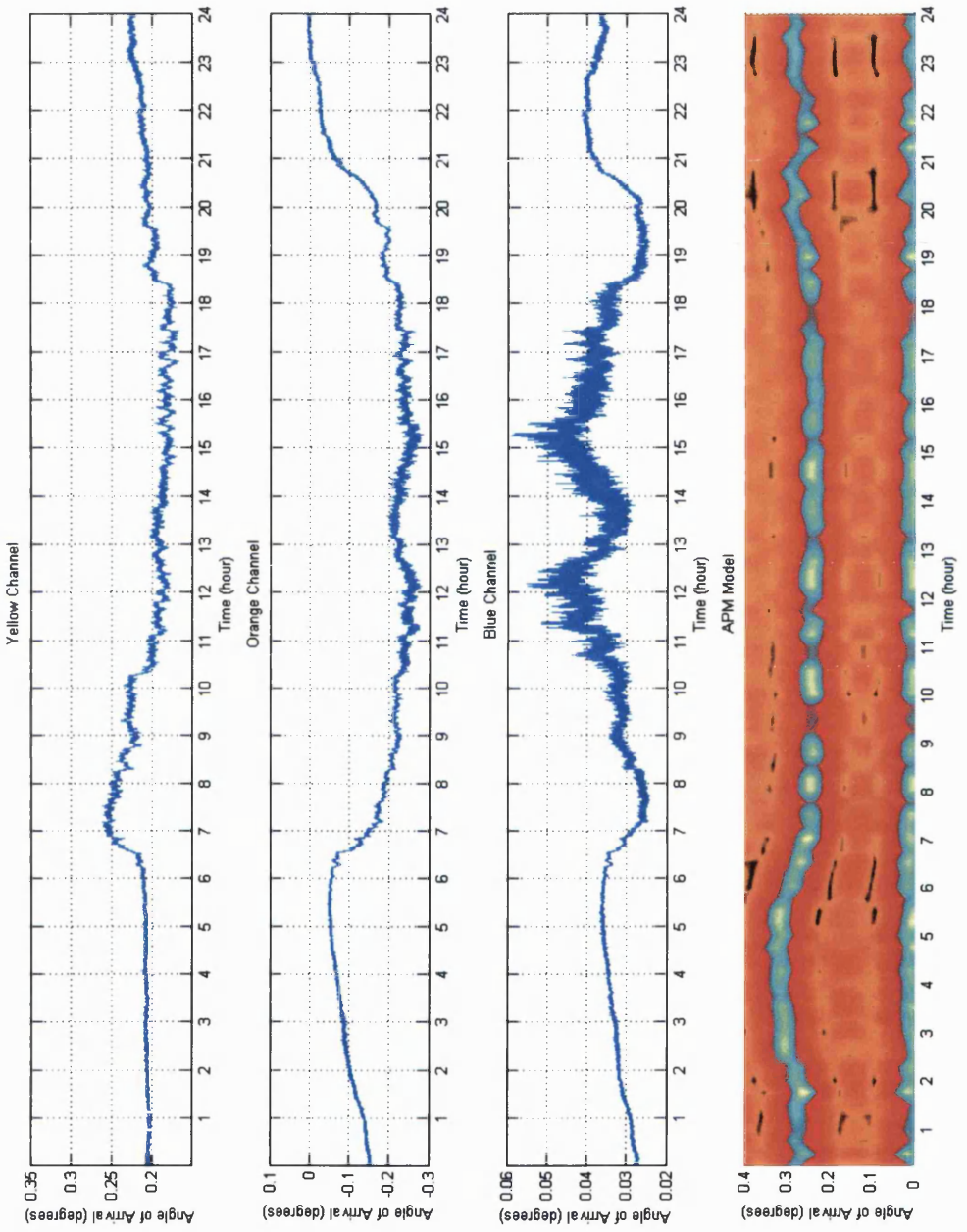

Figure 7.6: Measured AOA difference plots with modelled AOA surface plot, day 7

7.4 Period 2 Analysis

This week long period in the first half of July was dry with no rain being recorded by the weather station and only a few minutes of rain at the very start of day 1 from the MM5 model. The weather statistics for this period are given in Table 7.3.

Table 7.3: Period 2 Weather Statistics

	Period	Daytime	Night-time
Max	30.9 °C	30.9 °C	28.3 °C
Min	10.1 °C	10.1 °C	10.1 °C
Avg	20.2 °C	22.2 °C	18.1 °C

Using the same initial visual analysis technique as for Period 1, periods of apparent significant activity on the refractivity given by MM5 can be identified on the last three days of this analysis period.

Day 5, from the perspective of the phase difference plots, appears fairly typical of days in this period. There are a couple of notable points though, firstly, around 05:00 there is a period of change both in phase angle and noise. Similar events occur and 22:15 and 23:30.

The refractivity plots (Figure 7.7) show very little activity in the first 6 hours. At 06:20 a small inflection in the refractivity appears at around 250 m, which peaks at 06:30 whereupon it weakens and rises as the sun begins to heat the ground. Whether this is connected to the 05:30 event on the phase plots is difficult to say though it is possible that the APM has modelled the event timing slightly incorrectly.

The refractivity shows the lower 50 m or so alter gradient as 19:00 is reached, corresponding to the beginning of the AOA reduction seen on the phase difference plots. A slight additional change in refractivity gradient occurs shortly after 22:00 which may be linked to the later events noted on the phase difference plots.

Day 6 has significant disturbances present on the interferometer phase difference plots. The coincident MM5 data indicates corresponding anomalous

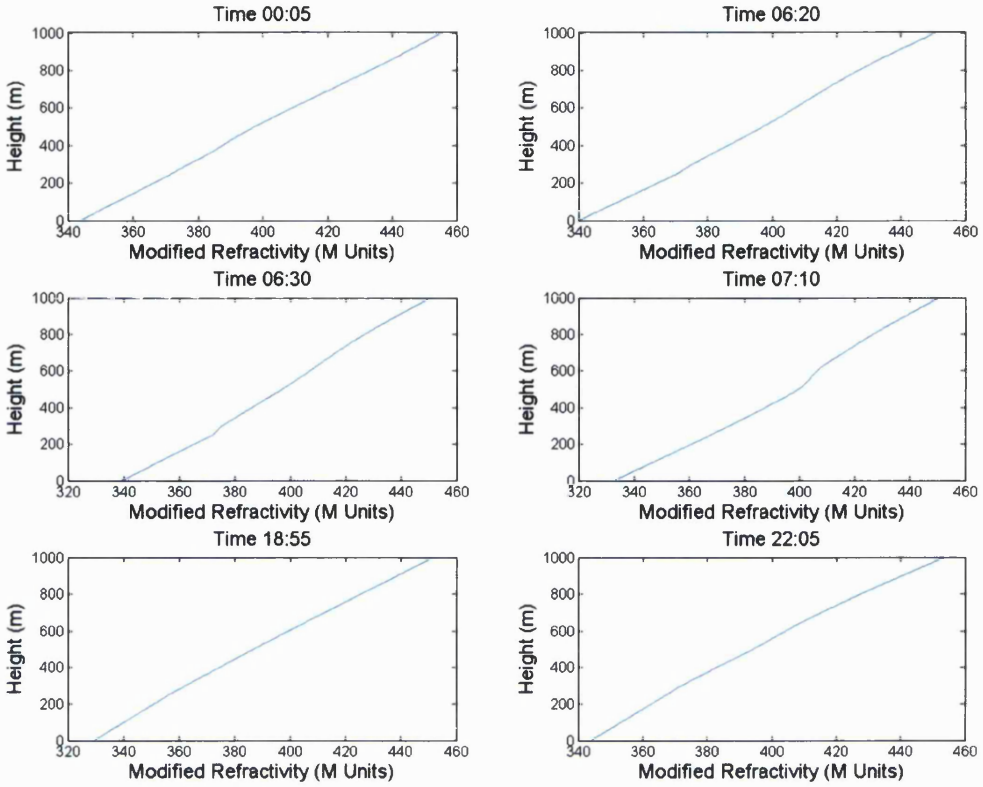

Figure 7.7: Key refractivity profiles from day 5

refractivity activity for these events. The MM5 refractivity indicates that the day begins with two distinct refractivity gradients within the first kilometre of the troposphere. This situation varies in significance until 02:05 when an inversion almost develops, see Figure 7.8. This inversion degrades but another develops at 02:45. This too fails to develop into an inversion though it persists for longer, until 03:30 in fact. At 06:35, an inversion briefly forms before decaying and then ascending.

The profile settles and remains almost completely benign throughout the day and only begins to alter towards late evening, even then nothing significant develops.

The APM (Figure 7.9) shows changes in the electric field with field enhancement and reduction conditions for the direct path occurring at 01:30

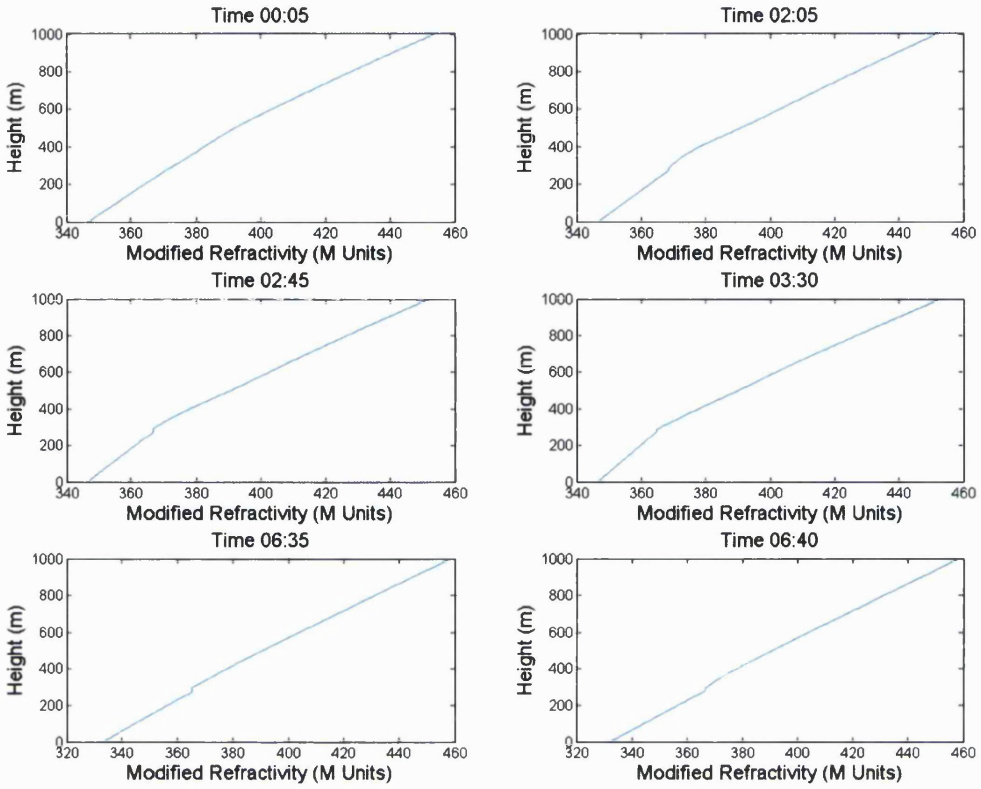

Figure 7.8: Key refractivity profiles from day 6

and during the period 02:00 - 06:45. At 01:30, there is an enhancement in field strength however, from 02:00 until 04:00 there is a severe reduction. This reduces by 04:30 before reappearing at 06:30, followed by a significant enhancement at 06:45. The phase difference plots do on this occasion indicate an effect.

A similarly severe reduction in direct path field strength occurs shortly after 06:00, lasting for almost an hour. The APM indicates that this is followed by a brief enhancement before the field settles. The phase difference plots however indicate a much longer effect with the phase difference not recovering for a further hour and a quarter.

In summary, the refractivity fluctuations present on this day brought about a number of AOA changes during the first 8 hours. These resulted

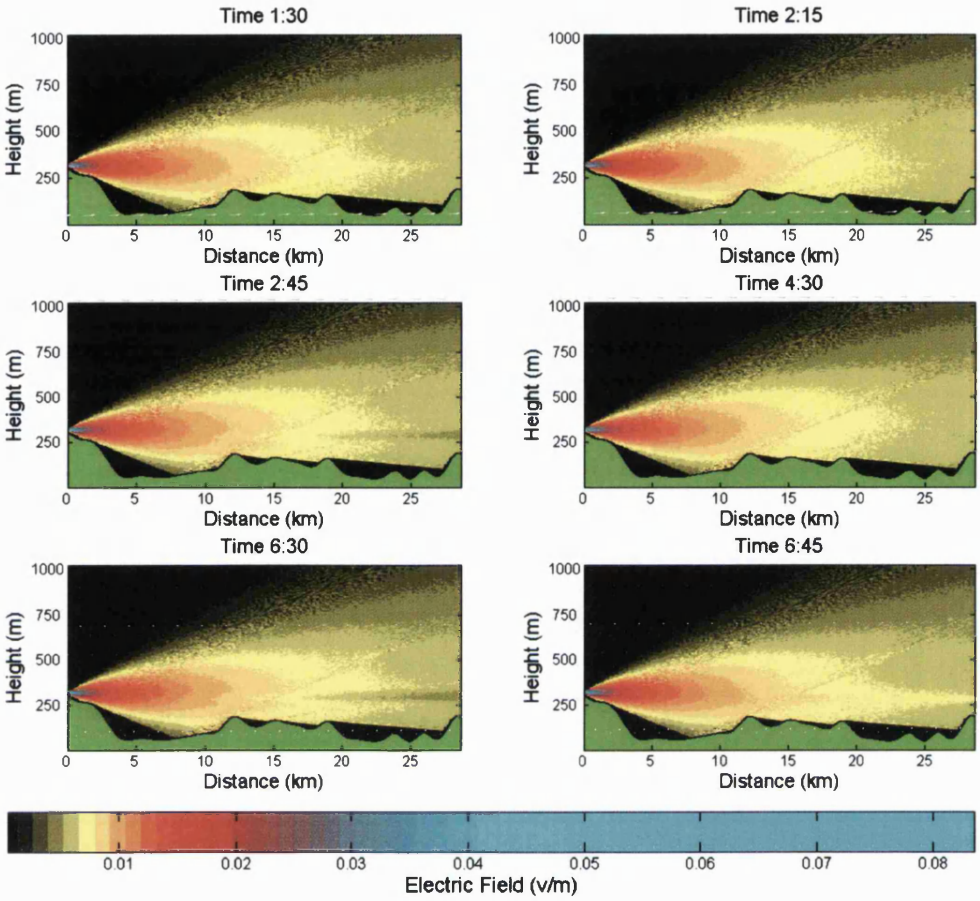

Figure 7.9: Key APM frames from day 6

from a couple of near inversions which vanished once the heat of the sun warmed the land underneath the transmission path. The remainder of the day followed what appears to be a common pattern for warm dry days, that of a flat topped smooth curve of AOA.

The final day of this period, from visual inspection, appears to be a candidate for significant refractive index events.

Producing the refractive movie file (see Figure 7.10 for key frames) for this day reveals the beginnings of an inversion at just over 400 m at 00:05. This lingers, altering strength until it very rapidly develops leading up to

06:00 and ascends during the course of the next two hours, weakening as it does so.

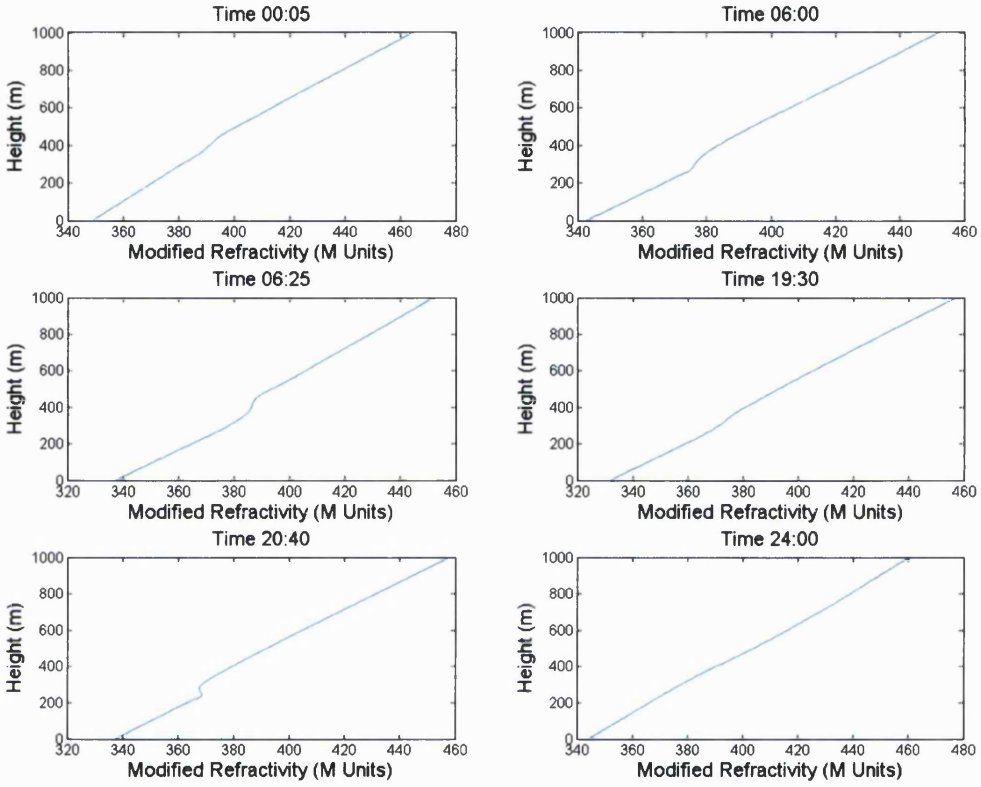

Figure 7.10: Key refractivity profiles from day 7

The phase difference plots indicate an essentially constant phase difference until around 06:00, matching the MM5 prediction.

The bulk of the day is uneventful with respect to refractivity though the measured data shows the AOA ramping up to and down from a static angle which is maintained for much of this time. From 19:30 the refractivity profile shows the development of what turns out to be a sharp inversion, the thickness of which is only approximately 40 m at 20:15. This does not appear to have any marked effect on the measured phase difference plots though they do indicate a significantly more rapid reduction in phase difference, compared to the change in the morning.

The APM electric field plots show a few interesting events. Firstly in the 05:15 plot, the model shows a marked drop in field strength with areas of increased field strength either side. This is followed by an extension of one of these stronger regions. These events in the electric field do not translate into significant events in the measured data. One explanation would be that this type of event would lead to a reduction in received signal strength but not necessarily an alteration in AOA and that would certainly appear to be the case here. The raw data from the interferometer indicates a short lived dip in signal strength at around 05:00 lasting for approximately 20 mins. This reduction in signal strength is not however large compared to other fluctuations during the day.

The day time is clearly defined in this movie by stability in the electric field strength, lasting until 18:15 which is when the measured data begins its reduction in angle. The APM then shows another field reduction event centred on 20:45 and which is all but absent at 22:00.

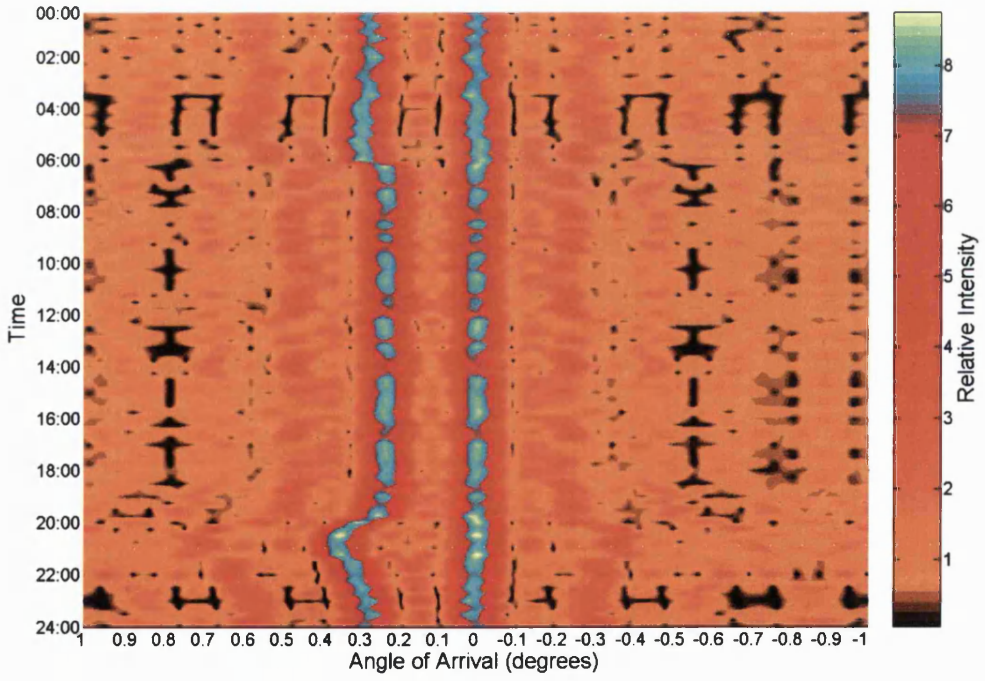

Figure 7.11: AOA surface plot, day 7

The AOA surface plot (Figure 7.11) indicates two periods of larger AOA, the first leads up to a fairly sudden change at approximately 06:30 with the maximum AOA of 0.35° at 03:30. An opposite change of a similar magnitude but more gradual is noted around 20:00.

7.5 Period 3 Analysis

Period 3 is a 9 day period in July. This period contains two days which were affected by precipitation. These two days therefore offer the first look so far at how the link performs during precipitation. From the link budget and given the effects of precipitation on radio frequencies calculated from [20], an outage is anticipated with pervasive rainfall rates exceeding $3.4\,\mathrm{mmh}^{-1}$. There simply is not enough power to overcome the attenuation introduced by rain, particularly when that rain affects a significant portion of the link. One important factor to consider throughout the analysis of days affected by precipitation is that precipitation may be present along the entire link or perhaps only a proportion of it. Clearly if only a small proportion of the link is affected by rain, there is a chance that the signal to noise ratio will remain sufficiently high to maintain the link integrity. If this occurs then the phase difference plots should indicate the effect rain has on AOA. More intense or pervasive rain events will simply attenuate the signal to a level where the interferometer cannot function and the data from it will be insignificant.

Plotting the MM5 rain data for this period reveals several pervasive rain events with a number of short lived rain events which cover only a proportion of the link.

The weather statistics for the period are given in Figure 7.4.

Table 7.4: Period 3 Weather Statistics

	Period	Daytime	Night-time
Max	$25.6\,°C$	$25.6\,°C$	$23.9\,°C$
Min	$12.0\,°C$	$12.0\,°C$	$12.4\,°C$
Avg	$16.7\,°C$	$17.6\,°C$	$15.9\,°C$

From the analysis of Day 6, which had heavy and persistent rainfall, it is clear that the various sources of information support each other. The MM5 rainfall, plotted inversely above the received power for one of the interferometer vertical pairings (Figure 7.12) indicates that the periods of attenuation occur in line with the peak rainfalls.

The rainfall (see Figure 7.13) initially covers the entire link length with moderate to heavy rain, causing severe attenuation to the point where the link fails and remains in an outage condition for over 2 hours. The later events are more limited in geographical scope however much more severe rain is experienced.

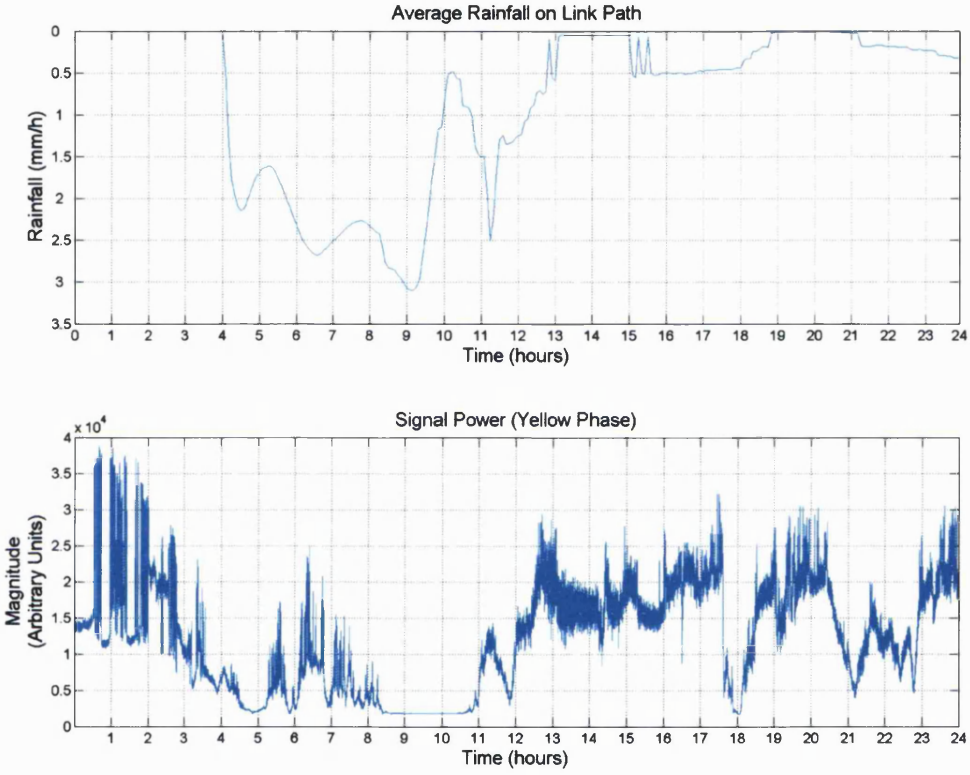

Figure 7.12: Rainfall and signal power (yellow phase) plots for day 6

Day 7 poses a few difficulties for analysis as the various information sources appear not to support each other. Firstly examining the measured data, there appear to be two significant events. The first is a marked drop in signal power shortly after 05:00 with associated mild alteration in phase differences. This recovers in a two step manner with an hour between steps. The second event occurs at 14:30 and appears to be comprised of two more in-

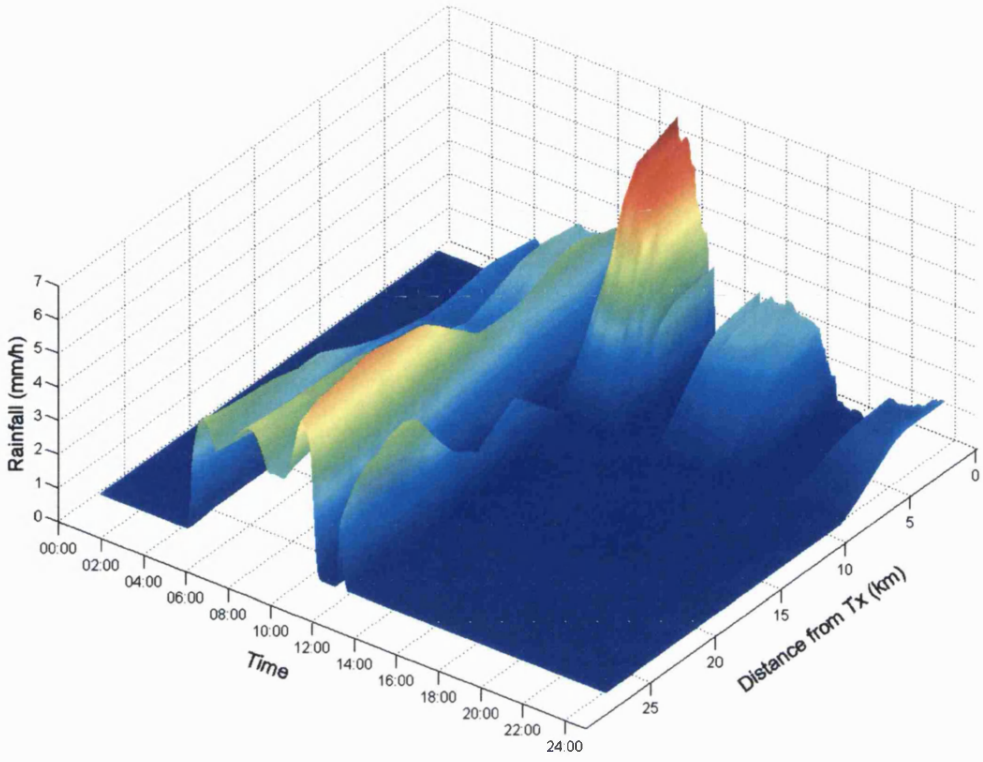

Figure 7.13: 3D surface plot for rainfall, day 6

tense periods with a brief, partial recovery between them. This second event appears to have greater effects on the phase whilst only mildly affecting the signal power, conversely for the earlier event.

The MM5 indicates rainfall over the first 7 hours with a local maxima shortly after 05:00. The 3D surface plot (Figure 7.14) of the MM5 rainfall indicates that the rain is concentrated at the transmitter location but increases in link coverage towards 05:00. The intensity decreases from the initial level however the increased link coverage would result in potentially greater attenuation and depolarisation.

The MM5 data does not show any rain events during this period. No conclusive picture can be derived from the surface weather station data though changes in both temperature and humidity indicate rapidly changing conditions in the afternoon. The event is therefore presumed to be convective

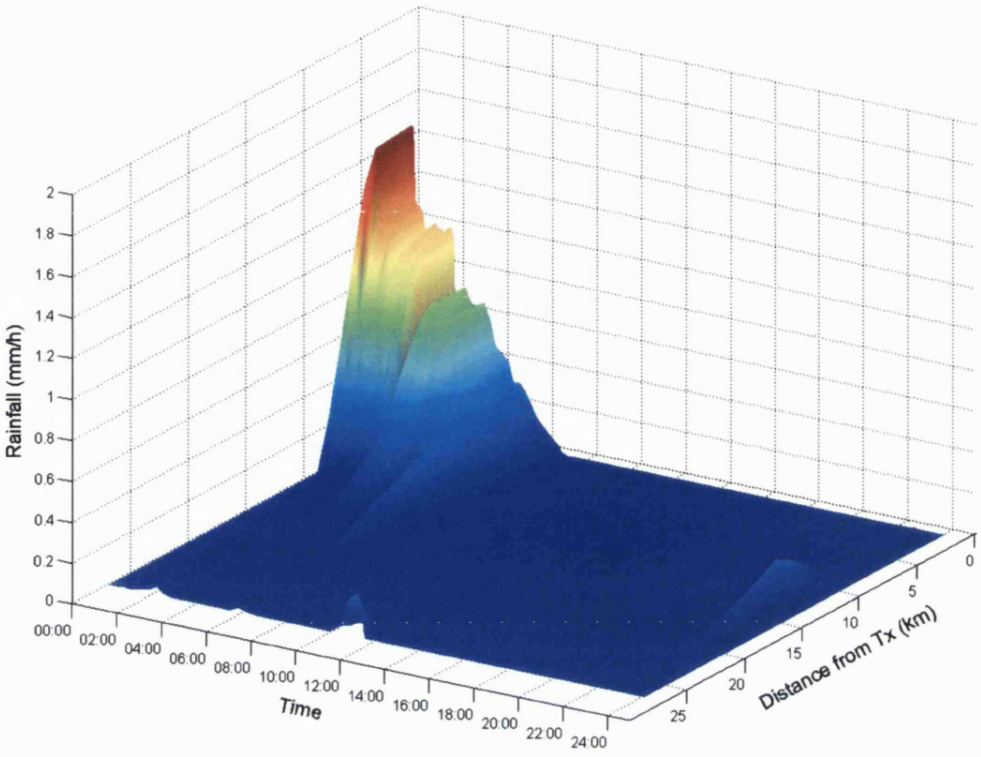

Figure 7.14: 3D surface plot for rainfall, day 7

rain, which the MM5 failed to predict.

Day 8 appears to buck the trend of well correlated data. This day suffers rain though the MM5 doesn't predict either the severity or the timing correctly. The recorded data indicates a fade shortly after 09:00 which does correlate to the Bristol weather station data, if shifted by 1 hour which is reasonable given the geographical separation of the link and weather station and a SE wind direction. The MM5 model indicates sustained rain from shortly after 17:00 (Figure 7.15) which varies in intensity, peaking at 19:15 occurring mid link with significantly less rainfall elsewhere. The recorded data however indicates that after the morning downpour, the signal levels don't begin to return to normal until 20:00. The conclusion is that the rain actually experienced was less severe but sustained, preventing the link from

returning to normal after the mid morning rain event. The reduction in rain fall from 20:00 onwards allowed the link to normalise.

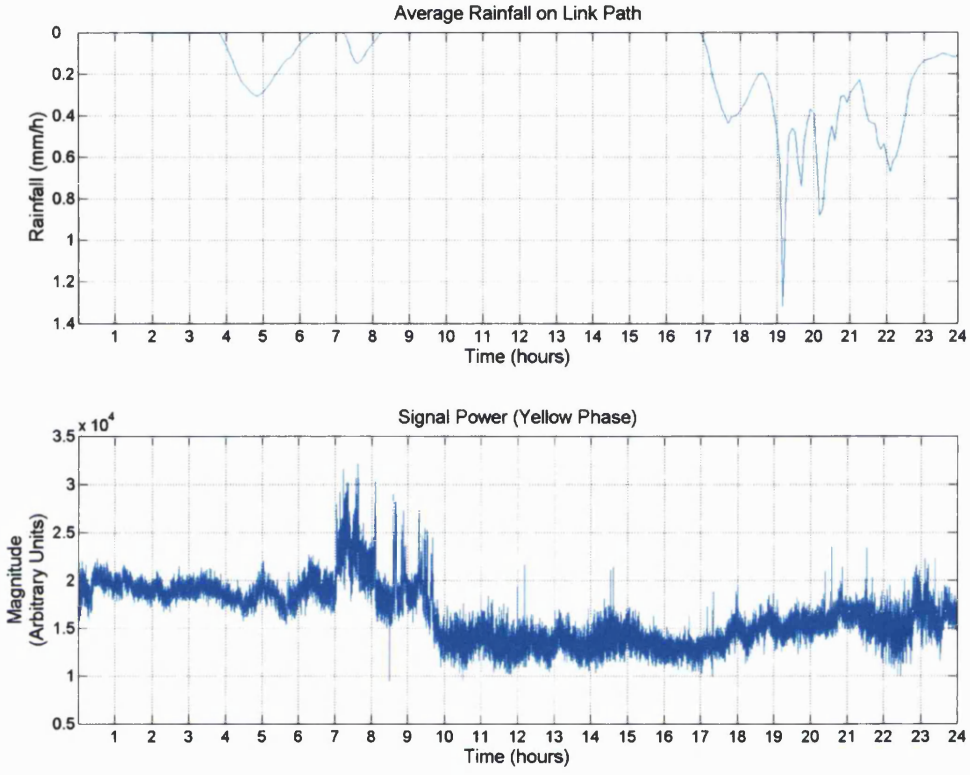

Figure 7.15: Rainfall and signal power (yellow phase) plots for day 8

The refractivity plots do indicate that there is a link between this and the initial slow change in phase seen over the first 6 hours however the plots indicate no significant AOA variation.

The last day in this period, day 9, suffered significant rain events. These lead to the link failing due to the signal attenuation. The interferometer did however remain operational for the vast majority of the day, capturing the signal degradation which lead up to and away from the outages themselves.

Plotting the MM5 average rain for the link path with an inverted y axis and the signal power for one phase (Figure 7.16), it is clear that there is a direct link between the two. There is a detectable time slip though it is only

slight and there are some effects present on the recorded data which don't have a corresponding event in the modelled rain. This discrepancy can be explained by the fact that small rain events are not well modelled by the MM5. Figure 7.16 displays a glitch very shortly before 9am, this is believed to be caused by an intermittent equipment fault with the reference MMIC.

From a surface plot of the MM5 rain data (Figure 7.17) over the link length it is clear that the centre of the link suffered different rainfall than the ends so this is a case in which the severe rain on one portion of the link does not affect the whole link and therefore does not cause the level of attenuation necessary to force the link into fade.

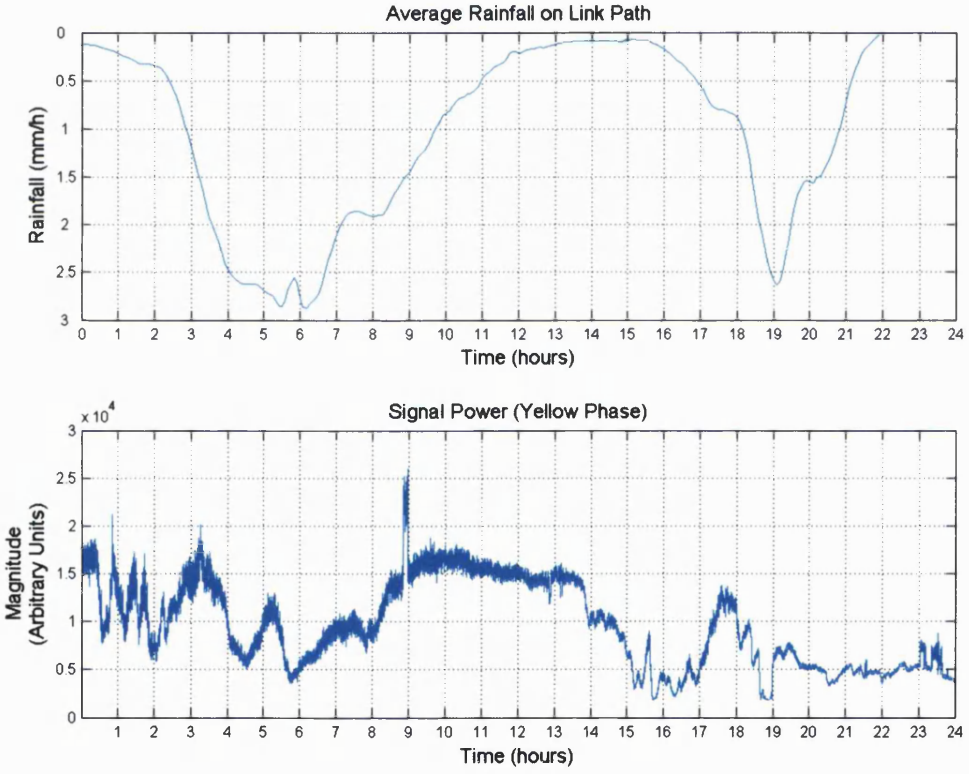

Figure 7.16: Rainfall and signal power (yellow phase) plots for day 9

The data from this last day of the period indicate that the interferometer works correctly right up until the point when the signal attenuation pre-

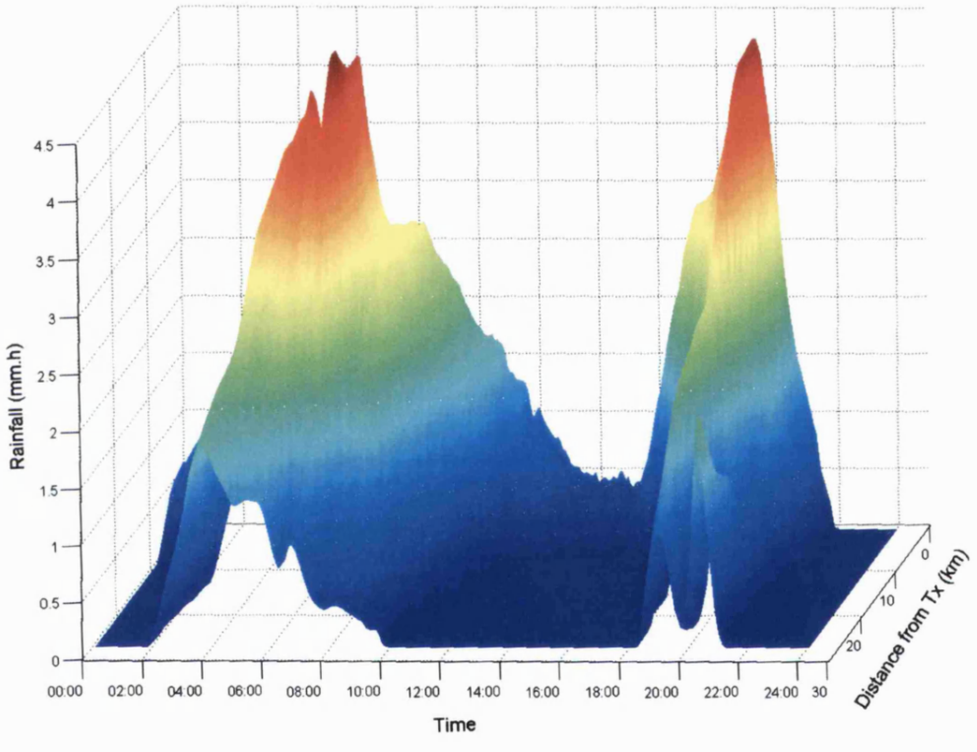

Figure 7.17: 3D surface plot of rainfall, day 9

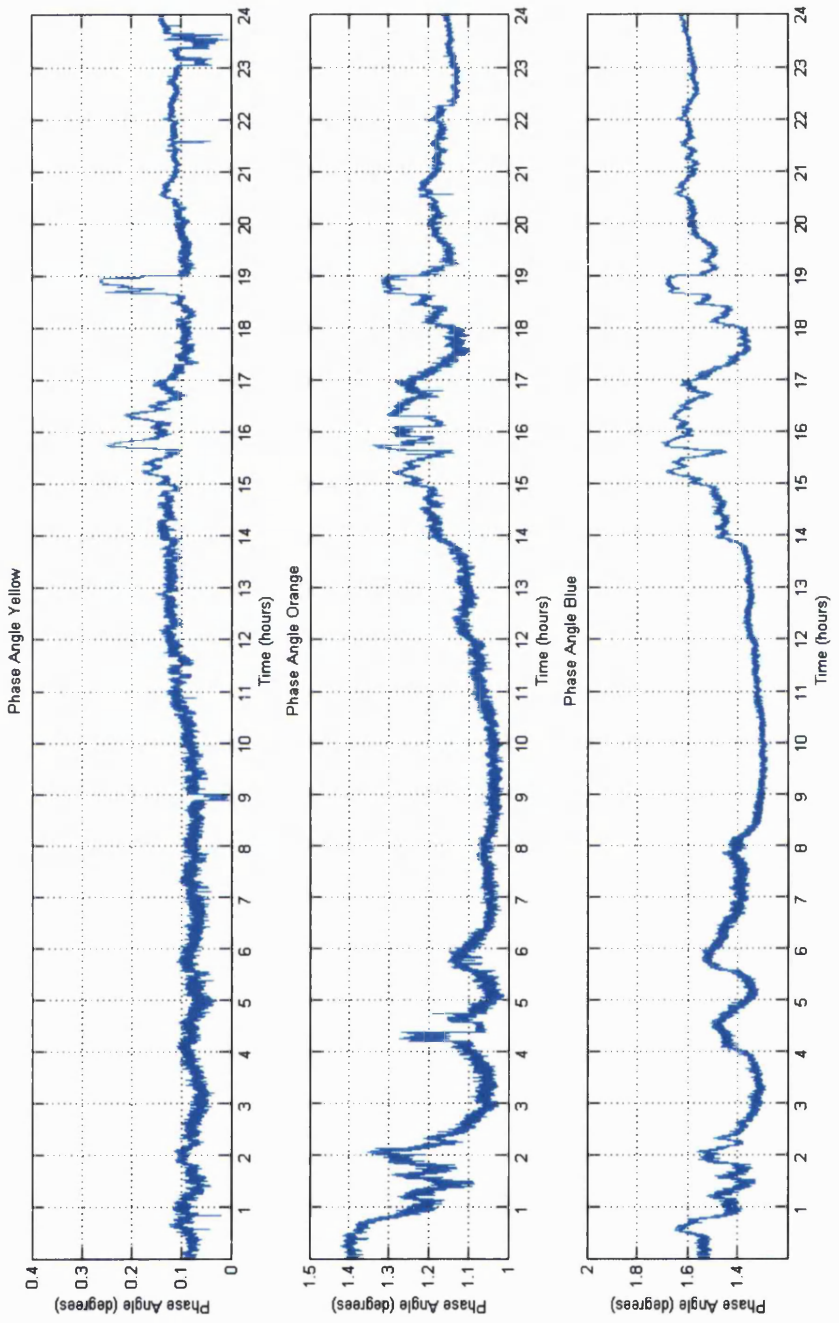

Figure 7.18: AOA difference plots, day 9

vents it from locking onto the source. The data therefore records the AOA measurement until this condition arises whereupon there is a jump in AOA. This jump is reversed when the signal returns. The remainder of the data, which is considered valid, shows very little variation over the day, see Figure 7.18. Certainly there is no arch trend as was seen with the warm dry days in periods 1 & 2. This further confirms that the equipment is relatively temperature insensitive. There is an increase in measured AOA over the period of the most severe attenuation indicating that there is an effect on the AOA caused by rainfall. The phase difference plots for the three colour coded receiver pairs (see Section 7.2) also indicate that the effect might be more severe horizontally than vertically.

Theory tells us that during heavy rain, drops approximate oblate spheroids rather than the spheres formed by small drops. These oblate spheroids attenuate horizontally polarised waves to a greater degree than vertically polarised waves. This link uses a circularly polarised wave which can be considered to be affected equally in both ways by the drops. If the rain is heavy then there should be a greater level of attenuation horizontally than vertically. The two mechanisms are absorption and scattering. A phase difference comprising both horizontal and vertical components would experience greater changes in received intensity than one which was based on a vertical spacing alone. More importantly there would be increased scattering in the horizontal plane. This appears to be borne out in the interferometer data. The phase changes associated with the heavier rain event of the day cause a greater AOA change on the diagonally spaced phase difference compared to the two vertically spaced ones. Further, this change is significantly greater than those associated with the earlier, less heavy rain events though these too indicate a slightly larger effect than the other phase difference plots.

The conclusion has to be therefore that heavy rain, due to the oblate spheroid approximation, causes an AOA change, both horizontally and vertically though the effect appears to be more significant in the horizontal plane.

Examining the MM5 refractivity for the day shows that changes do occur in the modelled environment though these aren't easily seen from some

analysis methods. The APM activity (Figure 7.19) shows gradual changes in AOA which correlate well with the experimental data (see Figure 7.20). Also worthy of note are the gaps which indicate that some beam focusing does occur during the rain events in addition to the AOA changes.

The effects do however appear to be smaller in magnitude than those seen in previous periods for clear air cases. It can also be seen, particularly in the experimental data that there is more variance in the measurements during the rain periods indicating rapidly varying propagation conditions.

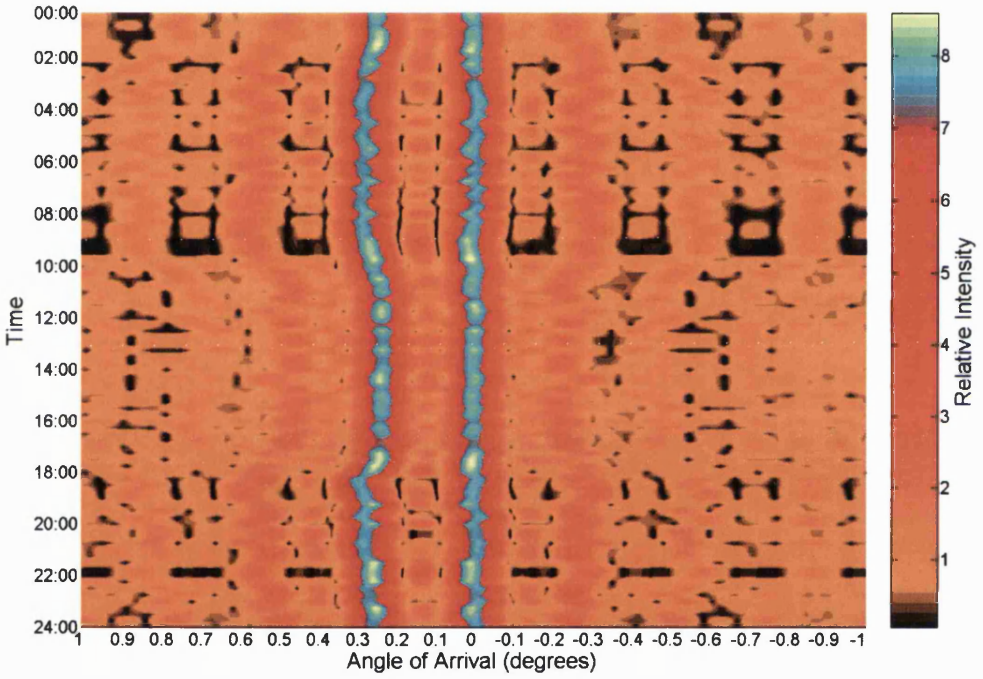

Figure 7.19: AOA surface plot, day 9

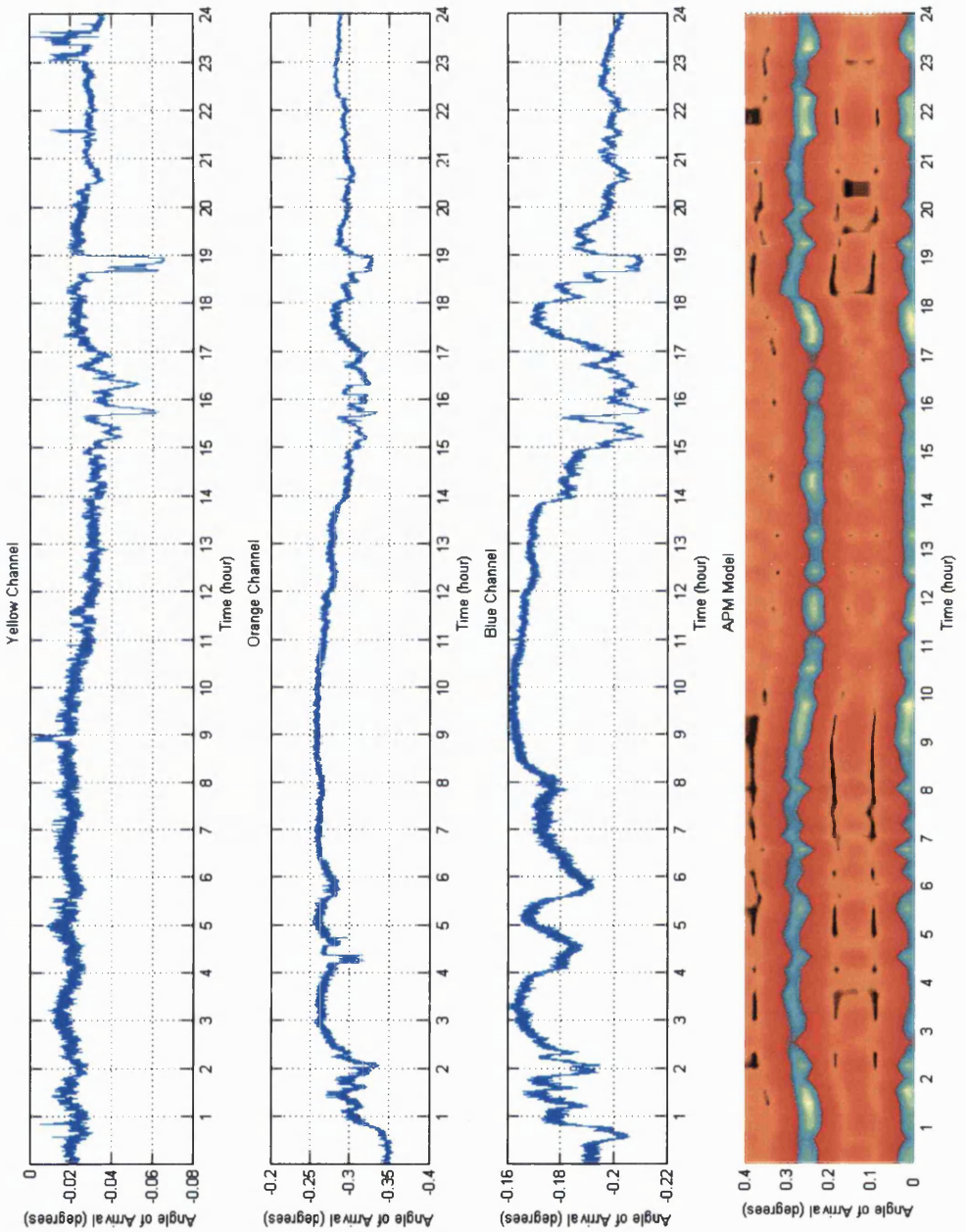

Figure 7.20: Measured AOA difference plots with modelled AOA surface plot, day 9

7.6 Period 4 Analysis

This period, covering slightly more than two weeks at the beginning of September 2005 saw only two significant rain events. Days 6 and 10 saw severe but short lived rainfall with varying link coverage. The MM5 model indicates tiny ($< 0.1\,\mathrm{mmh}^{-1}$) quantities of rain on other occasions though these do not amount to anything significant in their own right.

The general weather statistics for this period are given in Table 7.5.

Table 7.5: Period 4 Weather Statistics

	Period	Daytime	Night-time
Max	$25.4\,°C$	$25.4\,°C$	$23.4\,°C$
Min	$3.9\,°C$	$3.9\,°C$	$4.1\,°C$
Avg	$16.1\,°C$	$17.5\,°C$	$14.6\,°C$

The period is predominantly dry though days 5, 6 and 10 are affected by significant rain events. The MM5 model refractivity plots indicate that in contrast to period 3, the refractivity is not static, even on days with rain events.

Day 1 begins with an inversion which persists until 03:35 (Figure 7.21), this subsides thereafter giving way to a broadly stable profile featuring a slight inflection near the ground. Around 18:00 a sharp inversion begins to form which lasts until 20:10. This and the earlier inversion do not appear to result in significant changes in the phase measured by the interferometer. The familiar arch is seen with the phase changing as the inversion layer mixes and rises due to the heating effect of the sun. The 18:00 inversion initiates the decline in phase difference. Figure 7.22 shows quite significant AOA changes over the course of the day. The inversion noted in the early hours corresponds with an arch of AOA followed by a period of steady but large AOA. This reduces shortly after 08:00 to an AOA slightly more than the geometric AOA before gradually increasing throughout the remainder of the day. Similar trends are noted in the experimental data however the magnitude of the changes are not replicated.

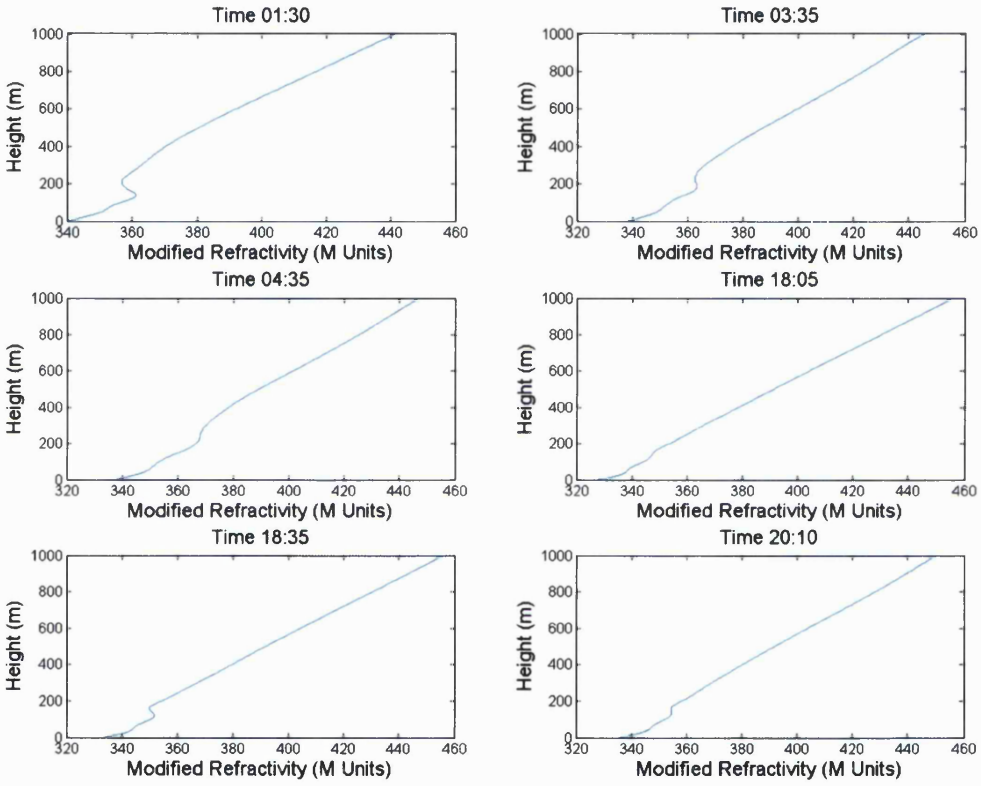

Figure 7.21: Key refactivity profile from day 1

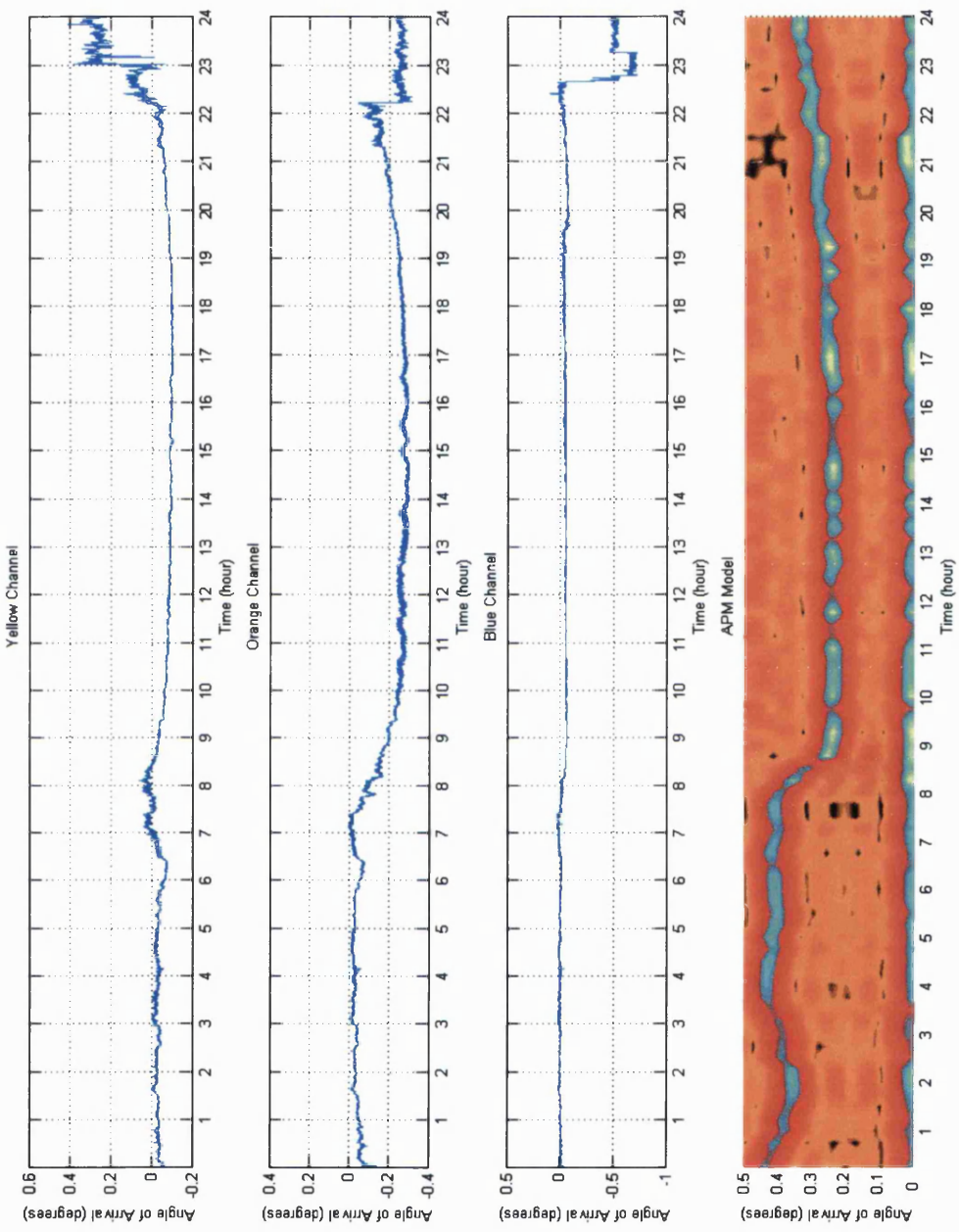

Figure 7.22: Measured AOA difference plots with modelled AOA surface plot, day 1

Day 2 shows nothing out of the ordinary. Day 3 however indicates a slightly more active refractivity profile. The normal trend persists throughout the small hours and then as the sun rises, the phase difference measurements show an increase (Figure 7.23). Around 09:00 the change ceases with little change noted until shortly before 10:00 when a further increase is seen. This sharp increase stops shortly after 10:00. The refractivity plots (Figure 7.24) indicate that this is a period of quite uniform refractivity though that contrasts with the previous period where inflections feature.

While this event is not completely explained by the refractivity, an event around 19:00 appears to be. One of the phase plots indicates a rise in phase difference, peaking at 19:00. The refractivity plots indicate the formation of two inflections, one of which descends, beginning at 18:30. The event trails off steadily as the evening and night progress. This appears to be consistent with the refractivity plots which indicate a similarly gentle trail off in the severity of the inflections. The APM images indicate a strengthening of the field between 19:00 and 21:00. Plotting the AOA obtained from the APM alongside the experimental results (Figure 7.25)once again demonstrates a good correlation between the modelled and measured results. This also reveals a period around 13:00-14:00 where the model indicates a weakened signal which is matched by quiet periods in the experimental data. This is not apparent from the propagation images nor the refractivity profiles and the amount of signal attenuation does not appear to be excessive.

Day 10 suffered fairly persistent rain events, predominating the day. The measured data indicates a number of periods where the rainfall causes attenuation severe enough to prevent the link remaining operational. The MM5 model rainfall does not correlate perfectly though it does indicate the general trend. The prolonged rainfall predicted by the MM5 model appears to have affected the link in three heavy periods of rain while the larger and short lived event the MM5 model indicated appears to have occurred slightly later than anticipated.

The 3D rain plot (Figure 7.26) indicates the MM5 model rainfall prediction in more detail.

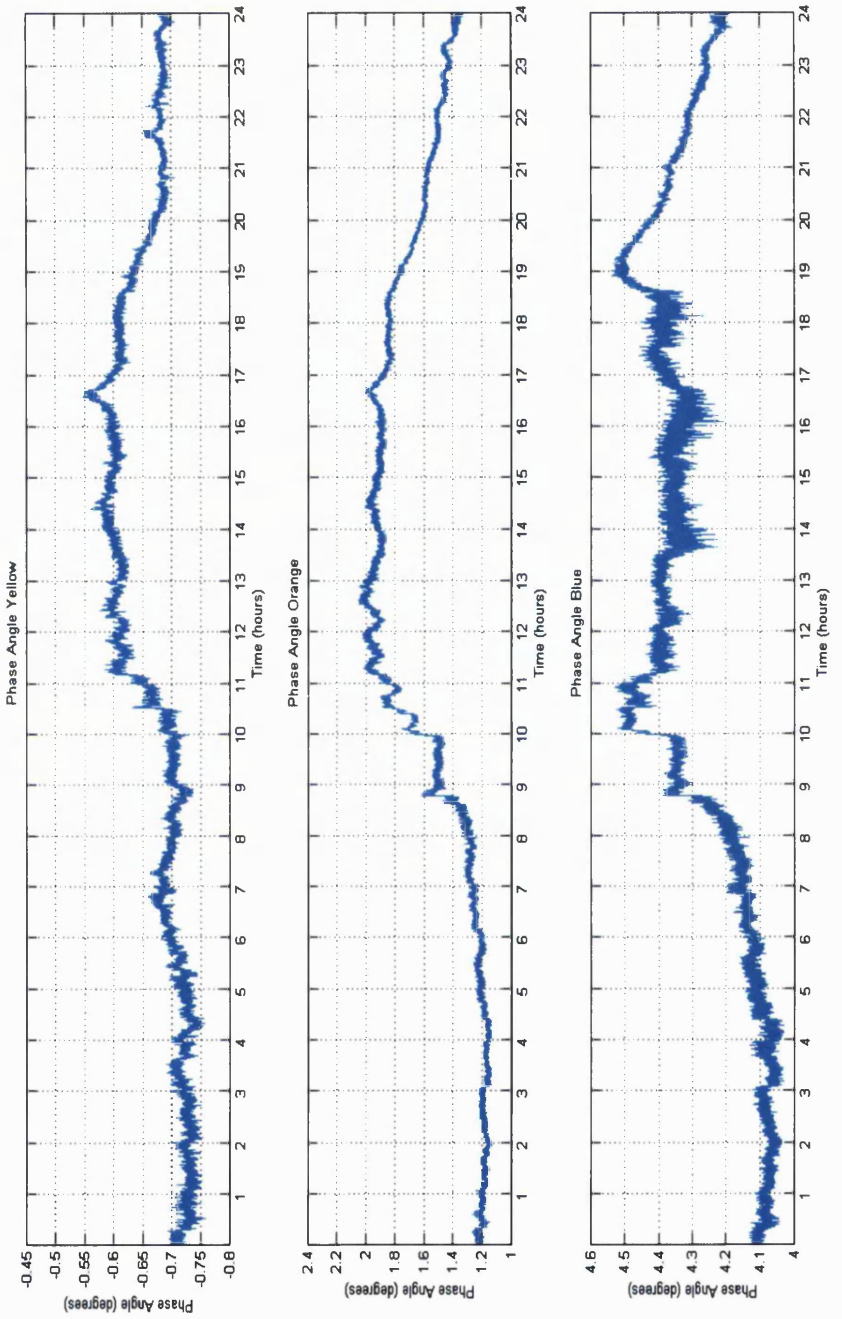

Figure 7.23: AOA difference plots, day 3

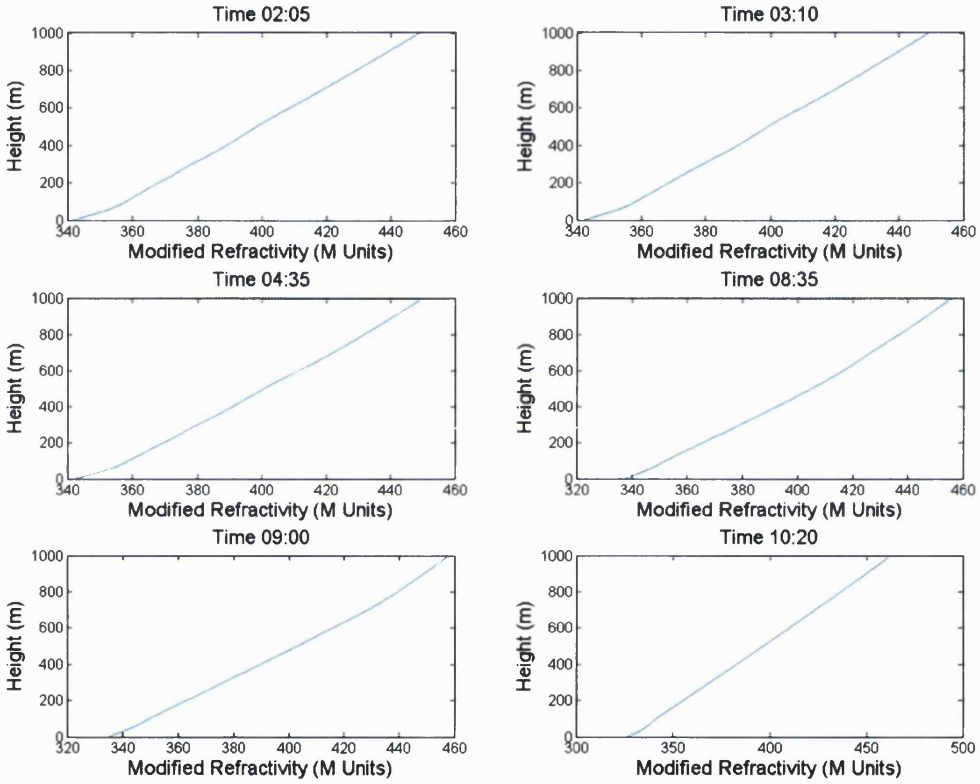

Figure 7.24: Key refactivity profile from day 3

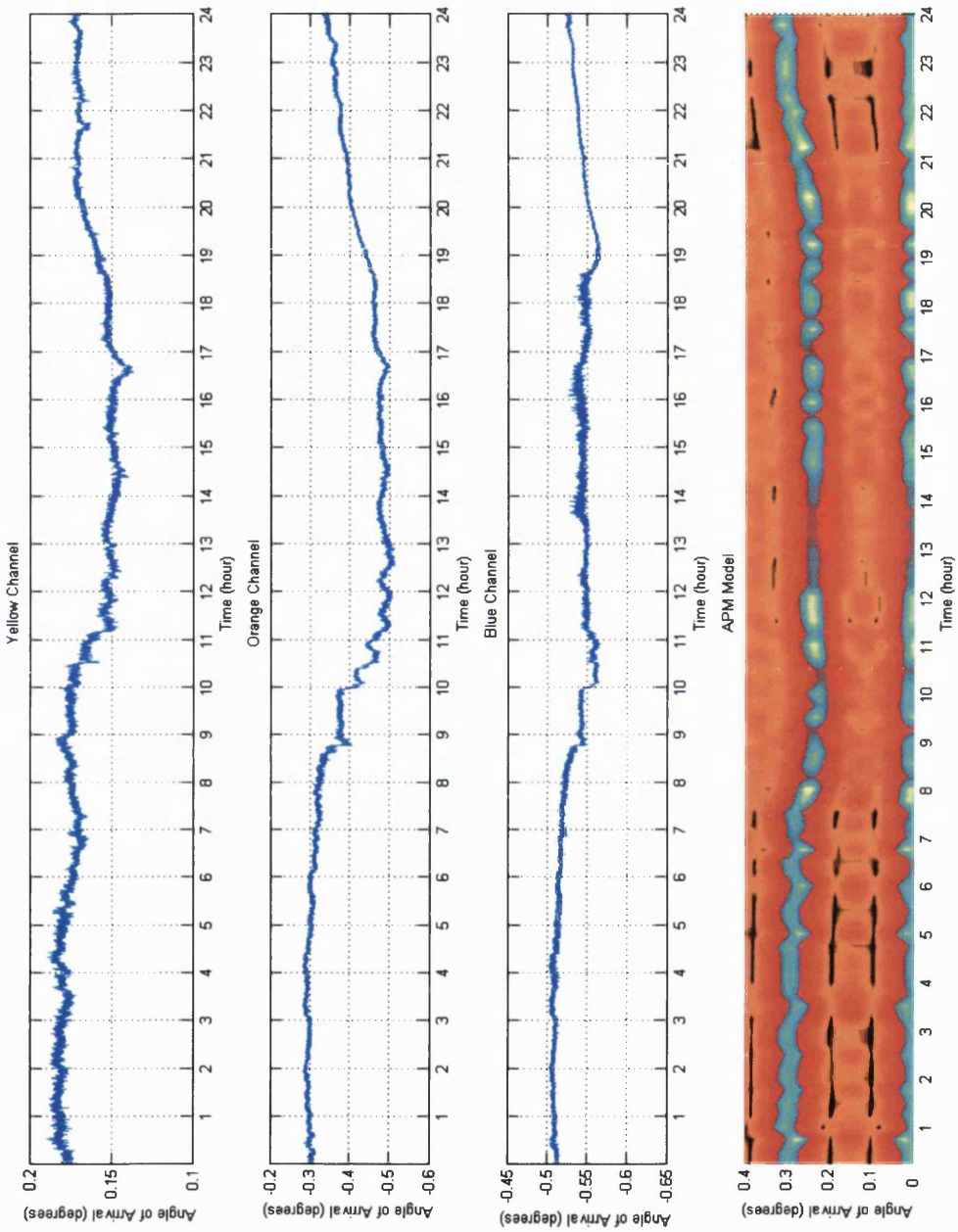

Figure 7.25: Measured AOA difference plots with modelled AOA surface plot, day 3

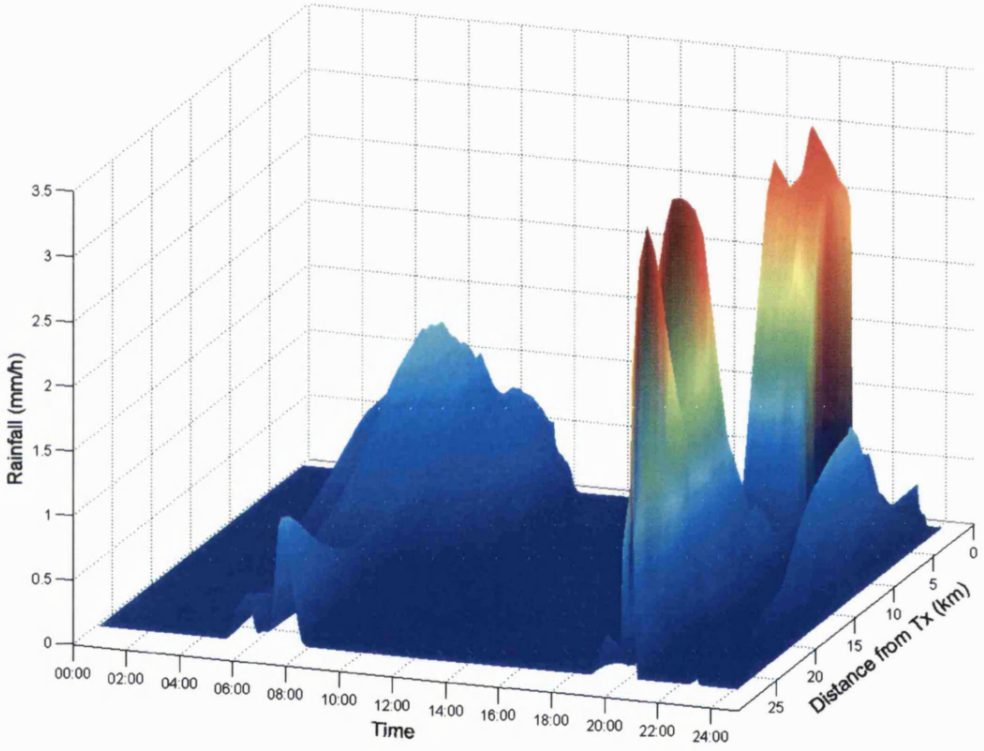

Figure 7.26: 3D surface plot for rainfall, day 10

7.7 Period 5 Analysis

This period, firmly in the winter season features lower temperatures than previous selected periods (Table 7.6). The period includes a significant snow shower which presents an opportunity to examine how such a weather event affects the link. Unfortunately such events are less common than rain and can therefore not be explored in as much detail.

Table 7.6: Period 5 Weather Statistics

	Period	Daytime	Night-time
Max	$11.8\,°C$	$11.8\,°C$	$10.1\,°C$
Min	$-0.6\,°C$	$-0.6\,°C$	$-0.3\,°C$
Avg	$6.1\,°C$	$3.3\,°C$	$2.8\,°C$

As would be expected, the refractivity profile during snow events is stable and benign. The AOA appears to be unaffected as can be seen from Figures 7.27 and 7.28 which show a quiet picture. This can be expected since snowflakes tend to scatter, due to their ice content, and the moisture content of the air is low, translating into very little bending.

Several snow periods were detected during this period, often in the early hours. The data from a disdrometer was used to pin point the snow events. This device was located directly underneath the link path a short distance in front of the receiver array.

This data allowed the analysis to exclude rain events which did accompany several periods of snow. The associated attenuation of both the rain and snow can be seen from the raw data plots (see Figure 7.29) however the phase angles are only affected by the onset of rain. This can be seen by examining Figure 7.30.

Summary

This chapter has examined, in detail, a number of periods throughout the experimental campaign. These periods have been chosen so as to feature as

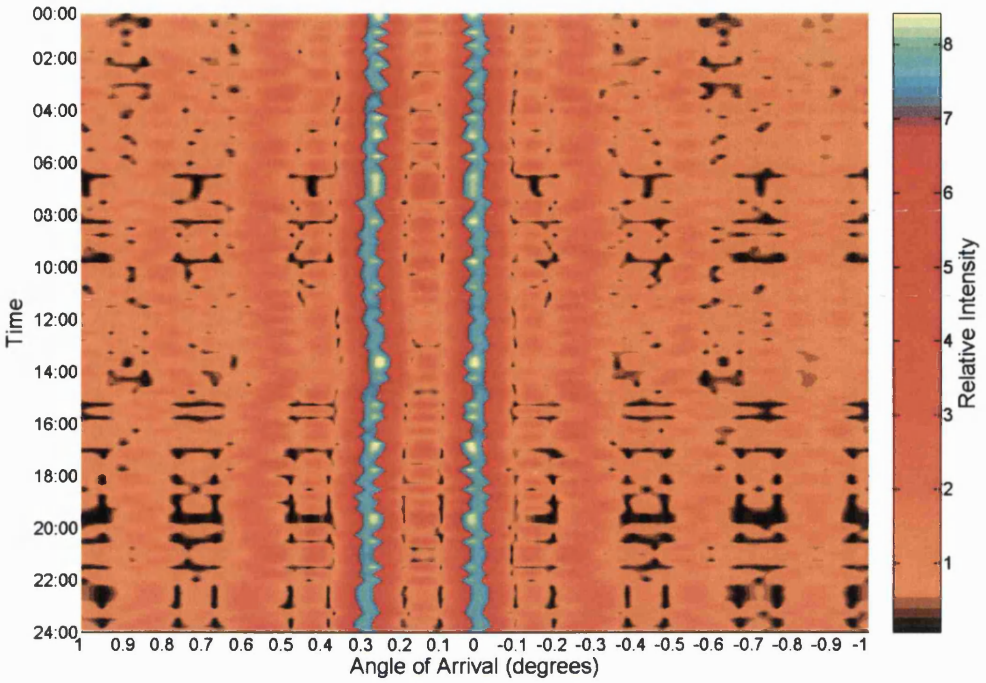

Figure 7.27: AOA surface plot, day 8

wide a range of weather conditions as possible. The analysis has shown that despite this diverse set of conditions, the AOA effects have been muted.

This chapter has, through its examination of the last period which featured snow, confirmed the theory presented in Chapter 2 in relation to the way in which snow affects radio propagation.

The analysis has shown how the various sources of information, available during the study and detailed in previous chapters, have been drawn together. Of particular importance is the relationship between the theoretical and practical results and how they concur, and on occasion there are differences. The broad agreement between the theory and experimental results lends weight to the conclusions which are presented in the next chapter.

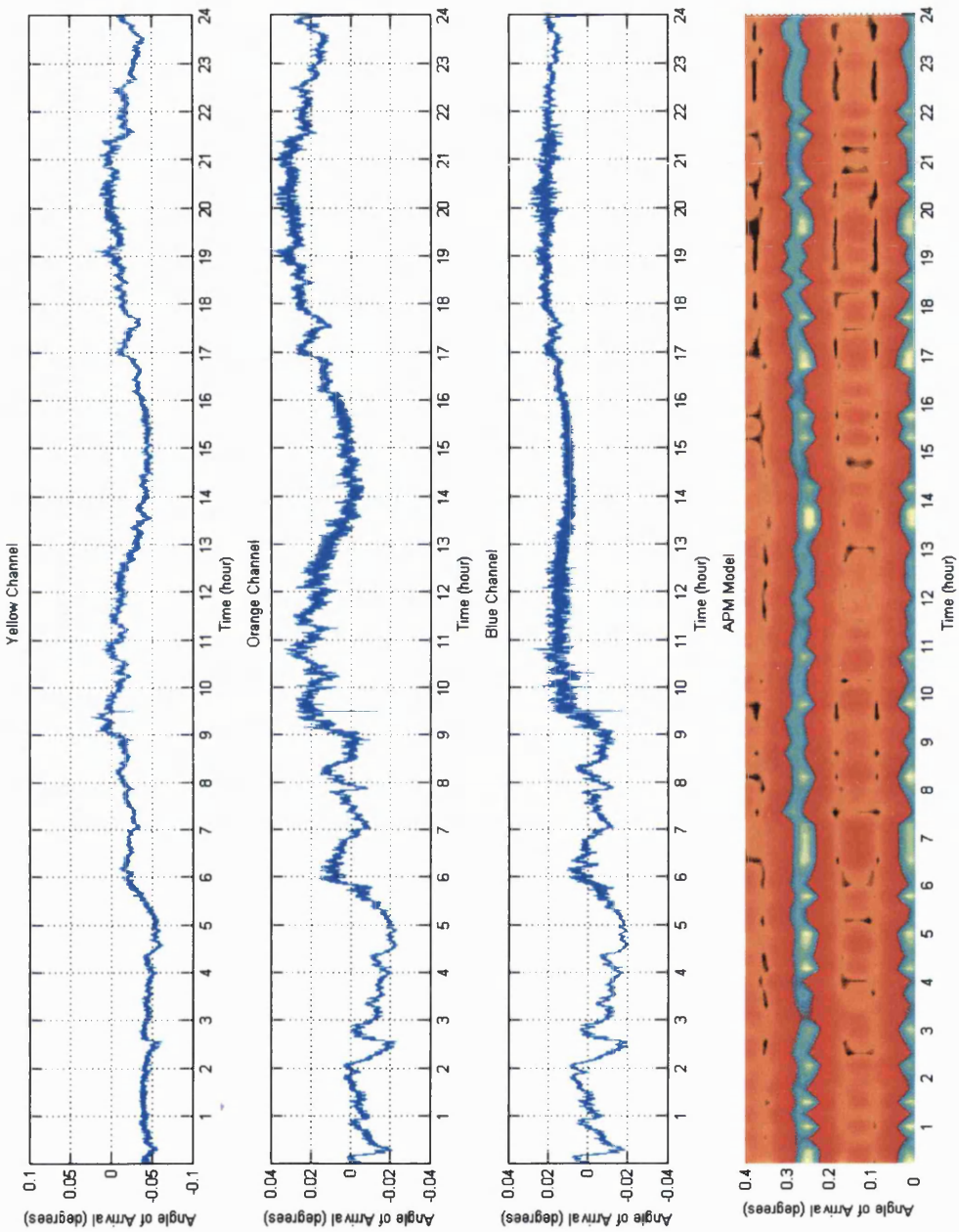

Figure 7.28: Measured AOA difference plots with modelled AOA surface plot, day 8

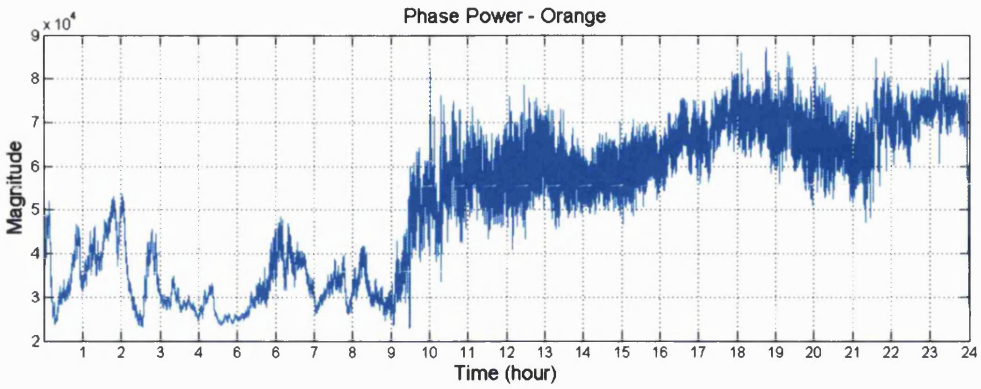

Figure 7.29: Phase power (Orange phase), day 8

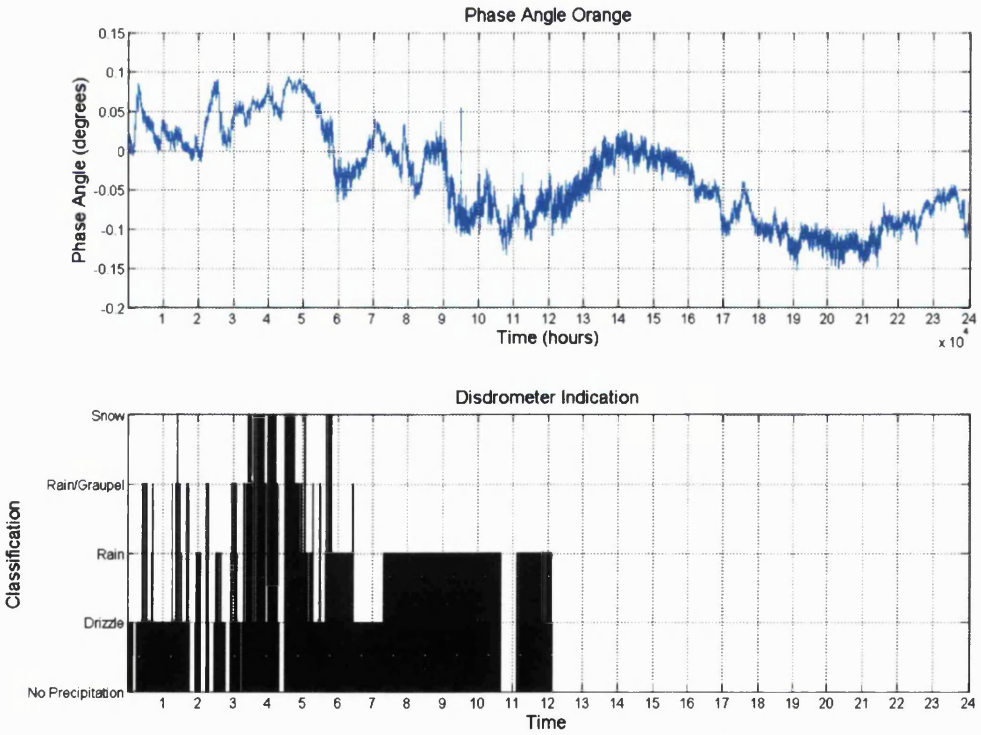

Figure 7.30: Phase difference (Orange phase) with disdrometer precipitation indication, day 8

Chapter 8

Conclusions and Further Work

This thesis has examined, in Chapter 2, the theory surrounding radio wave propagation through the troposphere. Included in this examination were the topics of turbulence, scintillation, refractivity, precipitation and interferometry.

A number of techniques for modelling tropospheric radio propagation were then examined in Chapter 3. The Parabolic Equation (PE) was introduced together with its basic derivation. The Split-Step and Finite Difference calculation approaches were then considered. This chapter also introduces geometric optics.

The equipment used in this study was then described in detail along with discussion of the work undertaken to prepare it for deployment on the experimental link. The transmitter and the receive array were discussed separately in Chapters 4 and 5.

Chapter 4 introduced the transmitter and its design. The chapter continues with the introduction of the additional design elements brought to the transmitter during this study in order to equip it for deployment. Key amongst them, the 2.28 GHz frequency generator, communications and control board and the Rubidium frequency standard.

The description then focused on the choice of components for the control and communications and the successful integration of those selected components into a working system. Key to this is the software design which was

also presented in detail.

Finally the practical considerations pertaining to deployment were discussed.

Chapter 5 presented an overview of the receivers and Demodulation Unit (DU) which form the superhetrodyne receiver array. The mechanical rebuild and refurbishment of both the DU and receivers was presented in detail.

Detailed descriptions of the extensive design considerations relating to the protection of the MMICs in the power supply and regulation stages were presented.

The testing and deployment of the receive equipment was also presented in detail.

In Chapter 6, the terrestrial link established with the equipment was then described together with the APM propagation modelling technique used for theoretical analysis of the link.

This chapter presented a five parameter model and its use in creating refractivity profiles, subsequently processed by the Advanced Propagation Model (APM) in order to build up a propagation database. The results from this database were then analysed yielding an indication of anticipate results from the measurement data of Chapter 7.

Chapter 7 presented the results gathered during the data collection campaign and the resulting analysis using the various techniques previously described.

Finally this chapter presented the conclusions reached as a result of this study. The analysis of the data collected during the operation of the experimental link covered a wide range of meteorological events and conditions.

The analysis confirmed the severe attenuation resulting from rain events. The analysis concentrated on the refractive index and how the formation of ducts and inversions affected the Angle of Arrival (AOA). The conclusions to be drawn are that AOA variations do occur on microwave links as a result of meteorological activity induced refractivity changes. The small fluctuations caused by scintillation appear as noise on the underlying broad AOA and the experimental results demonstrate close agreement with the APM model

results in the majority of the cases examined. It can therefore be said that the use of the APM modelling technique is a valid method for predicting the AOA on such an experimental link.

As a result of the agreement between the experimental results and the APM model run database, the APM database can be considered to be a valuable dataset in its own right, describing the link under various refractivity conditions. This validation of the modelling approach would allow further study of the link without the physical experimental overhead.

A further implication of the close agreement seen between the experimental and model results is that the experimental method worked and the substantial dataset compiled from it is also a valuable dataset.

One observation to be made would be that it is possible that, with the experimental link not being horizontal but instead having a slight slant of 0.2°, the radio signal may not have coupled into ducts as readily as a horizontal link might. Unfortunately it is the nature of experiments in the real world that conditions cannot be ideal and in this case this was one sacrifice which had to be made in order to benefit from the substantial link length and also the link profile on offer.

The results, both from the APM and the experiment itself, clearly demonstrate that the AOA does not vary wildly nor does it have a particularly large range. The range when considered with the geometrical experimental offset of 0.2° is of the order of tenths of a degree. These sorts of angles would not, for example, cause a link to couple with another neighbouring one unless much greater path lengths were involved. For obvious reasons links of such lengths would be impractical within the bounds of operational microwave radio links. It can therefore be concluded that the fluctuations caused by variations in the refractive index as the result of meteorological events do not cause AOA changes of the magnitude necessary to account for the observations noted in [58]. Here, it was believed that the AOA fluctuations could, under certain conditions, be sufficiently large that cross coupling could occur on parallel microwave radio links.

The results seen in this study do not support that hypothesis. The larger AOA variations seen in the vertical would not account for this effect and

therefore the smaller horizontal variations observed would be insufficient too.

Although the receive array consisted of only four units rather than the intended five and therefore suffered reduced resolution in the horizontal direction, there were no significant differences between the horizontal and vertical measurement axis. It is clear that the vertical channels saw greater changes in the AOA then the horizontal. This is due to the greater variability of refractive index vertically.

The affects of snow were considered, though despite our varied climate in the UK, we only experienced very limited periods of snow during the data collection campaign. The analysis appears to support the prediction that snow does not cause AOA deflections but does cause some attenuation resulting from scattering.

The effects of attenuation appear to be very much more significant in terms of link reliability than scintillation induced AOA fluctuations. From the periods examined in detail and from the daily heart beat printouts, no periods of link loss were noted which did not have an attenuation event or hardware failure associated with them. It can therefore be stated that this experiment supports the link availability being accurately described from the link budget and rainfall statistics for the climate in which it is operating.

Clearly there is a difficulty in making unambiguous measurements of AOA at high frequencies due to the physically small wavelength. This has been further exacerbated in this study with the loss of one receiver head unit. The effect of this was reduced horizontal sensitivity. It would be highly desirable to extend both baselines with additional receiver units both in terms of more units and an overall longer baseline.

Consideration should also be made to not only the main lobe but also side lobes which from the point of view of interference with neighbouring links are more important than the main lobe.

One aspect which might be worthy of further consideration are the effects of scattering precipitation, not on the link thus affected but on links which become coupled in as a result. It has been shown that such scattering precipitation does not prevent the source link from operating however the energy

scattered might have an appreciable effect on, for example, an orthogonal link. It is possible that the effects seen in [58] can in fact be explained by such mechanisms rather than the predominant AOA examined in this study.

Appendix A

Mesoscale Model Version 5

The Mesoscale Model version 5 (MM5) was developed by Pennsylvania State University and the National Center for Atmospheric Research. It is a limited-area, non-hydrostatic, terrain-following sigma-coordinate model designed to simulate or predict mesoscale atmospheric circulation [59].

This translates to a model which considers the atmosphere to be a fluid system, to which it is possible to apply fluid mechanics and which considers vertical motion within the atmosphere. The model also uses a sigma coordinate system which simplifies the lower boundary conditions.

The model is the 5th generation of the model system comprised of a number of sub-programmes. This permits the model to be adapted to individual cases and suits the diverse user base. The system is harder to run as an system than a single unit implementation though un-supervised operation is still achievable.

The use of the model as a source of data for this study was entirely historic, that is it used historic data to recreate past events though the model can be operated as a real time forecasting tool.

The model is sufficiently adaptable to permit installation and operation on a single unix based machine, small clusters of PCs and similar architectures. The model in this instance is run on a cluster of six identical nodes at the University of Bath, each node is a 2.8 GHz Pentium IV with 512 MB of physical RAM.

The MM5 models the atmosphere as a fluid, applying fluid mechanics to

the task of atmospheric modelling. By moving away from a hydrostatic approximation (where the force at a given point caused by the pressure gradient is considered to be balanced by the weight of the air above that point) which is valid on a large scale, the model is able to resolve small scale convective events.

The MM5 model requires a set of initial conditions as a starting point for the modelling process as well as a set of lateral boundary conditions, since it is a regional model, to define the state around the boarders of the domain throughout the simulation.

The model uses orography and with a more subtle effect, land-use profiles. The lateral boundary conditions are then applied together with initial metrological data, defining the start point. This data usually comprises:

- Air temperature (K)
- u & v horizontal wind components (relative to domain grid) (ms^{-1})
- Relative humidity (%)
- Geo-potential height (m)
- Sea-level pressure (Pa)
- Sea-surface temperature (K)

The model may then be optionally refined with surface and radiosonde observational data before the MM5 module itself is invoked.

A significant proportion of the implementation involves the conversion of data from one format to another. This features heavily in the production of the data used in the analysis in this investigation. The output data from the model requires processing to achieve the output structure which is suitable for processing within MATLAB.

Bibliography

[1] J. H. Van Vleck.
Absorption of microwaves by oxygen & the absorption of microwaves by uncondensed water vapour.
Physics Review, 71:413–433, April 1947.

[2] Attenuation by atmospheric gases.
ITU-R, P.676-5, 2001.

[3] Water vapour: surface density and total columnar content.
ITU-R, P.836-3, 2001.

[4] D. C. Blanchard.
The behaviour of water drops at terminal velocity in air.
Transactions of the American Geophysical Union, 31:836–842, December 1950.

[5] H. R. Pruppacher and K. V. Beard.
A wind tunnel investigation of the internal circulation and shape of water drops falling at terminal velocity in air.
Quarterly Journal of the Royal Meteorological Society, 96:247–256, April 1970.

[6] C Magono.
On the shape of water drops falling in stagnant air.
Journal of Meteorology, 11:77–79, February 1954.

[7] H. R. Pruppacher and R. L. Pitter.
A semi-empirical determination of the shape of cloud and rain drops.
Journal of the Atmospheric Sciences, 28:86–94, January 1971.

[8] R. A. Semplak.
Effect of oblate raindrops on attenuation at 30.9 GHz.
Radio Science, 5:559–564, March 1970.

[9] M. J. Saunders.
Cross polarization at 18 and 30 GHz due to rain.
IEEE Transactions on Antennas Propagation, AP-19:273–277, March 1971.

[10] D. T. Thomas.
Cross-polarization distortion in microwave radio transmission due to rain.
Radio Science, 6:833–839, October 1971.

[11] S. Okamura, K. Funakawa, H. Uda, J. Kato, and T. Oguchi.
Effect of polarization on the attenuation by rain at millimeter-wave length.
Journal of the Radio Research Laboratories (Japan), 8:73–80, March 1961.

[12] J. Joss, J. C. Thams, and A. Waldvogel.
The variation of raindrop size distributions at Locarno.
Proceedings of the International Conference on Cloud Physics (Toronto, Ontario, Canada), pages 369–373, 1968.

[13] U. H. W. Lammers.
Electrostatic analysis of raindrop distributions.
Journal of Applied Meteorology, 8:330–334, June 1969.

[14] M Schönguber.
Joanneum research - 2d video distrometer.
www.distrometer.at, 2006.

[15] J. S. Marshall and W. McK. Palmer.
The distribution of raindrops with size.
Journal of Meteorology, 5:165–166, 1948.

[16] J. O. Laws and D. A. Parsons.
The relation of rain-drop size to intensity.

Transactions of the American Geophysics Union, 24:432–460, September 1943.

[17] C. W. Ulbrich.
Natural variations in the analytical form of the raindrop size distribution.
Journal of Climate and Applied Meteorology, 22:1764–1775, 1983.

[18] A. Vander Vorst.
Cross-polarization on a terrestrial path.
Alta Frequenza, 48:201–209, April 1979.

[19] R. L. Olsen.
Cross polarization during precipitation on terrestrial links.
Radio Science, 16:761–779, September 1981.

[20] Specific attenuation model for rain for use in prediction methods.
ITU-R, P.838-2, 2003.

[21] Characteristics of precipitation for propagation modelling.
ITU-R, P.837-4, 2003.

[22] Propagation data and prediction methods required for the design of terrestrial line-of-sight systems.
ITU-R, P.530-10, 2001.

[23] M.P.M. Hall et al.
Propagation of radiowaves.
Institution of Electrical Engineers, 1996.

[24] D. Atlas, M. Kerker, and W. Hitschfeld.
Scattering and attenuation by non-spherical atmospheric particles.
Journal of Atmospheric and Terrestrial Physics, 3:103–119, 1953.

[25] N. R. Labrum.
The scattering of radio waves by meteorological particles.
Journal of Applied Physics, 23:1324–1330, December 1952.

[26] C. Yeh, R. Woo, A. Ishimaru, and J. Armstrong.
Scattering by single ice needles and plates at 30 GHz.

Radio Science, 17:1503–1510, November-December 1982.

[27] C. Magono and T. Nakamura.
Aerodynamic studies of falling snowflakes.
Journal of the Meteorological Society of Japan, 43:139–147, June 1965.

[28] Y. Sasyo.
The collection efficiency of simulated snow particles for water droplets (ii)-on the oscillatory angular motion of the snowflake.
Meteorology and Geophysics (Tokyo), 28:159–168, December 1977.

[29] G.G. Kuznetsov, C. J. Walden, and A. R. Holt.
Attenuation of microwaves in sleet.
Final Report to the Radiocommunications Agency, August 2000.

[30] M. P. Langleben and K. L. S. Gunn.
Scattering and absorption of microwaves by a melting ice sphere.
Stormy Weather Research Group (Report), McGill University, Montreal, Canada, MW-5, 1952.

[31] B. M. Herman and L. J. Battan.
Calculations of Mie back-scattering from melting ice spheres.
Journal of Meteorology, 18:468–478, August 1961.

[32] T. Oguchi.
Scattering and absorption of a millimeter wave due to rain and melting hailstones.
Journal of the Radio Research Laboratories (Japan), 13:141–172, May 1966.

[33] P. Debye.
Polar molecules.
Dover, 1957.
pages 89-90.

[34] E. K. Smith and S. Weintraub.
The constants in the equation for atmospheric refractive index at radio frequencies.
Proceedings of the Institute of Radio Engineers, 41:1035–1037, 1953.

[35] The radio refractive index: its formula and refractivity data.
ITU-R, P.453-9, 2003.

[36] V. I. Tatarski.
Wave propagation in a turbulent medium.
McGraw-Hill, New York, 1961.

[37] R. B. Stull.
An introduction to boundary layer meteorology.
Kluwer Academic Press, 1988.

[38] Mark Evans.
Effects of Atmospheric Turbulence on Millimetre Wave Propagation in the Surface Boundary Layer.
PhD thesis, School of Physics and Astronomy, University of St Andrews, 2004.

[39] U Frisch.
Turbulence: The legacy of A. N. Kolmogorov.
Cambridge University Press, 2001.

[40] H Tennekes and J. L. Lumley.
A first course in turbulence.
MIT Press, 1972.

[41] J. L. Lumley and H. A. Panofsky.
The structure of atmospheric turbulence.
John Wiley & Sons, 1964.

[42] G. I. Taylor.
The spectrum of turbulence.
Proceedings of the Royal Society, A164:476, 1938.

[43] G. E. Willis and J. W. Deardorff.
On the use of Taylor's translation hypothesis for diffusion in the mixed layer.
Journal of the Royal Meteorological Society, 102:817–822, 1976.

[44] A. Richard Thompson, James M. Moran, and George W. Swenson Jr.
Interferometry and Synthesis in Radio Astronomy.

John Wiley and Sons, INC, 2001.

[45] Elie J. Baghdady.
Hybrid interferometry for high-resolution DOA measurement.
IEEE, pages 2092–2097, 1989.

[46] H. W. Ko, J. W. Sari, and J. P. Skura.
Anomalous wave propagation through atmospheric ducts.
John Hopkins APL Technical Digest, 4:12–26, 1983.

[47] K. H. Craig.
Propagation modelling in the troposphere: parabolic equation method.
Electronic Letters, 24:1136–1139, 1988.

[48] K. H. Craig and M. F. Levy.
Parabolic equation modelling of the effects of multipath and ducting on radar systems.
IEE Proceedings, Part F, 138:153–162, 1991.

[49] G. D. Dockery.
Modelling electromagnetic wave propagation in the troposphere using the parabolic equation.
IEEE Transactions on Antennas and Propagation, 36:1464–1470, 1988.

[50] G. D. Dockery and J. R. Kuttler.
An improved impedance boundary algorithm for fourier split-step solutions of the parabolic wave equation.
IEEE Transactions on Antennas and Propagation, 44:1592–1599, 1996.

[51] G. D. Dockery and J. R. Kuttler.
Theoretical description of the PE / Fourier split-step method of representing electromagnetic propagation in the troposphere.
Radio Science, 26:381–393, 1991.

[52] Mireille Levy.
Parabolic equation methods for electromagnetic wave propagation.
IEE Electromagnetic Wave Series 45. The Institute of Electrical Engineers, 2000.

[53] Stanford Research Systems, Sunnyvale, California.

Model PRS10 Rubidium Frequency Standard, Operation and Service Manual, December 2001.

[54] H. A. Wheeler.
Transmission-line properties of a strip on a dielectric sheet on a plane.
IEEE Transactions on Microwave Theory and Techniques, MTT-25:631–647, August 1977.

[55] Tom Roberts.
Circuit improvements on bias for GaAs FETs.
EDN Europe, page 54, December 2001.

[56] US Military.
APM User Guide.

[57] Peter Gerstoft, L. Ted Rogers, Jeffrey L. Krolik, and William S. Hodgkiss.
Inversion for refractivity parameters from radar sea clutter.
Radio Science, 38(3):MAR 18 1–22, April 2003.

[58] I. Flood.
Private communication.
2001.

[59] MM5 community model website.
www.mmm.ucar.edu/mm5/, 2005.